Light-induced Energy Production Using Plasmonic Photocatalysis

by

Ehsan Vahidzadeh

A thesis submitted in partial fulfillment of the requirements for the degree of

Doctor of Philosophy

in

Microsystems and Nanodevices

Department of Electrical and Computer Engineering
University of Alberta

Abstract:

Diversifying the energy sources and finding an alternative for fossil fuels is the new global challenge. To this end, utilizing solar light to produce energy carriers such as hydrogen and hydrocarbons attracted tremendous attention. Hydrogen and methane can be produced through photo-induced processes named water-splitting and CO_2 photoreduction, respectively. Water-splitting is the process where water molecules are broken into hydrogen and oxygen. The hydrogen produced in this process can be utilized for applications such as fuel cells or hydrogen-powered vehicles. The CO_2 photoreduction process converts CO_2 (which is considered waste and the major contributor to global warming) into valuable products. As a result, this process is regarded as the missing puzzle piece to address the global warming issue. The practical application of these two processes is contingent upon the fabrication of highly efficient photocatalysts. Photocatalysts are a family of heterogeneous catalysts that can increase the rate of chemical reactions by producing photogenerated electron-hole pairs. Since the interaction with light is a primary step in a photocatalytic reaction, engineering the light absorption properties, increasing the electron-hole pair generation, and suppressing their recombination is key to improving their efficiency. The most novel direction in photocatalysis research is plasmonic photocatalysis. Plasmonic materials are usually metal nanoparticles such as Au and Ag. Plasmonic metal nanoparticles can interact extensively with incident light, making them an interesting nominee for photocatalytic applications. The advantages of using plasmonic materials for applications such as CO_2 photoreduction and water-splitting motivated me to investigate their ability to drive these chemical reactions.

In the first step of my Ph.D. studies, a heterojunction between bimetallic plasmonic (AgCu) nanoparticles with semiconductor (TiO_2 nanotube arrays) was fabricated through a facile photo deposition technique. These samples were characterized with state-of-the-art characterization techniques and utilized for CO_2 photoreduction reaction.

In the second step, core-shell Au@a-TiO_2 photoelectrodes were fabricated and utilized for photoelectrochemical water-splitting reaction. The mechanism of the charge transfer between the Au and a-TiO_2 was investigated using several experiments such as surface potential measurement using Kelvin probe force microscopy and conducting the water-splitting reaction in the presence of a hole scavenger. The Au@a-TiO_2 photoelectrode fabricated in this step exhibited remarkable photocurrent responses with high faradaic efficiency.

In the third step, sponge-shaped Au nanoparticles (Au-Sponge) were fabricated using a creative dewetting followed by dealloying technique. Au-Sponge samples were utilized for CO_2 photoreduction reaction. In comparison with regular spherical-shaped Au nanoparticles (Au-Island) the Au-Sponge sample exhibited outstanding photocatalytic performance.

Preface:

All results presented in this thesis were obtained during my Ph.D. studies in electrical and computer engineering at the University of Alberta, under supervision of Professor Karthik Shankar.

The thesis starts with an introductory chapter that asserts the importance of the development of light-harvesting technologies and plasmonic materials. Chapter 2 of this dissertation is about the methodology and the experimental setup including chemicals and materials used for the synthesis and running the experiments, experimental procedure for the CO_2 photoreduction, water-splitting and hydrogen evolution. Chapter 3 has been published as an article titled, "Asymmetric Multipole Plasmon-Mediated Catalysis Shifts the Product Selectivity of CO_2 Photoreduction toward C_{2+} Products" in the journal of Applied Materials and Interfaces. I have designed and performed the measurements and wrote the manuscript for this study, and Sheng Zeng helped me with CO_2 photoreduction reaction experiments. Ajay Manuel helped me with the finite difference time-domain (FDTD) simulations. Saralyn Riddell, Dr. Pawan Kumar, and Dr. Kazi Alam helped me with the sample characterizations and data collection. Results presented in chapter 4 are related to a full-fledged article titled "Au-amorphous TiO_2 heterojunction: Plasmon coupled ultrathin hot carrier photoanode and photocathode for high-performance photoelectrochemical water-splitting." This article is going to be submitted to a journal soon. In this study, I have synthesized the samples and conducted the experiments. Sheng Zeng, Dr. Kazi Alam, Dr. Pawan Kumar, and Saralyn Riddell helped me with sample characterization and data collection.

The results of chapter 5 are related to a written article titled "Sponge shaped Au nanoparticles: A practical stand-alone photocatalyst for driving light-induced CO_2 reduction reaction via interband transition" in the study, I have devised the experiments, fabricated, and characterized the samples and Saralyn Riddell helped me with sample fabrication. This article is ready to be submitted as a communication to a journal. Finally, the last chapter of this dissertation is dedicated to the conclusions and the future works.

Acknowledgment:

Firstly, I would like to thank Professor Karthik Shankar for his guidance, patience, support, and encouragement. I was a student with a chemical engineering background who he openly accepted in his research group as a graduate student. I was lucky to join his group and learn about the domains I was unfamiliar with. Looking back at these four years of an unforgettable journey, I have learned not to be afraid of exploring new things, it helped me better myself. It was not possible without Dr. Shankar's help.

Special thanks to my supervisory committee, Dr. Behrad Gholipour and Dr. Jingli Luo, for their insightful suggestions and their help to improve my research quality.

I am incredibly grateful to my colleagues, Arezoo Hosseini and Najia Mahdi, who helped me whenever I needed them. As an international student who did not have many friends here, they treated me like a family member. I am also grateful to my lab mates Sheng Zeng, Aarat Kalra, Yun Zhang, Ujwal Kumar Thakur, Ajay Peter Manuel, Ryan Kisslinger, Saralyn Riddell, Dr. Pawan Kumar, and Dr. Kazi Alam. I learned from all of them, and they impacted my research in so many ways.

I was lucky to be part of the ATUMS community. I want to express my appreciation to Jonathan Veinot and Leah Veinot, who founded the ATUMS program. Kudos to their excellent work to increase the international collaboration of the University of Alberta with the technical university of Munich. I want to extend my sincere thanks to Prof. Dr. Ulrich Heiz, Dr. Aras Kartouzian, and Natalie Fehn from the technical university of Munich. I spent three months of research in their lab and appreciated all the help and support I received during my research visit.

Finally, I would like to express my gratitude to my family. My mom sacrificed everything for me to take stride in the way of success. She always encouraged me to pursue my studies and gave me

confidence and love throughout this journey. My dad who stood behind me whenever I needed his help. He always believed in me and gave me confidence in doing the things I was afraid of doing. My sister who helped me whenever I needed help and my brother who played the role of a guru for me.

Table of Contents

List of Tables

List of Figures

List of Symbols

ΔG^0	Change in Gibbs free energy of reaction under standard condition
ΔE	Applied potential for water electrolysis
λ	Wavelength
θ	The angle between incident beam and the crystallographic reflecting plane
$M_{product}$	Mole fraction of the product
P_{total}	Total pressure of the reactor
$P_{product}$	Partial pressure of the product
w	Estimated weight of the sample
μ	Permeability
ε	Permittivity
E	Electric Field
H	Magnetic Field
n	Refractive index
A°	Angstrom
AgCu	Bimetallic silver and copper
ϕ	Work Function
$E_{cut\text{-}off}$	Cut-off energy of secondary electrons
h	Plank’s constant
ν	Frequency
m/z	Mass to charge ratio

List of Abbriviations and Acronyms

Ag(acac)	Silver Acetylacetonate
ALD	Atomic Layer Deposition
AM 1.5	Air mass 1.5
AM0	Air mass 0
BE	Binding Energy
CO_2RR	CO_2 Reduction Reaction
Cu(acac)2	Copper Acetylacetonate
CV	Cyclic Voltammetry
DC	Direct Current
DFT	Density Functional Theory
DRS	Diffuse-reflectance Spectra
ECSA	Electrochemical Surface Area
EDS	Energy-dispersive X-ray Spectroscopy
EG	Ethylene Glycol
FCC	Face-Centered Cubic
FDTD	Finite difference Time domain
FESEM	Field Emission Scanning Electron Microscope
FTO	Fluorine-doped Tin Oxide
GC	Gas Chromatograph
GC-MS	Gas Chromatography–mass Spectrometry
GHG	Greenhouse Gases
GUI	Graphical User Interface
HPLC	High Performance Liquid Chromatography
HR-TEM	High-resolution Transmission Electron Microscope
I.R.	Infrared
KPFM	Kelvin Probe Force Microscopy
LED	Light-emitting Diode
LSPR	Localized Surface Plasmon Resonance
LSV	Linear Sweep Voltammetry
MS	Mott-Schottky
NHE	Normal Hydrogen Electrode
NIR	Near-infrared
PDD	Pulsed Discharge Detector
PEC	Photoelectrochemical
PIRET	Plasmon-induced Energy Transfer
PML	Perfectly Matched Layer
PPM	Parts Per Million
PRET	Plasmon Resonance Energy Transfer

RF	Roughness Factor
SAED	Selected Area Electron Diffraction
SSA	Specific Surface Area
TFSF	Total-field Scatter-field
TNTA	TiO_2 Nanotube Array
U.V.	Ultraviolet
UNFCCC	United Nations Framework Convention on Climate Change
UPS	Ultraviolet Photoelectron Spectroscopy
VB	Valence Band
VBmax	Valence band maxima
WF	Work Function
XPS	X-ray photoelectron Spectroscopy
XRD	X-ray Diffraction

1. Introduction

1.1. Renewable Energies

As heavy reliance on expendable fossil fuels brought challenges such as global warming, pollution, and climate change, seeking a sustainable energy resource is in great demand globally. Energy resources such as wind energy, hydro energy, solar energy, and geothermal energy are among the most sustainable energy resources which have been utilized to mitigate the negative effects of the chronic usage of fossil fuels. While fossil fuels are considered the primary culprit for the emission of greenhouse gasses (GHG) such as CO_2, renewable energy resources can fulfill the global energy demands with almost zero GHG emission.[1]

In December 2015, parties of the United Nations Framework Convention on Climate Change (UNFCCC) reached an important agreement to fight against climate change and invest in a sustainable/low carbon future. This agreement is now known as the Paris agreement. This agreement's primary goal is to invest in reliable technologies to decrease the global temperature rise below 2 degrees Celsius. Fossil fuels continue to play a significant role in the world's electricity production with a share of 73.5% in 2017.[1] The silver lining is that after the Paris agreement, there is a global tendency to increase the share of renewable resources in global energy production. To reach the Paris agreement's goals, investing in solar energy, which is available worldwide, is of great importance.

As a ubiquitously available clean energy source, solar energy holds the promise to meet the energy demands throughout the world. Figure 1 exhibits the solar light spectrum and the amount of energy emitted by the sun, which is around 1376 W/m^2 (Air mass 0, AM0). A portion of this energy is being absorbed by the Earth's atmosphere. The energy that can reach the Earth's surface is around 1000 $W/\ m^{2,}$ known as Air mass 1.5 (AM 1.5). This amount of energy that continuously reaches the Earth's surface is more than enough to meet our energy demands. According to the solar light spectrum, only 5% of the light reaching the Earth's surface belongs to the ultraviolet (U.V.) region. Around 43% belongs to the visible region, and the rest belongs to the infrared (I.R.) region. This fact justifies the tremendous efforts scientists take to fabricate visible light-sensitive devices.

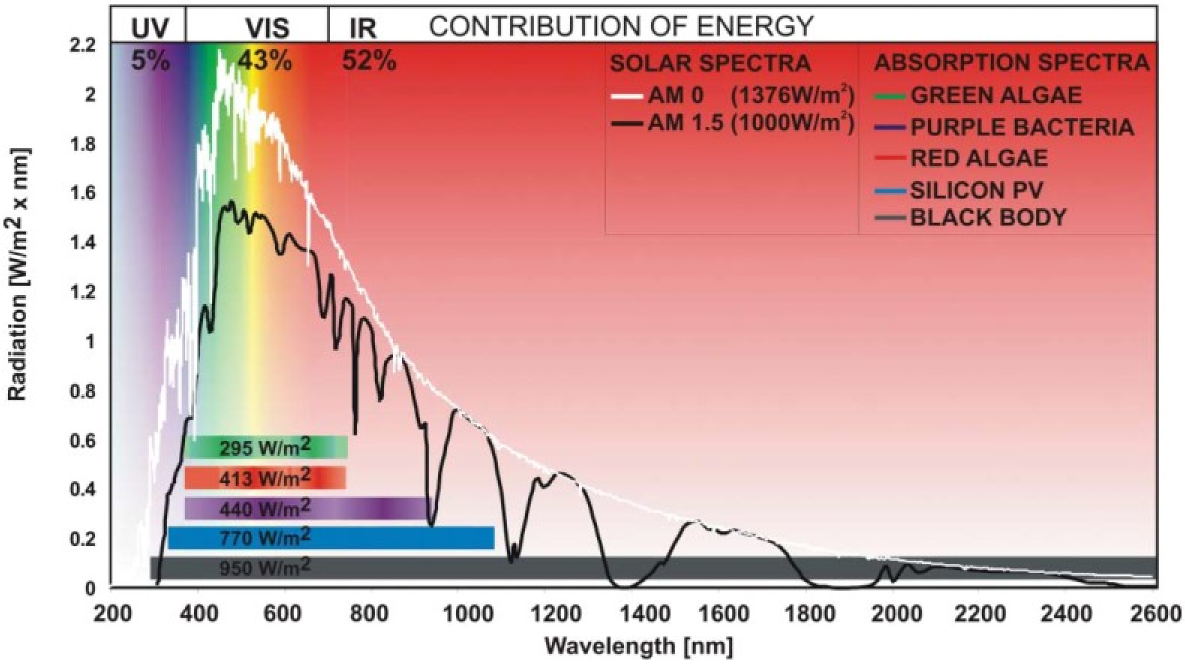

Figure 1. The solar energy spectrum and the amount of energy emitted by the sun (AM0), and the amount of energy received at Earth's surface (AM.1.5), the color bars exhibit the absorption of green plants, purple bacteria, red algae, and silicon-based photovoltaics. Reprinted with permission from Kruse et al. Copyright 2005 Royal Society of Chemistry.[2]

Solar energy can be stored as a clean energy source in different ways. The most conventional way is to store the sunlight energy as electricity using photovoltaic devices. From the advent of the first solar cell devices in early 1839 till today, this became an extensive area of research that led to the industrial-scale fabrication of commercial silicon-based solar cells, which are being used today.[3] The conversion of solar energy to electricity using photovoltaics has its shortcoming as well. One of the main drawbacks of using this technology on a large scale is that the excess electricity generated using solar light should be stored. It requires the photovoltaic devices to be hybridized by battery storage systems to make them operational. The expensive battery technologies make the capital investment of photovoltaic power plants very high. As a result, scientists worldwide decided not to limit their choice to store solar energy only into electricity.

Compared to electricity, hydrogen and methane offer a better gravimetric energy density, ease of storage, and ease of transportation.[4] The next step in solar energy utilization is to store it in the form of a fuel such as hydrogen or methane. The photons of sunlight have energies ranging from 1-3 eV (100-300 kJ/mol), which is high enough to drive different chemical reactions.[4] Hydrogen can be produced by splitting of water (a process which is being called water-splitting), in a process in which oxygen is being produced as a byproduct, also using water or hydrogen as other reactant CO_2 can be converted into methane, ethane, and Carbon monoxide utilizing solar energy. This reaction is being called CO_2 photoreduction reaction.

1.2. Photoelectrochemical water-splitting and CO_2 photoreduction

The amount of energy needed for reversible water-splitting reaction is 237 kJ.mol^{-1}, within the range of the energy provided by solar light. This reaction can be written as follows:

$$2H_2O + Sunlight \rightarrow 2H_2 + \ 2O_2 \ \ \Delta G_0 = 237\ kJ/mol \qquad (1.)$$

Photoelectrochemical (PEC) water-splitting is a process that can utilize solar light to drive the reaction mentioned above using a photocatalyst. For photoreduction of CO_2 with water, the situation is different, as CO_2 is a stable molecule, the amount of energy needed to dissociate the C=O is very high. As a result, the energy required to convert CO_2 to methane (the main product of CO_2 photoreduction) is as high as 818.3 kJ.mol^{-1}.[5] The higher activation energy needed for driving the CO_2 reduction reaction makes it a more difficult reaction to conduct than water-splitting reaction. The overall CO_2 photoreduction reaction can be written as follows:

$$CO_2 + 2H_2O + Sunlight \rightarrow \ CH_4 + \ 2O_2 \ \ \Delta G^0_{298\,K} = 818\ kJ/mol \qquad (2.)$$

To understand how photocatalytic processes work, first, we should understand the concept of catalysis. In general, a catalyst is a substance that facilitates a chemical reaction without itself being consumed throughout the process. Estimations show that almost 90% of the industrial chemical processes are catalytic.[6]

Figure 2a exhibits the operating principle of a photocatalyst. Inspired by photosynthesis, a photocatalyst is a hybrid of heterogeneous catalysts and semiconductors that can accelerate a specific chemical reaction utilizing sunlight. When irradiated by sunlight, photocatalysts generate excited electron-hole pairs. These excited electron-hole pairs react with the reactants in the photocatalyst's vicinity and drive the chemical reaction. In photocatalysis, the photogenerated electron-hole pairs are the main driving force for the chemical reaction. Since photocatalysts can produce the reactive electron-hole pairs by themselves, photocatalytic processes can usually be implemented in milder conditions (lower temperature and pressure) than conventional catalytic counterparts that use heat as the driving force of the chemical reaction.[7] Figure 2b exhibits the energy diagram for both CO_2 photoreduction and water-splitting reactions. Both reactions can be categorized as thermodynamically unfavorable reactions as Gibbs free energy changes are positive ($\Delta G > 0$). As being shown by Figure 2, the electron-hole pairs are being provided by the photocatalyst to the reactants to drive the reaction in both of these reactions.[8]

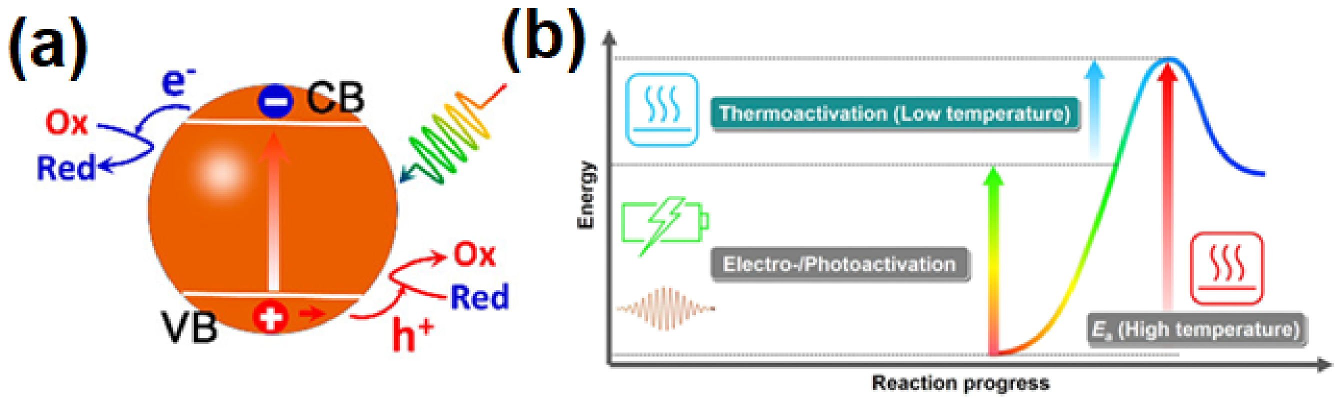

Figure 2. Schematic illustration of the working principle of a photocatalyst under excitation(a). Reprinted with permission from Yang et al. Copyright 2018 American Chemical Society. [9] Schematic illustration of the energy diagram for photocatalytic water-splitting and CO_2 reduction reactions (b). Reprinted with permission from Meng et al. Copyright 2019 Royal Society of Chemistry.[8]

Depending on the type of the reaction, the energy related to activation of the reactants in a photo/catalytic process can be provided by electro activation (electrolysis), electro /photoactivation (photoelectrochemical, PEC), photoactivation (photocatalysis), or only heat (temperature) in the purely catalytic processes. In PEC water-splitting, a photoelectrochemical cell (Figure 3) is used to conduct the experiment. A photoelectrochemical cell consists of a semiconducting photoelectrode (working photoelectrode), a metal counter electrode, and a reference electrode dipped inside an electrolyte. The working electrode that is a semiconductor is being irradiated with solar light, which produces the photogenerated electro-hole pairs then the electrons are extracted from the semiconductor to the counter electrode by the applied external electric field where the reduction reaction occurs, leaving holes in the semiconductor where oxidation reaction happens at the semiconductor/electrolyte interface. For CO_2 photoreduction reaction, an electrochemical cell is not necessary. Instead, a reactor that can hold high-pressure CO_2 gas is being used.

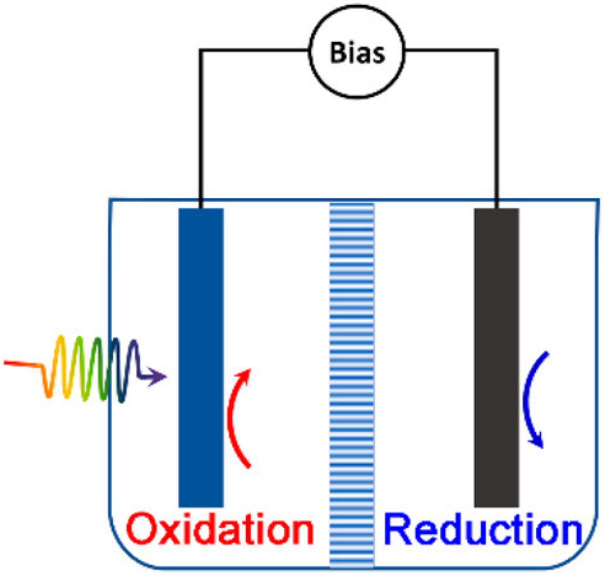

Figure 3. Schematic illustration of a photoelectrochemical cell. Reprinted with permission from Yang et al. Copyright 2018 American Chemical Society.[9]

For PEC water-splitting, the change in the Gibbs free energy (ΔG) can be related to the applied potential in PEC using the following equation:

$$\Delta G = -nF\Delta E \qquad (3.)$$

Where n is the number of electrons involved in the reaction, F is the Faraday constant (96485.3 C/mol), and ΔE is the applied potential. Since for the water-splitting $\Delta G^0_{298\ K}$ =237 kJ./mol and n=2, the ΔE calculated to be -1.23 V, this is the minimum potential applied in PEC to electrolysis the water.[4] The overall reaction written as equation 1 can be divided into the separate reactions happening in working and the counter electrodes. In an alkaline solution, these half-reactions and corresponding energy needed to drive them compared to a normal hydrogen electrode (NHE) can be written as:

$$4H_2O + 4e^- \rightleftarrows 2H_2 + 4OH^- \;\; E_{red} = -0.828\; vs.NHE \qquad (4.)$$

$$4OH^- + 4h^+ \rightleftarrows 2H_2O + O_2 \;\; E_{ox} = -0.401\; vs.NHE \qquad (5.)$$

In an acidic solution, these half-reactions and corresponding energy needed to drive them compared to NHE can be written as:

$$4H^+ + 4e^- \rightleftarrows 2H_2 \quad E_{red} = +0.00\,V\,vs.NHE \tag{6.}$$

$$2H_2O + 4h^+ \rightleftarrows 4H^+ + O_2 \quad E_{ox} = -1.229\,V\,vs.NHE \tag{7.}$$

Based on these energy calculations for water-splitting, a semiconductor's bandgap should be at least 1.23 eV to meet the water-splitting reaction's energy requirement. In addition to that requirement, for both water-splitting and CO_2 photoreduction reactions, the semiconductor's valence band and conduction band edges should be appropriately positioned to drive the oxidation and reduction half-reactions. In other words, the excited electron in the conduction band of the semiconductor should have enough energy to drive the reduction half-reaction, and the holes located in the valance band should also be oxidative enough to drive the oxidation half-reaction.

In PEC water-splitting, the oxidation half-reaction is more complicated (involve 4 electrons) than the reduction reaction (involves 2 electrons), which makes the oxidation half-reaction the main bottleneck of the PEC water-splitting reaction. Hence, a suitable semiconductor for a PEC water-splitting reaction should have a deep valence band edge (potent oxidative power).

For CO_2 photoreduction reaction, the situation is different. Usually, the first step of the CO_2 photoreduction is the production of $\cdot CO_{2*}^-$ intermediate through the following reaction:

$$CO_2 + e^- \rightarrow \cdot CO_{2*}^- \quad E_{red} = -1.90\,V\,vs.NHE \tag{8.}$$

This reaction is considered to be the rate-limiting step in CO_2 photoreduction reaction as there is a considerable energy difference (-1.90 V) between the linear CO_2 molecule and bent $\cdot CO_{2*}^-$ radical.[5] As a result, a suitable semiconductor for CO_2 photoreduction reaction should possess a conduction band edge high enough to drive the reduction reaction.

Figure 4 exhibits the valence band edge and conduction band edges of the most common semiconductors used in the literature compared to the energy required to drive the oxidation/reduction half-reactions in water-splitting and CO_2 photoreduction reactions.[5]

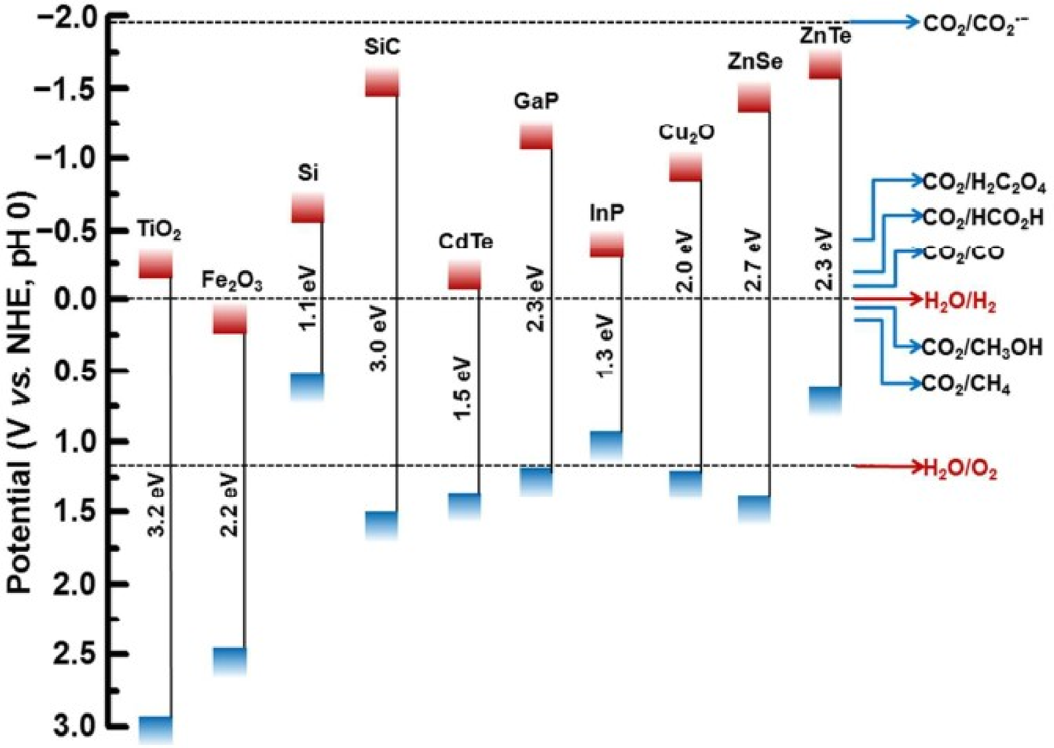

Figure 4. The position of valence band and conduction band of the common semiconductors vs. NHE. Reprinted with permission from Chang et al. Copyright 2016 Royal Society of Chemistry.[5]

Based on all of these complications for these two reactions, a suitable semiconductor for an efficient photoelectrode in a PEC water-splitting process should possess the following features[10]:

- Strong (visible light) absorption
- Suitable chemical stability
- Suitable band edge positions
- Efficient charge transport
- Low cost

Most of the commonly used semiconductors have wide band gaps, making them weak absorbers to the visible light. Among all these semiconductors, TiO_2 meets most of the prerequisites mentioned above except the strong visible light absorption and appropriate conduction band position for driving reduction half-reaction for CO_2 photoreduction, which makes it one of the most suitable semiconductors to be used as a photoelectrode in PEC water-splitting and CO_2 photoreduction processes.

1.3. Strategies to improve the performance of the photocatalysts.

TiO_2 is one of the most promising semiconductors for PEC water-splitting and CO_2 photoreduction applications. In addition to its poor light absorption properties limiting its photocatalytic efficiency, the photogenerated electron-holes pairs generated by the excited semiconductor tend to recombine fast. The recombination process adversely affects a semiconductor's ability to drive the chemical reaction because the recombination process limits the number of electron-hole pairs available for chemical reaction. One of the most effective ways to address this issue is making a heterojunction between the semiconductor and another material (usually another semiconductor or metal) to suppress the recombination process. The heterojunction materials are known to inherit the properties of each element or even exhibit new unique properties that make them suitable for many light-harvesting applications.[11, 12] In general, there are three different types of heterojunction depending on the band alignment of the two semiconductors, type-I heterojunction in which the band edges of one semiconductor are located between the band edges of the other one, type-II semiconductor in which the band edges of one semiconductor are higher than the other semiconductor and type-III in which both band edges of one semiconductor are even higher than the conduction band of the other semiconductor. There is no space charge region formed at the interface of the two semiconductors. In addition to these conventional types of heterojunctions between different kinds of semiconductors, a semiconductor and a metal can also form a heterojunction. Since the work function (the energy needed to extract an electron to a point in vacuum) of the metals are usually at different energy level compared to the semiconductors, when a heterojunction between the metal and the semiconductor forms, a depletion region with an internal electric field forms to reach neutrality also for metal and the semiconductor to reach equilibrium. This depletion region formation causes the genesis of a potential barrier and band bending at the metal/semiconductor interface. If the semiconductor is n-type, the band bending is upward (Figure 5d), and if the semiconductor is p-type, the band bending is downward (Figure 5e).[12-14] Conventionally, metals were considered a co-catalyst in photochemical reactions that could facilitate the reaction either by providing an appropriate adsorption site for the reactants or by providing a media for increasing the lifetime of the photogenerated electron-hole pairs via suppressing the recombination process. Recently, a new family of metals called plasmonic metals attracted attention for light-harvesting applications. The unique interaction of these metals with light, especially in the visible light spectrum, made their role go beyond only an electron (hole) acceptor of a simple co-catalyst.

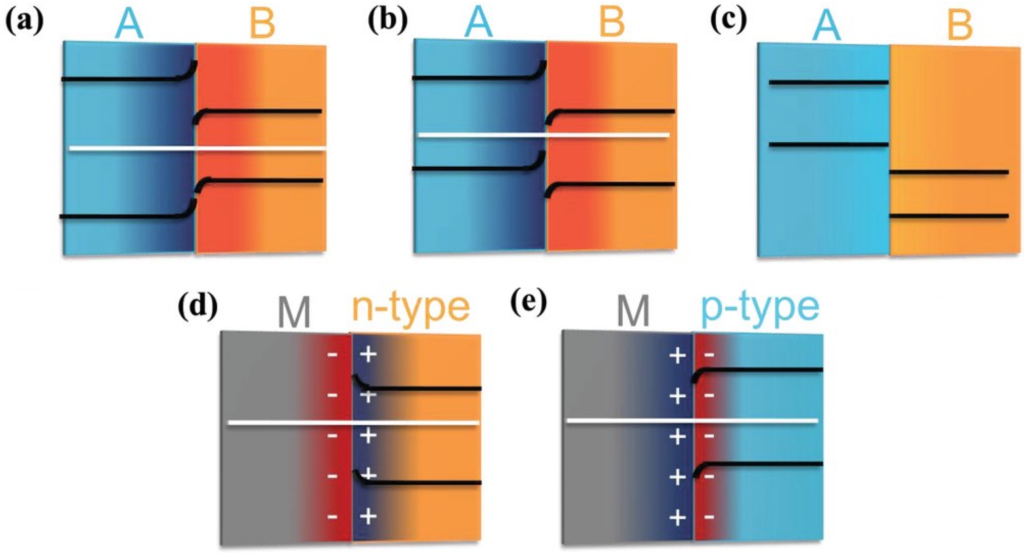

Figure 5. Schematic illustration of type-I (a), type-II (b), and type-III (c) heterojunctions and the heterojunction between an n-type semiconductor and metal (d) and a p-type semiconductor and metal (e). Reprinted from Su et al. under Creative Commons Attribution Copyright 2019 Wiley.[12]

1.3.1. Plasmonic metals and their heterojunctions with semiconductors

In a plasmonic metal/semiconductor heterojunction, not only the plasmonic metal acts as a simple co-catalyst but also affects the optical properties of the heterojunction. Plasmonic metal such as Ag, Au, and Cu can interact with incident electromagnetic waves through a phenomenon called localized surface plasmon resonance (LSPR). LSPR is the collective oscillation of the free electrons in the metals (Figure 6a). When the plasmonic nanoparticles' size is smaller than the incident wavelength, they can strongly interact with the incident light in specific frequencies known as plasmon frequency. Light with a frequency below the plasma frequency gets reflected, and light with a frequency above the plasma frequency gets transmitted by the metal nanoparticle.[15]

This strong interaction with light made plasmonic metal nanoparticles an exciting research area with applications ranging from surface-enhanced Raman spectroscopy, refractive index sensing, photovoltaics, photocatalysis, etc. When a metal is being excited by its LSPR, there are several mechanisms by which LSPR energy can decay. In general, these mechanisms can be divided into radiative and nonradiative groups. Figure 6b-d exhibits the primary means by which excited plasmon can decay, including radiative light scattering/trapping, nonradiative plasmon-induced energy transfer (PIRET), and nonradiative hot carrier injection. Usually, light scattering/trapping happens for large metal nanoparticles. The incident light gets scattered by the large metal nanoparticles, the plasmon's far-field scattering can penetrate the semiconductor, which enhances the photon flux in the semiconductor (Figure 6b).[16]

The plasmon can decay non-radiatively through Landau damping in hot carrier generation, including interband and intraband transition of electron-hole pairs in the plasmonic metal. These energetic hot carriers (they are called hot because usually, their energy is higher than their thermally excited counterparts) can get injected into the semiconductor's conduction or valence band. The injected electron to the semiconductor does not necessarily have an energy equal to the semiconductor's conduction. In fact, these injected charge carriers exhibit energy distribution up to the plasma frequency, so the injected carriers can still be considered hot.[16]

In PIRET, the plasmon's energy can transfer to the adjacent semiconductor through dipole-dipole interaction. Since the collective oscillation of electrons can make a significant dipole moment that generates a concentrated strong near field, this near field can non-radiatively create electron-hole pairs inside the semiconductor. Usually, when the semiconductor has a large bandgap (> 3.1 eV), the dominant decay process is the hot carrier generation.[16] Based on the previous section for PEC water-splitting applications, the band edge position limitations imposed by photocatalytic water-splitting reaction encourage us to use wide bandgap semiconductors such as TiO_2. That's why in most of the PEC water-splitting applications, the dominant mechanism is the hot-carrier injection.

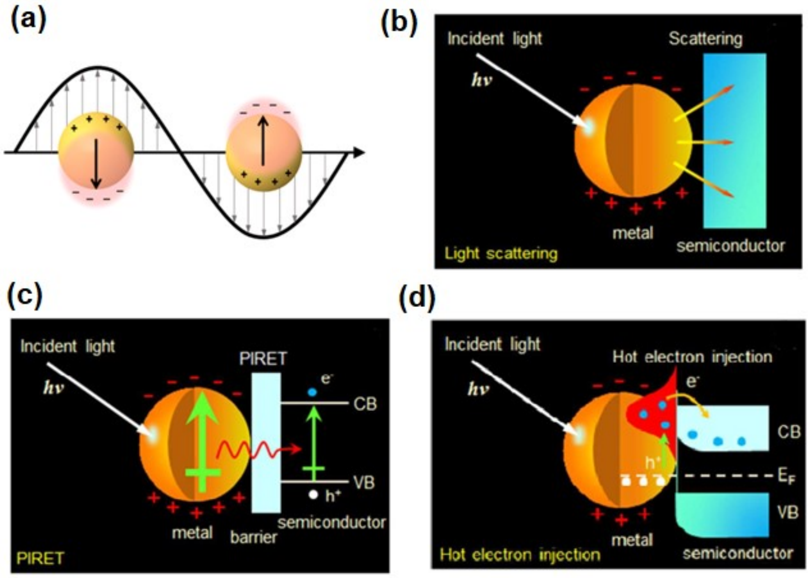

Figure 6. LSPR excitation of a spherical metal nanoparticle. (a) The resonant electromagnetic field induces oscillation of the electron gas. Reprinted with permission from Zhang et al. Copyright 2017 American chemical society.[17] Different mechanisms of LSPR decay, including light scattering (b), PIRET (c), and hot carrier injection (d). Reprinted with permission from Wu et al. Copyright 2018 Royal Society of Chemistry.[16]

Compared to conventional semiconductor photocatalysts, a plasmonic metal/semiconductor heterojunction possess two distinct feature which makes it useful for light-harvesting applications. The first one is Schottky's formation at the interface, which results in a built-in electric field in the contact area of the metal and the semiconductor. This electric field forces the electron-hole pairs to go in a different direction and facilitates the separation process.[18] The other important feature of such a heterojunction is that LSPR, the resonance wavelength of the plasmonic metal nanoparticles, can be tuned and fall within the visible range. As mentioned above, a heterojunction between a semiconductor can inherit both individual entities' optical properties. A plasmonic metal/semiconductor heterojunction can bring the visible light interaction to the table for solely U.V. responsive semiconductors such as TiO_2. The strong interaction of plasmonic metals with resonant light generates an intensive electric field that favors a photocatalytic reaction in several ways, such as excitation of excessive electrons and holes, heating the environment, and polarizing the absorbates for better absorption on the surface.[18]

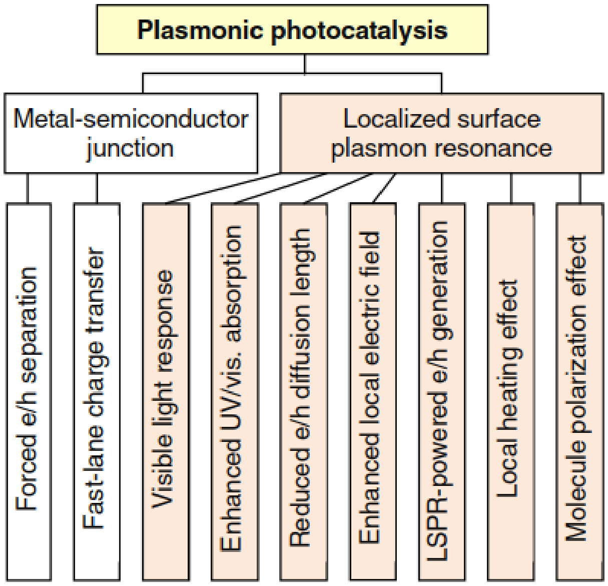

Figure 7. The major benefits of a metal/semiconductor heterojunction + the added benefits a plasmonic metal can offer for photocatalytic applications. Reprinted with permission from Zhang et al. Copyright 2013 IOP Science.[18]

Figure 7 briefly lists the significant benefits of a plasmonic metal\semiconductor heterojunction for photocatalytic applications. It is worthy of mentioning that regardless of if the metal in a heterojunction with a semiconductor is plasmonic or not, the metal itself can play several major beneficial roles such as surface catalysis, passivation of surface, etc., so the photocatalytic enhancement resulted due to the presence of a plasmonic metal in the heterojunction is a collective beneficiary effect of multiple features of the metal which plasmonic properties are only a portion of it.

Multiple advantages offered by the plasmonic metal nanoparticles for driving photocatalytic reactions made me investigate the effect of this interesting family of metals for driving complex light-induced chemical reactions such as water-splitting and CO_2 photoreduction. More specifically, since the charge transfer mechanism in a plasmon-coupled structure can be complicated, I decided to devise clever experimental procedures to shed light on it, which will be discussed in detail in the following chapters.

2. Materials and Methods

This chapter contains the details of the chemicals/devices used to conduct the experiments. Also, apparatuses and software used for simulation, fabrication, and characterization of the photocatalysts, analyzing the results, calibration of the devices, and conducting the photocatalytic reactions were explained thoroughly in this chapter.

2.1. Materials

Titanium foils (99%, 0.89mm thickness) were purchased from Alfa Aesar. Ammonium fluoride, ethylene glycol (EG, CAS 107-21-1), and methanol (CAS 67-56-1) were purchased from Fisher Scientific. Silver acetylacetonate (Ag(acac), CAS 15525-64-1) was supplied by Sigma Aldrich, and copper acetylacetonate ($Cu(acac)_2$, CAS 13395-16-9) was purchased from Acros. Potassium hydroxide (CAS 1310-58-3) with the purity of 85 % and Sodium sulfate (CAS 7757-82-6) with the purity of 99%were purchased from Sigma-Aldrich. Nitric acid (CAS 7697-37-2) with 70 % purity was purchased from Fischer Scientific. The solvents used for sample rinsing and material synthesis were deionized water and HPLC grade methanol purchased from Fisher Scientific. The CO_2 gas used for photocatalytic studies had 99% purity. It was obtained from Praxair, while the $^{13}CO_2$ isotope gas used for sanity tests had 99% purity and was obtained from Cambridge Isotope Laboratories, Inc. (USA).

2.2. Characterization

The morphologies of the samples were investigated using a field emission scanning electron microscope (FESEM, Zeiss Sigma) operating at an accelerating voltage of 5 kV. The morphological and structural properties of the samples were investigated using a high-resolution transmission electron microscope (HR-TEM, JEOL-2200 FS TEM) operating at an acceleration voltage of 200 kV. A Helium Ion Microscope (Zeiss Orion) was utilized to investigate the morphology of some of the samples in chapter 4. The samples' optical properties were analyzed using a UV-Vis spectrophotometer (Perkin-Elmer, Lambda 1050). The UV-Vis spectrophotometer was set on transmission mode for transparent and diffuse-reflectance spectra (DRS) mode for non-transparent samples. The crystallinity of the materials was determined using x-ray diffraction (XRD, Bruker-D8 Discover instrument) equipped with a sealed Cu Kα X-ray source (40 kV 44 mA, $\lambda = 0.15418$ nm) in the 2θ range of 10–80°. The vibrational properties of the samples were studied using a Raman spectrometer (Nd:YAG laser Raman Microscope, Nicolet Omega XR). The Raman spectrometer was equipped with a 532 nm laser source with an incident power of 10 mW, which was used to excite the samples.

The surface binding energies and the oxidation states of the elements were investigated using x-ray photoelectron spectroscopy (XPS) with Kratos Analytical-Axis-Ultra photoelectron spectrometer, which was equipped with a monochromatic Al-Kα source (15 kV, 50 W) and photon energy of 1486.7 eV. C1s with binding energy of ≈ 284.8 eV was chosen as the reference peak, and the binding energies of all the elements were corrected based on the C1s reference point. The synthesized materials' valence band positions and work functions were determined using ultraviolet photoelectron spectroscopy (UPS) equipped with an excitation source consisting of a 21.21 eV He lamp. The XPS depth profile was also measured using a PHI VersaProbe III Scanning XPS Microprobe equipped with an Ar^+ ion sputtering gun. The surface potential measurements were conducted using a Kelvin probe force microscopy (KPFM) equipped with an Atomic Force Microscope (Dimension FastScan, Bruker). The KPFM had two diode lasers sources centered at 520 nm and 635 nm.

2.3.CO_2 Photoreduction reaction and $^{13}CO_2$ labeling tests.

Experiments measuring the photoreduction of CO_2 were conducted using a 32 ml cylindrical shaped stainless steel flanged reactor equipped with a quartz window (Figure 8). The photocatalyst and a few water droplets were placed at the bottom of the reactor, following which the reactor was purged with 99 % purity CO_2 gas three times to remove residual air inside the reaction chamber and the tubing. The purged reactor was pressurized with 99% purity CO_2 gas to 50 psi (344738 Pascal) and subsequently placed on top of a hot plate set to 50 °C or 70 °C to evaporate the water droplets. To investigate the photocatalytic activity of the samples, the reactor was subjected to light irradiation. The light source used in these experiments was either a standard Class A solar simulator (Newport) with an intensity of 1000 W m^{-2} (one sun) or a U.V. lamp with its peak emission at 255 nm. The duration of irradiation was 2 hours. After the irradiation step, the products of the reaction were analyzed using a Shimadzu gas chromatograph (GC-2014, Figure 9) equipped with both Porapak Q and a molecular sieve column and a pulsed discharge detector (PDD). The carrier gas used was ultrahigh purity He. Each of the measurements was repeated three times, and the average of these three measurements was reported as the final result. Since it is impossible to purge all of the air from the GC after each run, the gas chromatogram always exhibits huge peaks for oxygen and nitrogen and a tiny peak for carbon monoxide (originating from the lab's atmosphere). Hydrogen or hydrocarbon mixtures of known composition were used to calibrate the output of the GC. The examples of the chromatogram of the products obtained from the GC measurements for each of the samples are shown in Figure 10. In addition to regular gas chromatography tests, a GC-MS was used to identify the products of the isotope labeling test using $^{13}CO_2$ instead of regular $^{12}CO_2$ gas. These tests were performed under identical reaction and illumination conditions, and their purpose was to verify that the hydrocarbon products originated from the reactant (CO_2) instead of carbon contamination.

Figure 8. Photograph of the high-pressure stainless still reactor used for the CO_2 photoreduction reactions. The volume of the reactor was 32 ml. A4 paper underneath the reactor is used for the purpose of scaling.

Figure 9. Photograph of the Shimadzu gas chromatograph (GC-2014) used for measuring the amount of hydrogen and hydrocarbons.

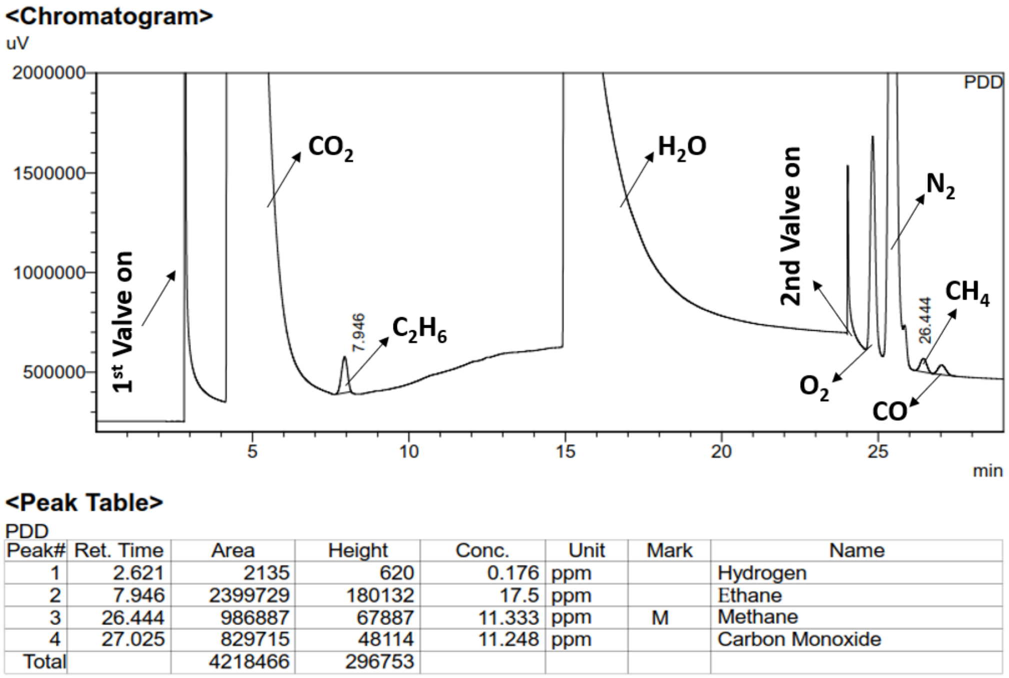

<Peak Table>

PDD

Peak#	Ret. Time	Area	Height	Conc.	Unit	Mark	Name
1	2.621	2135	620	0.176	ppm		Hydrogen
2	7.946	2399729	180132	17.5	ppm		Ethane
3	26.444	986887	67887	11.333	ppm	M	Methane
4	27.025	829715	48114	11.248	ppm		Carbon Monoxide
Total		4218466	296753				

Figure 10. An example of a gas chromatogram obtained by GC.

2.3.1. Conversion of GC peak areas to moles

The GC was calibrated with a standard cylinder with concentrations of 100 ppm methane and 100 ppm ethane. As a result, the reported chromatogram results are the areas that correspond to the ppm levels of the products. The ppm concentration of the product can be converted into mole fraction of product using the following formula:

$$M_{product} = \frac{ppm_{product}}{10^{+6}} \quad (9.)$$

$M_{product}$ is the mole fraction of the product's product in the reactor, and $ppm_{product}$ is the ppm value reported by the GC. Considering that the total pressure (P_{total}) in the reactor was 50 psi (3.45×10^5 Pa), using Dalton's law, the partial pressure of the product can be calculated using equation (10). After the partial pressure is obtained, the product's moles can be obtained using the ideal gas law (equation (11)).

$$P_{product} = P_{total} \times M_{product} \tag{10.}$$

$$n_{product} = \frac{p_{product} \cdot V}{R.T} \tag{11.}$$

Where V is the volume of the reactor (32 ml), R is the ideal gas constant (8.314 J mol-1K-1), and T is the reactor's temperature.

The selectivity toward production of methane or ethane were calculated using the following formula:

$$Methane/Ethane\ Selectivity = \frac{Amount\ of\ ethane\ produced\ (\mu mol)}{Total\ amount\ of\ products\ (\mu mol)} \tag{12.}$$

2.4. Photoelectrochemical water-splitting reaction, H_2 evolution, and Faradaic efficiency measurements.

The photoelectrochemical measurements were conducted using an electrochemical working station (CH Instruments, CHI660D) in a standard three-electrode electrochemical cell (Figure 11) containing a working electrode, a counter electrode, and a standard reference electrode. The fabricated photoelectrodes were used as working electrodes. Pt was chosen as the counter electrode, and a standard Ag/AgCl (0.1 M KCl) was used as a reference electrode. The electrolytes used for the experiments were an aqueous solution of 1 M Potassium Hydroxide (KOH) or Sodium sulfate (Na_2SO_4). The linear sweep voltammetry (LSV) measurements were conducted by sweeping the applied potential from -0.8 to +1 V, and the dark photocurrent was collected for the comparison purpose under the same condition. The photocurrent versus time (*I-t* measurements) was conducted either under the constant applied potential of +0.6 (photoanode) in a 1M aqueous KOH electrolyte or applied potential of -0.6 (photocathode) in a 1M aqueous Na_2SO_4 electrolyte. The scavenger test was conducted using the same procedure except that the solution was a 1M KOH in 10-volume percent methanol in water for the hole scavenger test. The Solar simulator used in these experiments was a standard Class A solar simulator (Newport) with an intensity of 100 mW cm $^{-2}$. A set of LEDs were also used as illumination light sources. The LEDs' output power intensity was calibrated to be 10 mW cm $^{-2}$.

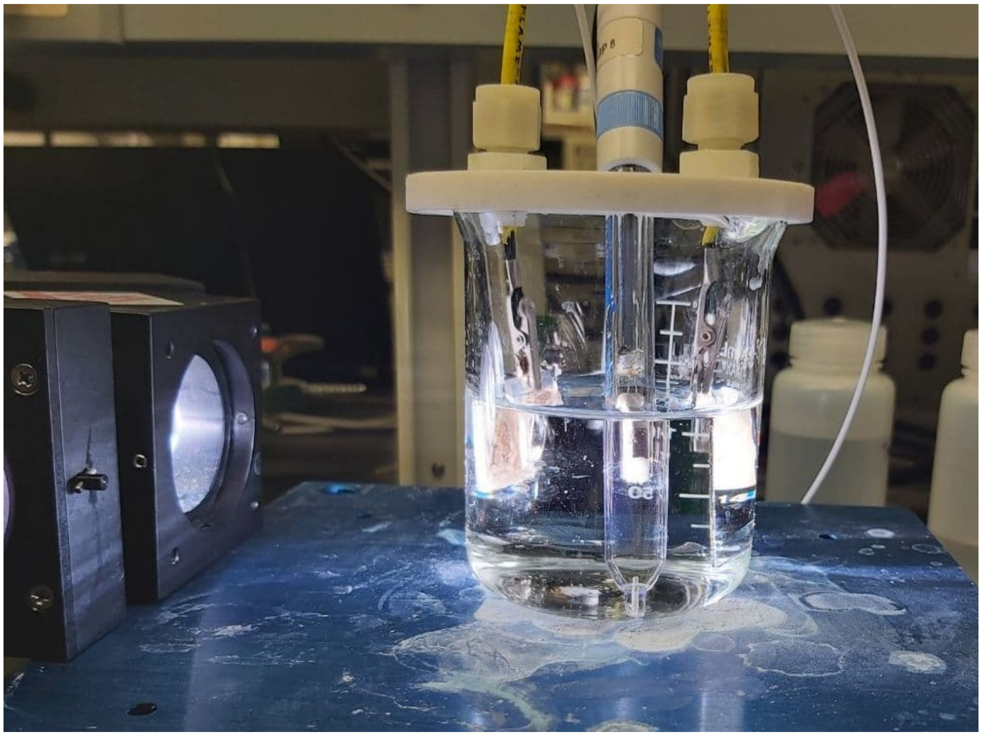

Figure 11. Photograph of the three-electrode electrochemical cell used for the photoelectrochemical water-splitting reaction.

The H_2 evolution was conducted in an H-Cell (Figure 12) made of borosilicate glass under standard 1 Sun illumination. The transmittance of borosilicate glass was calculated to be around 83 % at the wavelength ranging from 280 nm to 400 nm and 91 % at wavelengths ranging from 1120 nm to 2500 nm.[19] Based on these measurements, the loss associated with utilizing borosilicate glass instead of quartz is calculated to be around 4 %.

The electrolyte was a solution of 1 M KOH in water, the counter electrode was Pt, and the reference electrode was a standard Ag/AgCl electrode, the applied potential was fixed at +0.6 V. The experiment was conducted for 30 minutes after the experiments were finished the amount of H_2 produced at the counter electrode was measured using GC. The Faradaic efficiency, which is the ratio between the observed hydrogen in experimental condition to theoretical hydrogen evolution based on photocurrent value, was measured using the following equation:

$$Faradaic\ Efficiency = 100 \times \frac{H_2\ measured\ in\ actual\ reaction\ condition\ by\ GC(mol)}{\frac{J(Acm^{-2}).A(cm^{2}).T(Sec)}{2.e(C).N_A(mol^{-1})}} \qquad (13.)$$

Where J is the photocurrent density, A is the photoelectrode area, T is the irradiation time, e is the standard charge of an electron (1.602×10^{-19} C), and N_A is the Avogadro number (6.02×10^{23} mol^{-1}).

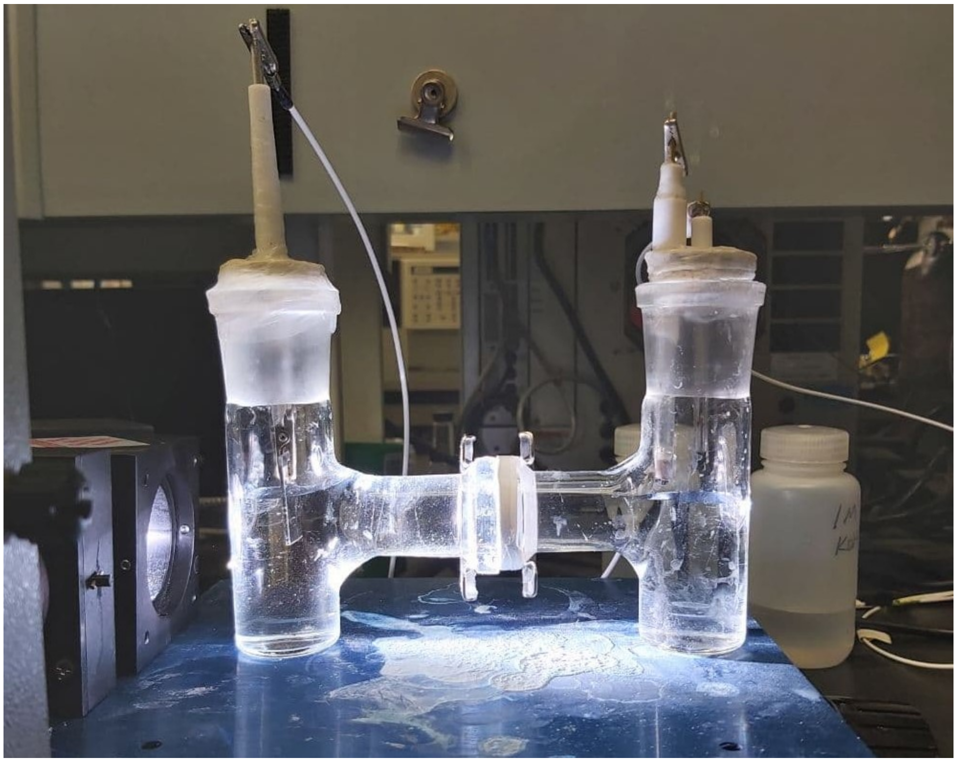

Figure 12. Photograph of the H-Cell used for H_2 evolution reaction.

2.5. Electrochemical Cyclic voltammetry and electrochemical surface area measurements

The cyclic voltammetry (CV) measurements were conducted in a standard three-electrode system. The electrolyte was an aqueous solution of 0.05 M Na_2SO_4. The CV experiments contain sweeping from 0 V to 1 V in the forward bias direction and sweeping backwardly in the reverse order; the scan rate was set to 0.1 V/s.

For calculation of the electrochemical surface area (ECSA) and specific surface area (SSA), firstly, roughness factor (RF) was calculated using the following formula:

$$\mathrm{RF} = \frac{\mathrm{q_{sample}}}{\mathrm{q_{reference}}} = \frac{ECSA}{Geometrical\ Area} \qquad (14.)$$

Where q_{sample} is the charge associated with the reduction of AuO from the samples and $q_{reference}$ is the charge related to the reduction of the smooth sample as a reference. The charge related to the reduction of each sample was calculated by integrating the area under the curve of the reduction of the sample during the reverse bias sweep divided by the scan rate. After calculation of the RF for each of the samples, the ECSA was calculated by multiplying it by the geometrical area of the sample, and SSA was calculated using the following formula:

$$\mathrm{SSA} = \frac{\mathrm{ECSA}}{\mathrm{w}} \qquad (15.)$$

Where w is the estimated weight of the sample.

2.6. FDTD Simulations

Finite-difference time-domain (FDTD) simulation is a powerful tool for investigating light/matter interaction. Like every finite difference method, FDTD solves a partial difference equation (PDE) called Maxwell's equations (equations 16 and 17) on the tiny grid cells (known as the Yee grids) of the structure.[20]

$$\Delta \times E = -\mu \frac{\partial H}{\partial t} \tag{16.}$$

$$\Delta \times H = -\varepsilon \frac{\partial E}{\partial t} \tag{17.}$$

In Maxwell's equations, E is the electric field, H is the magnetic field, μ is permeability, and ε is the permeability of the structure. The electric field and magnetic field are discretized in FDTD simulation. Each field component (E_x, E_y, E_z, H_x, H_y, H_z) will be simultaneously solved on the Yee grid, which allows us to obtain the far-field and near-field optical response of the structure. The FDTD method, in general, contains three major steps. The first step is the definition of the simulation environment and setting the boundary conditions. The three main boundary conditions in FDTD are perfectly matched layer (PML) to mimic the dissipation of the electric field, symmetric/antisymmetric boundary condition for reducing the computational cost of an object which has symmetry in its structure, and periodic boundary condition for simulation of a periodic structure. The second step is specifying the electromagnetic source; the primary electro magnetic sources used in the FDTD method are total-field scatter-field (TFSF) source, which comprises of two regions, the first region is called the total region, which contains the sum of the incident electric field and scattered electric field and the second region of it only contains the scatter electric field which is being called scatter region. TFSF is usually being used to determine the scattering and absorption cross-section of nanostructures. The second ubiquity-used electromagnetic source in the FDTD method is the plane wave representing the injection of a uniform electromagnetic wave inside the simulation environment. The plane wave is generally used for the simulation of periodic structures. The last step in FDTD simulation is the definition of the structure and setting of the materials. The materials are usually defined by their complex refractive index (n,k) in FDTD.

Lumerical software was used to implement the FDTD simulations. Using the graphical user interface (GUI) of lumerical, one can define materials with different shapes and structures even in nanoscale sizes. The simulation starts with the definition of the structures in the simulation environment. Based on the structure of the simulated object, if there was a symmetry in the structure in the X or Y direction, symmetrical boundary conditions or anti-symmetrical boundary conditions were introduced in the X and Y direction to reduce the computational cost of the simulations. Depending on the structure of the materials, either a TFSF source with a 250-800 nm bandwidth or a TFSF source with a 500-1200 nm bandwidth with 1000 frequency points was chosen as the light source. The far-field absorption cross-section of the structures was recorded using the proper monitor. The near-field electric field intensity was recorded using a frequency domain field and power monitor. The simulation was done using the same TFSF source two times to simulate the near-field electric field under an unpolarized light. The difference between these two simulations was the 90-degree difference in polarization of the TFSF source, the electric field obtained by these two simulations was averaged and reported. The monitors were set to obtain the electric field intensity at a single wavelength. Since TiO_2 is not a predefined material in the built-in Lumerical database, its refractive index was extracted from the literature[21] and imported into Lumerical. A uniform mesh size of 1nm was introduced in the simulations to ensure the results' accuracy.

2.7. Deposition of Au, Ag, and TiO_2 thin films

Deposition of Au and Ag thin films were implemented in a DC magnetron sputtering system (Kurt J. LeskerCo.) operating under a high vacuum (850 mTorr). Before the deposition, the Au or Ag targets were pretreated for 60 seconds. The deposition duration was 30 seconds for Au film and 15 seconds for Ag film. Deposition of amorphous TiO_2 layer was done on an ALD apparatus (Oxford Industries ALD, FlexAl), Titanium isopropoxide was used as the Titanium precursor, and oxygen plasma was the source of oxygen, the substrate temperature was set to 120 $^{\circ}$C, the chamber was firstly cleaned for 50 cycles to ensure the removal of the contaminations then the actual deposition was done, the deposition rate was 0.44 A$^{\circ}$/cycle.

3. A symmetric Multipole Plasmon-mediated Catalysis Shifts the Product Selectivity of CO_2 Photoreduction Towards C_{2+} Products.

In this chapter, the background information about the selectivity and activity of photocatalysts and strategies to improve the photocatalytic activity of a photocatalyst is presented. Bimetallic AgCu decorated TiO_2 nanotube array (TNTA) was fabricated and characterized, the results for the CO_2 photoreduction reaction are presented.

3.1. Background and motivation

The photoreduction of CO_2 to value-added products is currently a focus of tremendous research interest. The primary work of Inoue et al. in 1979 showed that CO_2[22] can be converted into useful products such as CO, CH_4, C_2H_6, HCOOH, CH_3OH, *etc.,* utilizing semiconductor photocatalysts such as TiO_2, ZnO, CdS, and GaP. The lack of product selectivity in CO_2 photoreduction is a major challenge that limits practical applications and industrial adoption of this technology.[23] The major products of this reaction are typically C_1 products such as CO and/or CH_4 and/or $HCOO^-$ (formate), but it has been reported that C_{2+} products (such as C_2H_6) can also be produced during the photoreduction process.[24-27] C_{2+} products are more interesting since they have a higher energy density and serve as precursors for a greater variety of industrial reactions thus generating more market value. For instance, ethane can be transformed into liquid fuels more easily than methane.[26, 28] The reaction mechanism involved in producing C_{2+} products is more complex and usually involves the C-C coupling reaction, which has a high activation energy barrier. It is noteworthy that the success achieved in the electrochemical CO_2 reduction reaction (CO_2RR) field in generating C_{2+} products such as ethylene and ethanol at yields of 60-90 % has not translated thus far into CO_2 photoreduction using similar material systems. Strategies used in CO_2RR to optimize C-C coupling and enhance the yield of C_{2+} products such as higher alkali metal cation concentrations in the electrolyte, higher pH near the electrode, higher electrolyte concentration of CO_2, running the reaction at higher overpotentials, *etc.* do not have direct counterparts in photocatalytic CO_2 reduction.[29-31]

The presence of a cocatalyst (mostly nanoparticles of transition metals such as Au, Ag, Cu, Pt, Pd, etc.) in a photocatalyst system offers several benefits, including increasing the light-harvesting ability of the photocatalyst through interband and intraband transitions in the metal nanoparticle, improving the separation of photogenerated charge carriers through the formation of a heterojunction interface, providing new sites for adsorption of reactant molecules on the surface of the photocatalyst, *etc.* Transition metals are known for improving the hydrogenation reaction rather than C-C coupling. The decoration of semiconductor photocatalysts with transition metal nanoparticles favor the production of methane compared to C_{2+} hydrocarbons.[28] Carbon dioxide anion radical ($CO_2{\cdot}^{-}$), electronically excited state of carbon monoxide (CO*), formyl radical (·CHO) and carboxyl radical (COOH) figure prominently as reaction intermediates in multiple pathways proposed for CO_2 photoreduction.[32, 33] Inter-adsorbate steric and dipole repulsion forces hinder the adsorption and C-C coupling of these reaction intermediates on adjacent reaction sites of metal atoms.[34] The interplay between attractive long-range forces and short-range Pauli repulsion and repulsive dipole-dipole coupling is well-studied for CO monolayers of various coverages on Cu(100), Cu(110), and Cu(111) surfaces.[35-37] Nanoparticles of Ag, Au, Cu, and Al exhibit strong localized surface plasmon resonances at visible wavelengths, consisting of coherent and collective charge density oscillations of conduction band electrons. Nanoparticles smaller than ~ 50 nm primarily exhibit a symmetric dipole resonance wherein optical excitation displaces the center of negative charge with respect to the center of positive charge due to the polarization of the electron cloud by the incident field.[38] The combination of adsorbate-adsorbate repulsion between reaction intermediates and symmetric distribution of surface charge due to dipolar LSPR excitation makes C-C coupling more unlikely on such metal nanoparticle surfaces. This may be why vapor phase CO_2 photoreduction on TiO_2 nanotubes surface-decorated by < 10 nm-sized nanoparticles of Cu, Pt, Ru, Au, Pd, AuPd, ZnPd, Ag, etc. has primarily been reported to result in the dominant formation (> 95% of all product molecules formed) of C_1 products such as methane, carbon monoxide, methanol, and formaldehyde, with C_2 products such as ethane and ethylene formed as minor by-products (<5% of all products).[39-46] In metal particles larger than 50 nm in size, the quasistatic approximation is no longer valid. The quadrupole plasmon mode becomes significant, which produces an antisymmetric distribution of charge density oscillations on the surface of the metal nanoparticle when excited.[47, 48] In even larger nanoparticles and aggregates of dissimilar nanoparticles, multipole plasmon excitations with rapidly alternating surface charge density oscillations dominate.[49] Multipolar plasmon resonance modes and symmetry breaking in heterodimers[50, 51] afford the possibility of closely-lying reaction sites having opposite charge, thus enabling a reduction in the dipole repulsion of adsorbed C_1 reaction intermediates and facilitating their C-C coupling to form C_2 products.

There are few reports on the production of C_{2+} hydrocarbons (more specifically ethane) in the CO_2 photoreduction process. Recently Sorcar et al. reported the production of ethane with 28% selectivity at a rate of 77 μmol gr^{-1} over a Pt-sensitized graphene-wrapped titania photocatalyst. Yu et al. reported a C-C coupling reaction on Au NPs with almost 40% selectivity for ethane production[24]. Our previous work in Angew. Chem. Int. Ed. on a Cu-Pt nanoparticle supported titania nanotube array photocatalyst exhibited a maximum 14% selectivity towards ethane formation.[25] In all the reported literature so far, the cocatalyst typically consists of one or more precious metals such as Pt, Au, Ru, and Pd.[39, 42, 52] Herein, we successfully synthesized large-sized, less expensive Ag, Cu, and AgCu nanoparticles, and successfully hosted these nanoparticles on a TiO_2 nanotube array (TNTA) scaffold. Our experiments demonstrate that the synergetic effect of large (> 80 nm) Ag and Cu nanoparticles as cocatalysts in CO_2 photoreduction increases both the efficiency and selectivity of CO_2 photoreduction, a C_2 product, namely ethane, is generated with an unprecedented selectivity as high as 60%. The critical conceptual innovation consists of the use of hybrid quadrupolar and multipolar plasmon resonances in large plasmonic nanoparticles and their aggregates to achieve an asymmetric photoexcited charge distribution on the photocatalyst surface.

3.2. Synthesis of TiO_2 nanotube arrays (TNTA), Ag-TNTA, Cu-TNTA, and Ag-Cu-TNTA

Figure 13 schematically depicts the fabrication process used to synthesize metal nanoparticle decorated TiO_2 nanotube arrays. Electrochemical anodization of Ti foils was used to obtain TNTA. Titanium foils were cut into smaller pieces (1 cm × 2.5 cm) and washed with methanol, water, and acetone thoroughly before the anodization process. An EG-based electrolyte containing 4% v/v water and 0.3 wt% NH_4F was used for anodization. The anodization was performed at room temperature under 40 V applied bias between the anode and the cathode (another Ti foil) for 3 hours. The anodized foils were washed with methanol and water and dried with nitrogen. The obtained TNTA were subsequently annealed at 450 °C for 3 hours to induce crystallinity.[53]

Two standard 2 mM solutions of $Ag(acac)_2$ and $Cu(acac)_2$ in methanol were prepared for depositing the metal nanoparticles. The prepared TNTA were immersed in a 2 ml solution of $Ag(acac)_2$ or $Cu(acac)_2$ (for preparing the Ag-TNTA and Cu-TNTA samples, respectively) and subjected to UV (365 nm) irradiation of a 4 W lamp for 3 hours. The synthesis procedure for preparing the AgCu-TNTA was similar except that the irradiated solution was 3 ml in volume consisted of a combination of 2 ml of $Ag(acac)_2$ and 1 ml of $Cu(acac)_2$ standard solutions (the molar ratio between Ag to Cu was adjusted to 2/1).

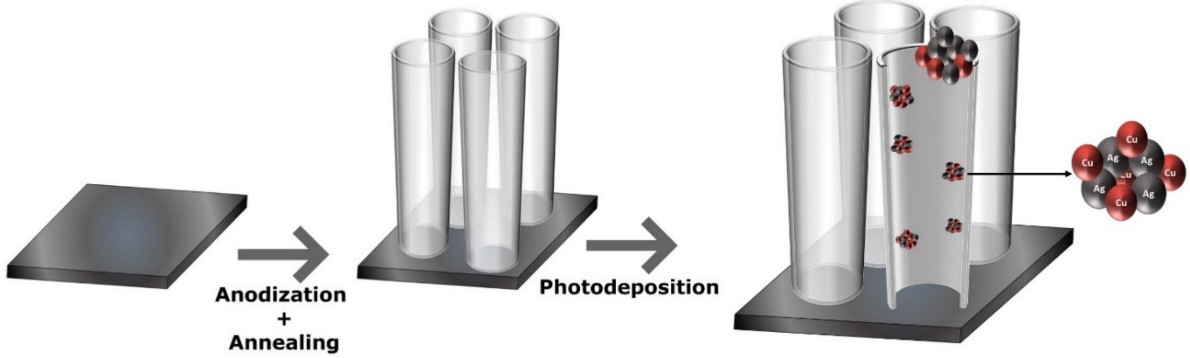

Figure 13. Schematic diagram of the fabrication process of AgCu-TNTA samples.

3.3. Results and Discussions

Electrochemical anodization was used to synthesize TiO_2 nanotube arrays (TNTA)[54, 55], and photodeposition from Ag(acac) and $Cu(acac)_2$ solutions[13, 56] was used to form monometallic and bimetallic nanoparticles (NPs) decorating and infiltrating the TNTA. The morphologies of TNTA were investigated using high-resolution transmission electron microscopy (HR-TEM) and field emission scanning electron microscopy (FESEM). The cross-sectional images of the TNTA (Figure 15a, Figure 15b, and Figure 14a) clearly show an array of hollow, vertically oriented nanotubes with an average length of ~ 6 µm and an average outer diameter of 110 nm. The top view of the AgCu-TNTA sample (Figure 14b and Figure 15a,b) shows 80-200 nm polydispersed nanoparticles of Ag and Cu agglomerated on the top of the TiO_2 nanotube arrays. From Figure 15a,b, it is evident that in addition to the aggregates of larger Ag and Cu nanoparticles on top of the nanotubes, there are smaller nanoparticles with diameters 25-80 nm compared to the inner diameter of the nanotubes, which penetrate along the length of the TNTA. Previous studies reported that bulk Ag and Cu exhibit lattice *d*-spacings of 0.208 nm and 0.240 nm, respectively, and the alloy of AgCu exhibits a *d*-spacing in the range 0.210 nm < *d* < 0.240 nm.[57] *d*-spacings of 0.350 nm and 0.240 nm were determined from selected area electron diffraction (SAED) patterns collected from higher magnification HR-TEM images (Figure 15c, d), and correspond to the (101) plane of anatase TiO_2 and FCC Ag(111). In some cases, a *d*-spacing of 0.22 nm was observed, indicative of the formation of AgCu bimetallic alloy through galvanic replacement.[57] The elemental map analysis of the area of interest in AgCu-TNTA sample is shown in Figure 15e which further confirms infiltration of the TiO_2 nanotubes with both Ag and Cu nanoparticles.

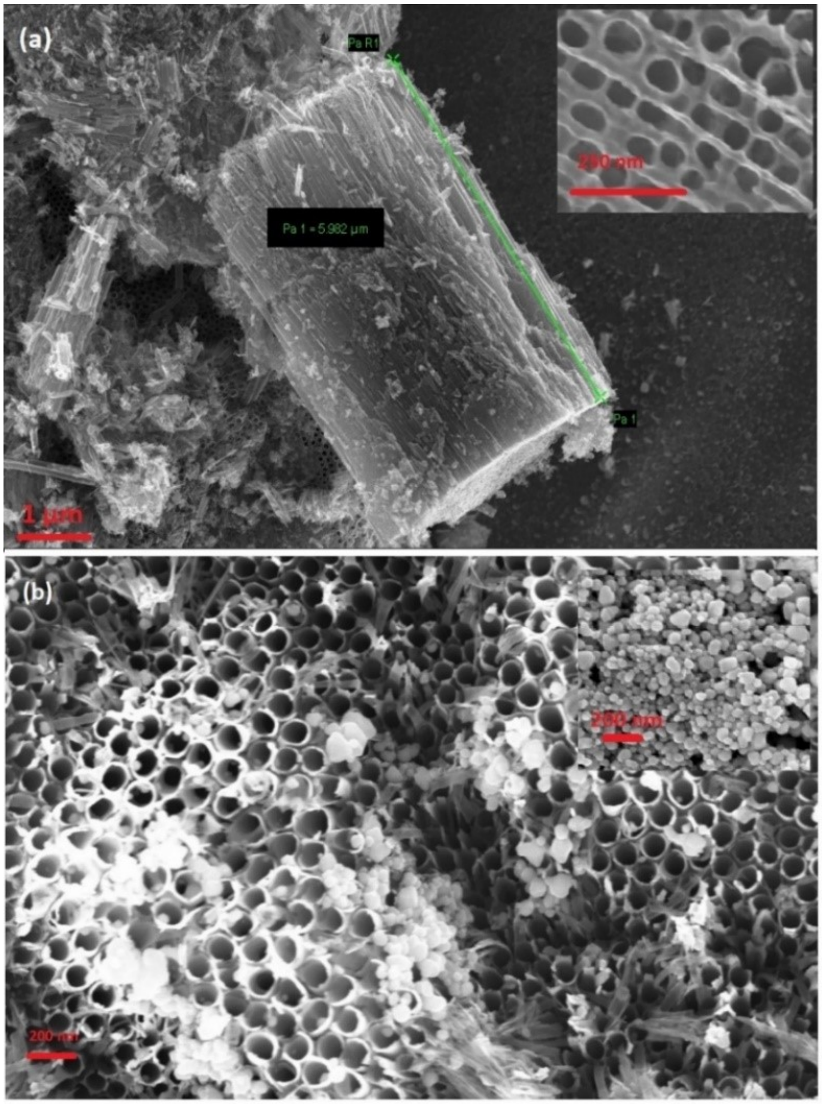

Figure 14. FESEM images of (a) TNTA and (b) AgCu-TNTA samples

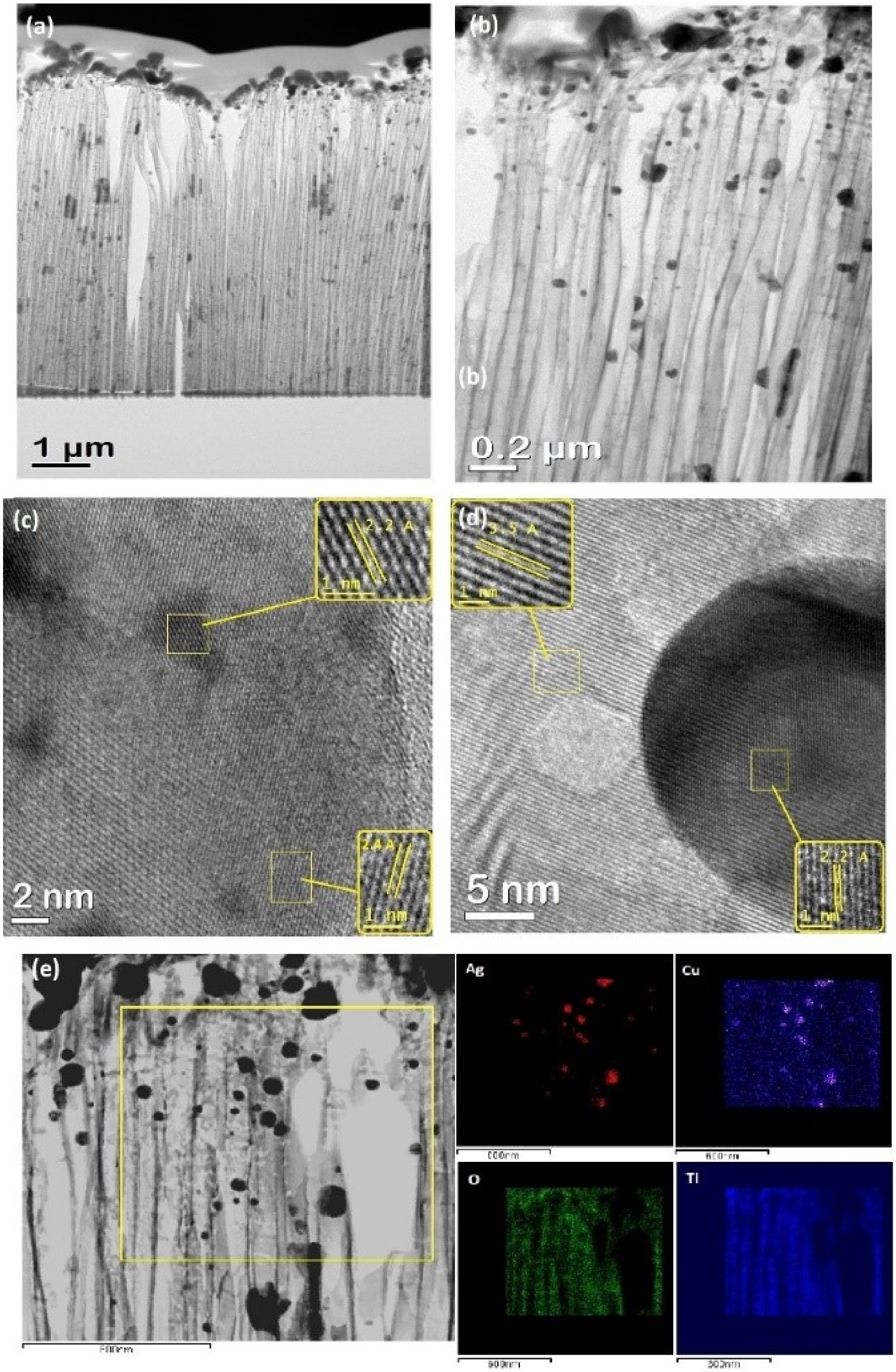

Figure 15. TEM analysis of AgCu-TNTA sample (a, b) Cross-sectional view (c, d) HR-TEM analysis of AgCu nanoparticles and corresponding d-spacings (e) Elemental mapping of AgCu-TNTA sample.

The X-ray diffractograms of TNTA, Ag-TNTA, and AgCu-TNTA are shown in Figure 16. The bare TNTA sample exhibited reflections corresponding to the pure anatase phase (JCPDS No. 21-1272). This is in agreement with prior reports that show the dominance of the anatase phase when anodic TiO_2 nanotubes are annealed at temperatures lower than 550 °C. The temperature of 450 °C used to crystallize the nanotubes is not high enough to induce the anatase-to-rutile phase transition. In addition to anatase peaks, other peaks originating from pure Ti could be detected in the XRD pattern of TNTA samples which corresponds to the portion of the titanium foil substrate that was not anodized. For the Ag-TNTA and AgCu-TNTA samples, additional peaks located at 2θ values of 44.08° and 64.3° are present in the diffractograms, which were indexed to face-centered cubic silver (JCPDS No. 04-0783). No peaks related to Cu could be detected in the XRD patterns of AgCu-TNTA and Cu-TNTA samples, indicating that the Cu nanoparticles were highly scattered. The amount of Cu was extremely small compared to Ag, Ti, and anatase TiO_2.[25] Consequently, it is reasonable to assume that the aggregated layer of large metal NPs seen in Figure 15 consists of a mixture of monometallic Ag and bimetallic AgCu NPs. However, the UV-vis spectra (to be discussed later) strongly suggest bimetallic AgCu NPs.

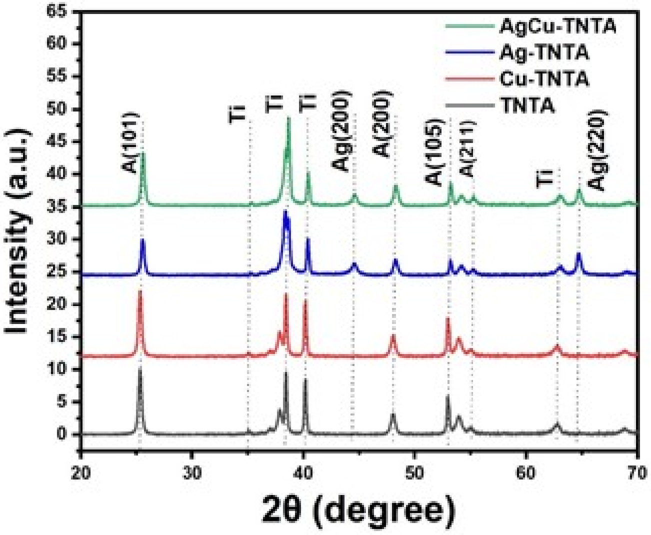

Figure 16. XRD patterns of TNTA, Cu-TNTA, Ag-TNTA, and AgCu-TNTs samples.

The Raman spectra of the TNTA, Cu-TNTA, Ag-TNTA, and AgCu-TNTA samples (Figure 17) exhibit one intense and three less intense peaks, which confirm phonon modes in tetragonal anatase TiO_2. The prominent peak at 145 cm^{-1} is due to the Eg mode, while less intense peaks at 395 cm^{-1}, 516 $cm^{-1,}$ and 640 cm^{-1} correspond to B1g, A2g, and Eg modes, respectively.[13] An expected shift and broadening for the main Eg modes in Raman spectra of Cu-TNTA, Ag-TNTA, and AgCu-TNTA has been observed, which is related to the changes induced in the structure of TNTA by the presence of Ag and Cu nanoparticles.[13]

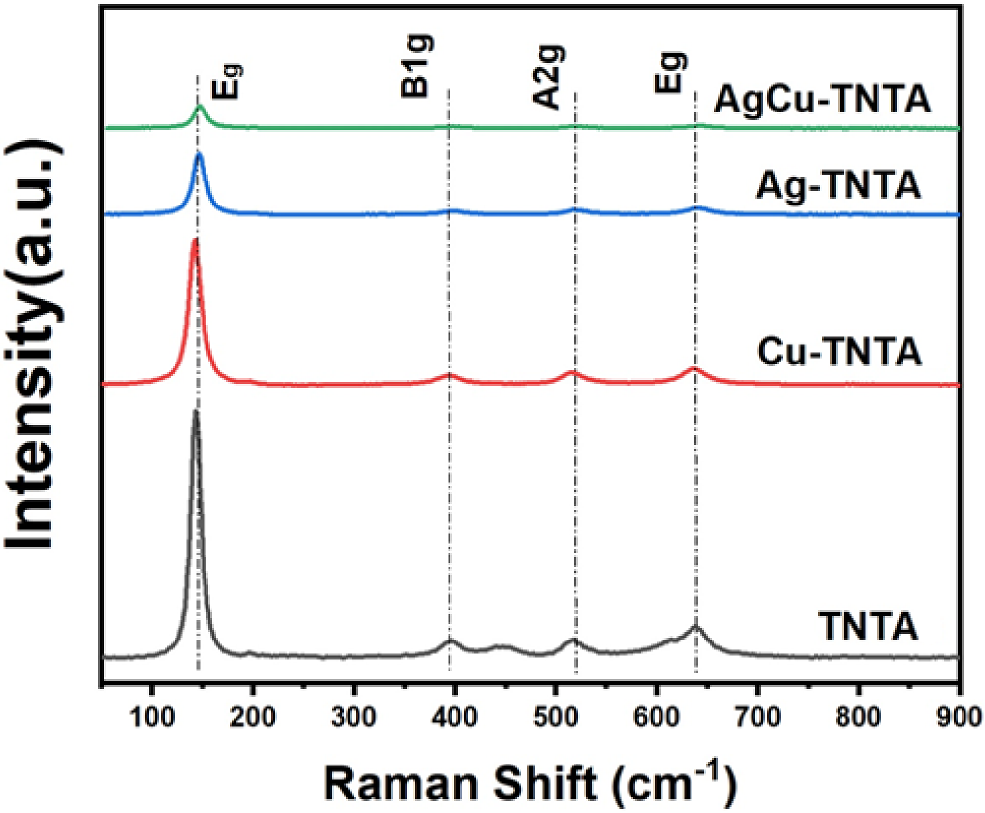

Figure 17. Raman spectra of TNTA, Cu-TNTA, Ag-TNTA, and AgCu-TNTA samples.

The chemical composition of the catalyst surface and sub-surface was determined using X-ray photoelectron microscopy (XPS) (Figure 18). The signature peaks of Ti, O, Ag and Cu are present in the XPS elemental survey scan (Figure 18a), confirming the successful photodeposition of Cu and Ag on the surface of the TNTA. The deconvoluted core-level high-resolution XPS (HR-XPS) spectra of TNTA and AgCu-TNTA samples in the Ti2p region exhibited two symmetric peaks located at binding energies (BE) of 458.96 and 464.84 eV, assigned respectively to the Ti2p$_{3/2}$ and Ti2p$_{1/2}$ peak components of Ti^{4+} ions present in TiO$_2$ crystal lattice (Figure 18b).[58-60] The obtained peak splitting between Ti2p$_{3/2}$ and Ti2p$_{1/2}$ peak components was found to be 5.88 eV, suggesting O^{2-} coordinated Ti^{4+} in TiO$_2$ lattice structure.[61, 62] The HR-XPS of TNTA in the O1s region can be deconvoluted into two chemically shifted components centered at BEs of 530.33 and 532.17 eV. The strong peak component at BE ~ 530.33 eV originated from the Ti bonded oxygens present in the crystal lattice (Ti-O-Ti), while the weak shoulder peak at 532.17 eV was attributed to surface bounded -OH and non-lattice adventitious oxygens (Figure 18c).[63-65] The binding energy of O1s peak components in AgCu-TNTA remains almost identical to TNTA, demonstrating that decoration of Ag and AgCu nanoparticles on TiO$_2$ nanotubes does not induce chemical changes on the surface. Two well-resolved Cu2p peaks for AgCu-TNTA at BEs of 932.63 and 952.65 eV (Figure 18d) originated due to Cu2p$_{3/2}$ and Cu2p$_{1/2}$ peak components of metallic Cu(0).[66, 67] The absence of any shoulder or satellite peak indicates the absence of any Cu^{1+} or Cu^{2+} oxides. The Ag3d spectra (Figure 18e) of AgCu-TNTA showed two peaks at 368.08, and 374.13 eV with 6.08 eV peak splitting corroborated to Ag(0), and the absence of shoulder peaks verified phase-pure metallic silver.[68, 69]

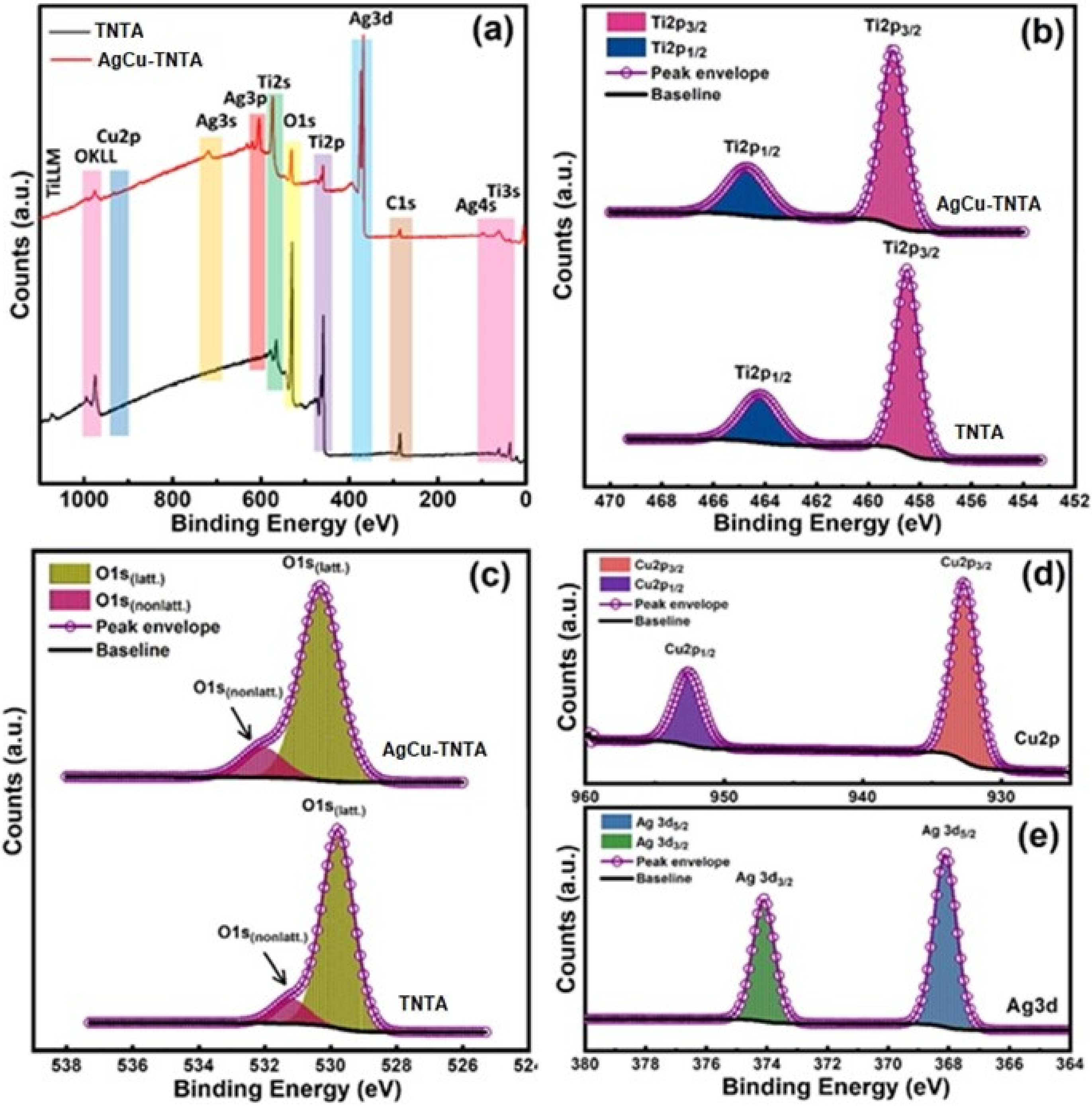

Figure 18. (a) XPS elemental survey scan of compact TiO_2 nanotubes arrays (black) and AgCu-TNTA (red) and core-level HR-XPS spectra of TNTA and AgCu-TNTA in (b) Ti2p region, (c) O1s region (d) Cu2p region, and (e) Ag3d region.

The optical properties of the TNTA, Cu-TNTA, Ag-TNTA, and AgCu-TNTA samples were investigated by diffuse-reflectance UV-Vis spectroscopy (DRS), as well as finite difference time domain (FDTD) electromagnetic simulations. The DRS spectrum of the TNTA sample (black line in Figure 19) exhibits a band edge around 380 nm, which is in accordance with its calculated band gap using Kubelka-Munk function (Figure 19b).[70] The band gap of Cu-TNTA, Ag-TNTA and AgCu-TNTA was calculate to be 3.27 eV, 3.75 eV and 3.7 eV respectively (Figure 19c,d,e). In comparison with the bare TNTA sample, the band-edge(s) for Ag-TNTA, Cu-TNTA, and AgCu-TNTA samples were blue-shifted to lower wavelengths. This blue shift is due to the Mie scattering of ultraviolet photons by metal nanoparticles.[71] In Figure 19, the optical spectra of Ag-TNTA and AgCu-TNTA samples resemble each other to some extent. For the Ag-TNTA sample, there is a broad, featureless localized surface plasmon resonance (LSPR) peak centered at 475 nm, which agrees with the polydispersed nature of Ag NPs fabricated in this study. The AgCu-TNTA sample exhibits two LSPR peaks at 425 nm and 525 nm. The 425 nm peak is due to the hybrid quadrupolar resonance of larger Ag NPs of size > 75 nm[48, 51] that is likely redshifted by 50 nm from Ag nanoislands' corresponding resonance to the higher permittivity of the TiO_2 nanotube array scaffold.[72] The 525 nm peak corresponded to the dipolar resonance of AgCu NPs in the vicinity of TiO_2 and weakened in amplitude by the interband damping of Cu.[48] The optical spectra indicate the AgCu-TNTA samples to be less polydispersed than the Ag-TNTA samples, which we attribute to the nucleation of Cu on Ag NPs and the etching of already agglomerated particles by galvanic replacement. The much lower scattering amplitude for AgCu NPs (green curve in Figure 19) due to damping provides persuasive evidence for the dominant presence of bimetallic AgCu nanoparticles over monometallic Ag NPs. The galvanic replacement by Cu^{2+} ions reduces the size of the Ag nanoparticles and also makes an alloy hybrid of the two materials.[57]

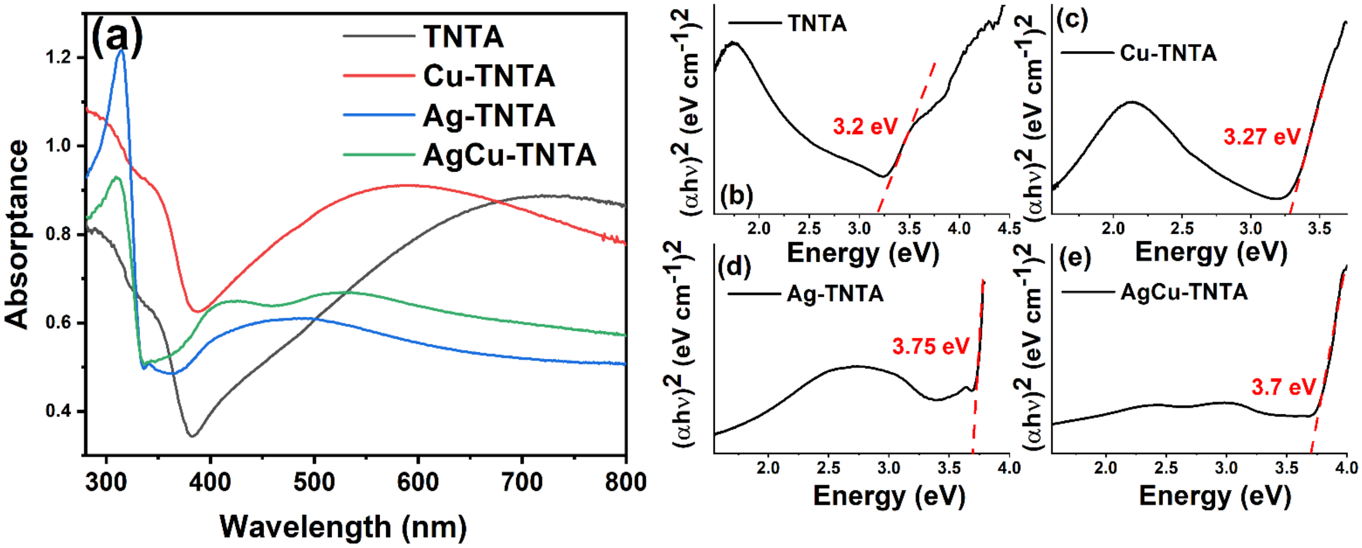

Figure 19. (a) DRS spectra of TNTA, Cu-TNTA, Ag-TNTA, and AgCu-TNTA samples and the calculated band gaps of (b) TNTA, (c) Cu-TNTA, (d) Ag-TNTA, and (e) AgCu-TNTA samples using Kubelka-Munk function.

We used finite-difference time domain (FDTD) electromagnetic simulations to study the interaction of light with TiO_2 nanotubes decorated with a single layer of Ag@Cu NP homodimers perched on top of the pore openings. The simulated optical properties of the dimers were used to obtain more general insight into the behavior of the aggregated nanoparticles on the surface of TNTAs. The diameter of the silver core was kept constant at 100 nm, and the thickness of the copper shell was set to 5 nm. Figure 20a exhibits the simulated electric field intensities of the AgCu-TNTA sample under broadband excitation (250 nm – 800 nm). Due to the strong interband damping-mediated absorption of Cu, TNTAs decorated with Ag@Cu homodimers exhibit significant visible light absorption. The strong damping due to the presence of Cu also ensures that the highest electric field intensities are found not in-between the two particles constituting the dimer but rather at Ag–TiO_2 and Ag–air interfaces. In addition, since the electric field was measured for a broad range of wavelengths from UV (250 nm) all the way to the visible (800 nm), electromagnetic radiation could couple with both TNTA and AgCu nanoparticles. The top view and cross-sectional profile electric field intensities at two chosen wavelengths on- (525 nm) and far from- (350 nm) LSPR resonance were also simulated; the results are shown in Figure 20b,c,d,e. For the excitation under LSPR (525 nm, Figure 20b,d), a strong electric field right at the interface between the two plasmonic nanoparticles is generated. This intensified electric field known as hotspot provides multiple benefits for a photocatalytic system, including LSPR-powered electron-hole generation, local heating effect, polarization of the reactants, and enhanced light absorption.

In comparison, the excitation under 350 nm (of resonance) did not produce a strong electric field which evidences the contribution of LSPR on the generation of hot spots at the interface. In addition, the electric field profiles in Figure 20d,e clearly shows that the electromagnetic wave did not couple with the TNTA at these two wavelengths. This is a well-studied phenomenon in TNTA. The TNTA can accommodate waveguide modes only when their diameter is bigger than the wavelength of the incident electromagnetic wave; also, when the wall thickness of the TNTA is significantly smaller than the wavelength of the light, its walls act as Rayleigh scattering elements.[73] In both of the simulations reported here, the TNTA (100 nm) diameter and the wall thickness (20 nm) are smaller than the wavelength of the light, so such a coupling did not happen.

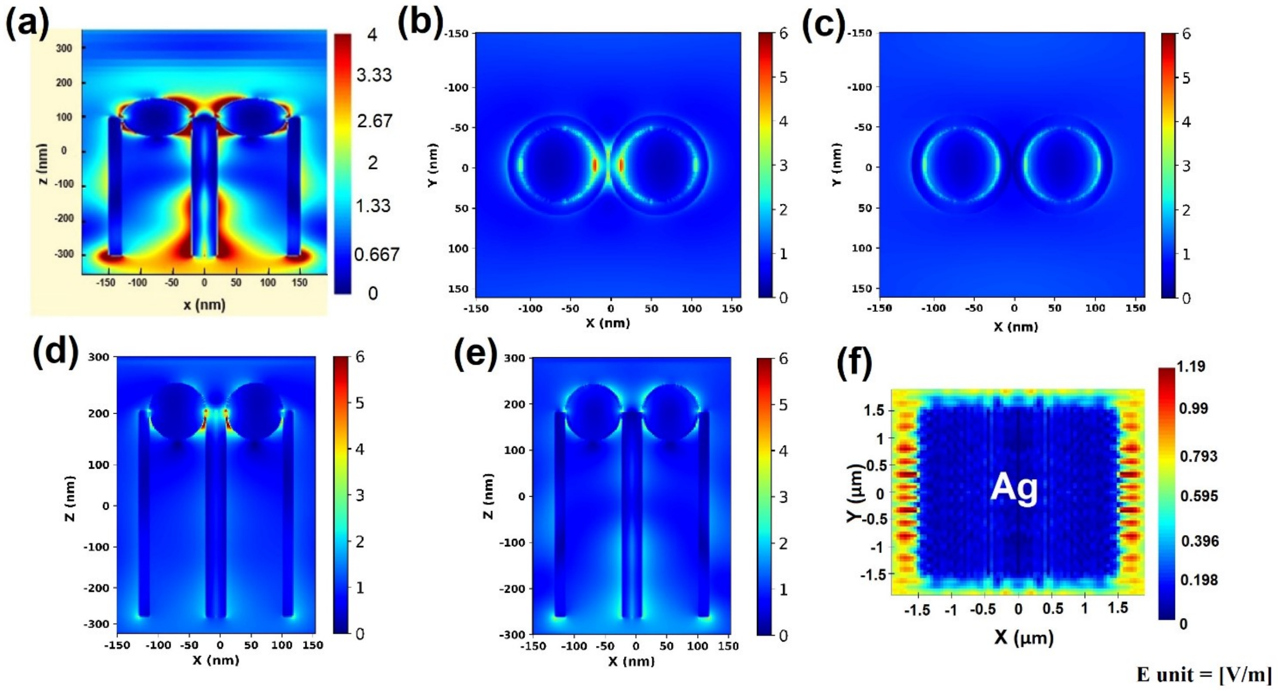

Figure 20. Electric field profile for a TNTA/100 nm Ag core–5 nm Cu shell homodimer with a 3 nm edge-to-edge spacing (a) ZY plane under broadband excitation (b) XY plane under 525 nm excitation (c) XY plane under 350 nm excitation, (d) ZY plane under 525 nm excitation and (e) ZY plane under 350 nm excitation. For comparison, the electric field profile on the XY plane at the interface between a 3µm×3µm slab of Ag on TiO_2 under 525 nm excitation is shown (f).

To prove the validity of our simulations, I have compared these results with the simulations reported in the literature. Figure 21a exhibits the calculated absorption spectra for Au, Ag and Al heterodimers with 1 nm spacing in medium with different refractive indices. For the refractive index of 1.5 which is close to the refractive index of TNTA, the simulation shows two peaks one centered at 430 nm and the other one centered at 530 nm which is comparable with the UV-vis spectra obtained for AgCu-TNTA sample (Figure 19a) which exhibited two plasmonic peaks one centered at 425 nm and the other one at 525 nm. Figure 21b,c exhibits the near-field electric field at a plasmon resonance wavelength in XZ-plane for Au and Ag homodimers respectively, these simulations exhibit an intense electric field right at the interface which is consistent with my simulations in Figure 20b,d.

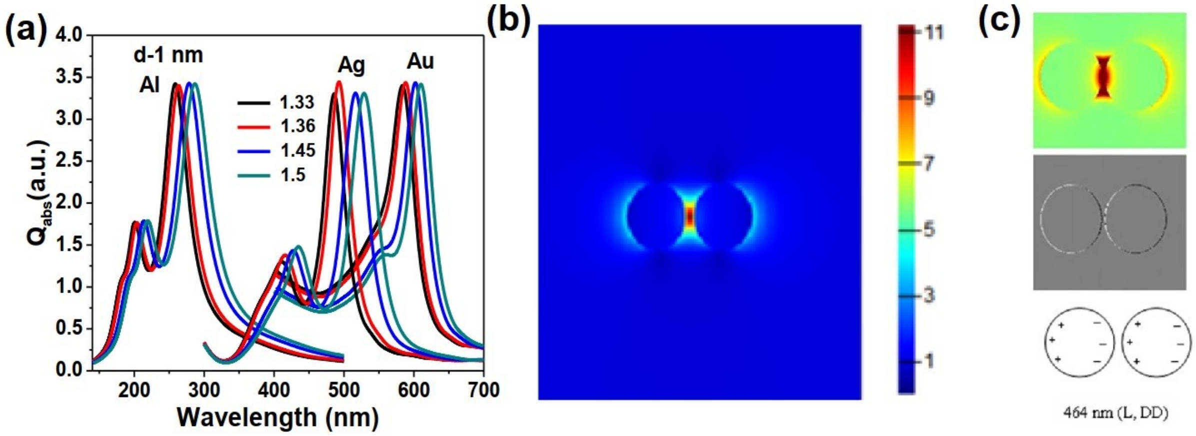

Figure 21. (a) Simulated absorption spectra of Au, Ag and Al homodimers (with 20 nm particle size and the interparticle spacing is 1 nm) in medium is with different refractive indices. Reprinted from Katyal et al. Advanced Electromagnetics (2018) with permission under Creative Commons Attribution.[74] (b) The near-field electric field profile at plasmon resonance wavelength in XZ-plane for Au homodimer. Reprinted from Katyal et al. Advanced Electromagnetics (2018) with permission under Creative Commons Attribution.[74] (c) electric field profile and surface charge distributions for a D=60 nm silver nanoparticle homodimer excited at its plasmon resonance. Reprinted from Chen et al. AIP Advances (2011) with permission under Creative Commons Attribution.[75]

Surface plasmons occur at metal-dielectric interfaces and are coupled to electromagnetic waves with both transverse and longitudinal components.[76] Due to the presence of the longitudinal component, both energy (i.e., finding photons or electrons of the right energy to excite the electron plasma) and tangential momentum conservation conditions need to be satisfied for the excitation of surface plasmons. Therefore, surface plasmon polaritons in metallic thin films cannot be simply excited with conventional illumination from an adjacent dielectric.[76] Unlike thin metal films, the conditions for plasmon excitation are easily met in the visible and near-infrared (NIR) spectral bands for < 100 nm-sized nanoparticles made of Ag, Au, Cu, Al, conductive transition metal nitrides, quasi-metallic degenerate oxides, and select degenerate chalcogenides (e.g., Cu_2S).[38, 77, 78] Surface plasmons undergo various ultrafast damping processes, including Landau damping, surface scattering, chemical interface damping and radiative damping.[79, 80] For nanoparticles in the 10-40 nm size range, Landau damping is the dominant mode of plasmon dephasing. Two regimes of Landau damping can be distinguished for surface plasmons[81]: (i) An interband damping regime wherein the bulk of the plasmon energy is transferred to hot holes and the hot electrons have energies < 1 eV above E_F. The produced hot electron-hole pairs are short lived with mean free path of < 5 nm. Interband damping is associated with a d→s electronic transition, and (ii) An intraband damping regime wherein longer-lived hot carrier pairs are produced with mean free paths as high as 40 nm and energies of 1-2 eV above E_F. Intraband damping is associated with s→s electronic transitions.

The strong electric field generated at the interface of AgCu and TNTA can be attributed to LSPR excitation.[82] To rule out the contribution of light absorption in the hot spot generation, we decided to simulate the electric field distribution at the interface between a slab of Ag and TiO_2. In this simulation, the sizes of the Ag and TiO_2 slabs were intentionally chosen in micrometers to negate the effect of the LSPR since LSPR happens only when the size of the structure is smaller than the wavelength of the incident irradiation. As shown in Figure 20f, the electric field intensities at the interface of Ag and TiO_2 are almost six times lower than the electric field intensities at the interface of AgCu and the TNTA structure. In addition to that, the production of hot carriers in metal films and nanoparticles cannot be separated from the collective (plasmonic) interaction of the free electron gas in the metal with the electromagnetic field of incident light. The frictional dissipation during the acceleration and deceleration of the electron gas in the metal by the applied oscillating electromagnetic field of light manifests itself as optical absorption. Landau damping is a mechanism guaranteed to occur in matter-waves that, in the case of metals, results in the plasmon (bulk or surface) losing its coherence to the electron-hole continuum.[83, 84]

The photocatalytic activities of Cu-TNTA, Ag-TNTA, and AgCu-TNTA samples were investigated under identical conditions involving two hours of illumination by AM1.5G simulated sunlight at 50° C. Immediately following illumination, the reaction products were analyzed by gas chromatography. The amounts of reaction products are reported in this work as micromoles of gas products per gram of photocatalyst per duration of the test (μmol gr^{-1} hr^{-1}). The results of the photoreduction tests are shown in Figure 22a, whose inset shows the total hydrocarbon production by the samples. The main reaction product was ethane (C_2H_6) for AgCu-TNTA samples, while methane was the main product for the Ag-TNTA and Cu-TNTA samples. The total rate of hydrocarbon production (methane + ethane) of 23.88 μmol gr^{-1} hr^{-1} was highest for AgCu-TNTA samples. The C_xH_{2x+2} production rate for Ag-TNTA and Cu-TNTA samples were 6.54 and 1.8 μmol gr^{-1} hr$^{-1,}$ respectively. The ethane selectivity for these three samples is shown in Figure 22b. The selectivity was highest for the AgCu-TNTs sample (60.7%), while the ethane selectivity was calculated to be 15.9% and 10% for Ag-TNTA and Cu-TNTA, respectively. The highest selectivity of ethane for the AgCu-TNTA sample and the fact that ethane was the primary product of CO_2 photoreduction for this sample indicates the synergistic effect between the Cu and Ag cocatalysts was responsible for the dominant production of ethane.

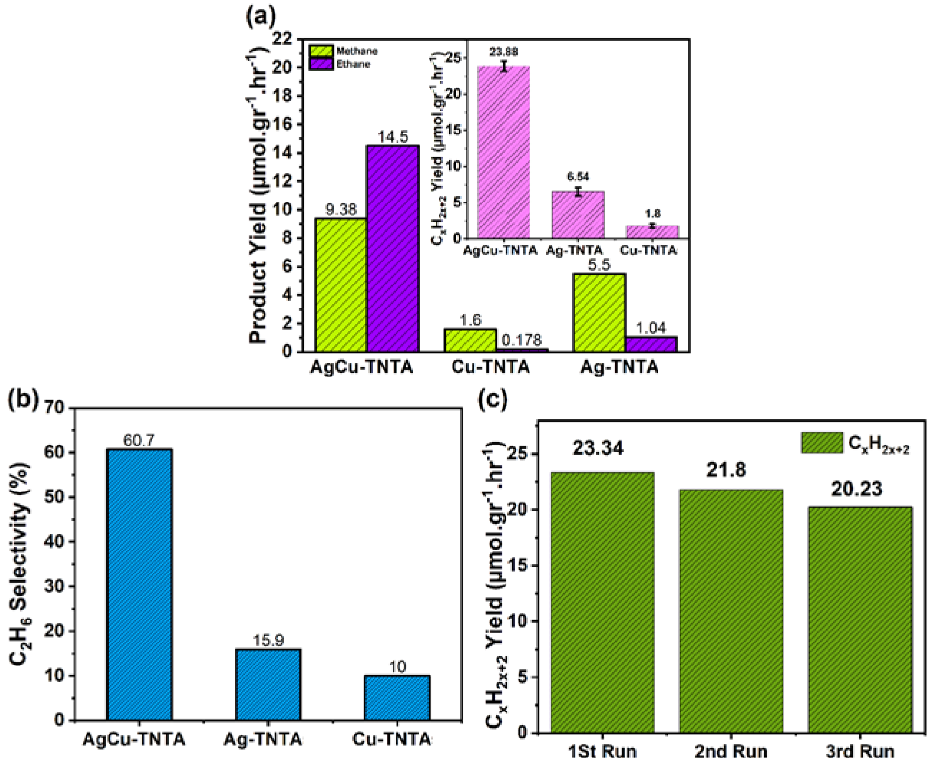

Figure 22. Reaction products under irradiation with AM1.5G one sun simulated sunlight (b) Comparison of the ethane selectivity using Cu-TNTA, Ag-TNTA, and AgCu-TNTA photocatalysts (c) Reusability test of AgCu-TNTA sample for CO_2 photoreduction reaction under standard condition.

Figure 22c exhibits the reusability of the best performing photocatalysts (AgCu-TNTA) during three consecutive runs; AgCu-TNTA photocatalyst still maintained a high level of photocatalytic activity during the 2nd and 3rd run with around 7 % decrease in performance.

A comparison between the photocatalytic activity of AgCu-TNTA with some of the previously reported literature on TiO_2 photocatalysts decorated with Ag or Cu nanoparticles was made (Table 1). It is evident from this table that the AgCu-TNTA sample reported in this work outperforms most of the previously reported Ag or Cu decorated TiO_2 photocatalysts.

Table 1. Comparison between the photocatalystic performance of AgCu-TNTA sample with previous literature

Sample	Light Source	Products (µmoles/gr hr)	Reference
Ag-TiO_2	Xe lamp (300 W)	1.4 Methane	85
Ag-TiO_2	365nm -UVA lamp (8 W)	2.64 Methane	86
Ag-TiO_2	Solar Simulator (AM 1.5)	4.93 Methane	87
Cu-TiO_2	Xe lamp (200 W)	5.4 CO 8.7 Methane	88
Cu-TiO_2	Xe lamp (300 W)	13.6 CO 1 Methane	89
Cu-TiO_2	UV Light	2.35 Methane	90
AgCu-TNTA	Solar Simulator (AM 1.5)	9.38 Methane 14.5 Ethane	This Work

The causes for the higher selectivity toward ethane compared to methane can be explained by looking into the carbene reaction pathway, which is widely agreed to be the mechanistic route for CO_2 photoreduction on nanoporous/nanotubular TiO_2 surfaces.[70, 91, 92] Depending on the CO_2 adsorption mode and the amount of energy provided by the charge carriers, CO_2 reduction can go through two different reaction pathways – the carbene pathway, in which the main product is methane and/or ethane and the formaldehyde pathway which formaldehyde itself is one of the main reaction products/intermediates.[5, 93, 94]

The carbene pathway can be written as follows:

$$CO_2 \xrightarrow{e-} \cdot CO_2^- \xrightarrow{e^-+H^+} CO + OH^- \xrightarrow{e-} \cdot CO^- \xrightarrow{e^-+H^+} C + OH^- \xrightarrow{e^-+H^+} \cdot \mathrm{CH} \xrightarrow{e^-+H^+} CH_{2*} \xrightarrow{e^-+H^+} \cdot$$

$$CH_{3*} \begin{cases} \xrightarrow{e^-+H^+} CH_4 \\ \xrightarrow{\cdot CH_{3*}} C_2H_6 \end{cases} \qquad (16.)$$

The overall reaction for methane and ethane can be written as:

$$CO_2 + 8H^+ + 8e^- \rightarrow CH_4 + 2H_2O \qquad (17.)$$

$$2CO_2 + 14H^+ + 14e^- \rightarrow C_2H_6 + 4H_2O \qquad (18.)$$

The photocatalytic conversion of CO_2 to hydrocarbons through the carbene pathway is a complex reaction with several intermediates. The methyl radical ($\cdot CH_{3*}$) plays an important role in the selectivity of the reaction. It requires 14 electrons to produce ethane from CO_2, while it requires 8 electrons to produce methane, thus making the ethane production significantly more complicated. A photocatalyst that can stabilize methyl radicals and provide many electron hole pairs is more successful in ethane production. If a $\cdot CH_{3*}$ reacts with a proton, the product is methane. On the other hand, ethane can be formed by the dimerization of two $\cdot CH_{3*}$ radicals. It has been suggested that the Cu^+ sites on a photocatalyst can stabilize the $\cdot CH_{3*}$ radicals and make the formation of ethane more favorable.[71, 95, 96] Interestingly, our results show that ethane can be produced with higher selectivity through CO_2 photoreduction by Ag-TNTA samples compared to Cu-TNTA samples, which provides empirical evidence that Ag also enables the production of ethane by stabilizing the methyl radical. Since the selectivity is higher (Figure 22b), we deduced that the Ag cocatalyst could stabilize methyl radicals even better than Cu. Here, we note that Ag co-catalyst is known to lower CH_4 production and increase C_{2+} selectivity in the Fischer-Tropsch reaction.[97] The highest selectivity of ethane for AgCu-TNTA samples proves that the synergistic effect between the Ag and Cu in AgCu bimetallic cocatalyst can boost methyl radical stabilization and pave the way for the dominant production of ethane in the CO_2 photoreduction process.

To gain insight into the electronic band structure and charge migration mechanism, work function (WF) and valence band (VB) spectra of TNTA and AgCu-TNTA were investigated using ultraviolet photoelectron spectroscopy (UPS) (Figure 23 and Figure 24). The work function value was estimated from work function spectra using the expression WF (ϕ) = $21.21-E_{\text{cut-off}}$, where 21.21 eV is the energy of the incident, He I line of a He discharge lamp, and $E_{\text{cut-off}}$ is the cut-off energy of secondary electrons. After extrapolating the linear region of the graph on horizontal and vertical regions, the intersecting points give the cut-off energy of secondary electrons ($E_{\text{cut-off}}$). The $E_{\text{cut-off}}$ values for compact TNTA and AgCu-TNTA were calculated to be 17.06 and 16.41 eV, and the associated WF values (ϕ) were determined to be 4.15 and 4.80 eV, respectively (Figure 23). Since the work function represents the position of the Fermi level with respect to vacuum, we found that the Fermi level of TiO_2 was downshifted following decoration of Cu, Ag nanoparticles on TiO_2 nanotube arrays, demonstrating the formation of a Schottky junction. Further, valence band maxima calculated from the intersecting point of the extrapolated linear region of the graph for TNTA and AgCu-TNTA were found to be 3.20 and 1.43 eV below the Fermi level (Figure 24).

To understand the mechanism of charge separation, the band diagram of the AgCu-TNTA sample is schematically depicted in Figure 25. The formation of a Schottky junction at the interface of the TNTA and the AgCu nanoparticles creates a depletion region in TiO_2 concomitant with an upward bending of the bands. I estimate the magnitude of the band-bending to be at least 1.2 V, in line with prior reports. In addition, considering a 10 nm space charge region between the AgCu and TNTA, the magnitude of the internal electric field intensity between the AgC u nanoparticles and the TNTA was estimated to be around $(4.6-4)/(10\times10^{-9}) = 6\times10^{7}$ V/m. Many reports have previously measured the electron density in anodically formed TiO_2 nanotube arrays to be 10^{18}-10^{20} cm^{-3},[98] indicating the titania to exhibit near-degenerate *n*-type semiconducting behavior. The valence band maximum confirms this in Figure 23 to be 3.2 eV below the Fermi level, almost equal to the bandgap of anatase TiO_2, thus implying that the Fermi level in TiO_2 coincides with the conduction band edge (implying degenerate *n*-type doping). Taken together, the combination of high built-in potential and a large electron density TiO_2 indicate a powerful interfacial electric field. The formation of the Schottky junction at the interface and a strong internal electric field is beneficial for the photocatalytic activity of the sample as the internal electric field can increase the charge separation. In the Schottky barrier band alignment, the electrons from metal nanoparticles can get injected into the semiconductor leaving the holes behind inside the metal nanoparticles.[13, 71]

Even though the UPS measurements suggest an upward band bending at the interface, there is another widely accepted hypothesis in the literature which indicates that the metallic nanoparticles can act as an electron sink (trap). The conventional belief is that the metallic nanoparticles can accept the electrons from the TiO_2 semiconductor. The CO_2 photoreduction occurs on the reactants adsorbed on the metallic nanoparticle surface, a phenomenon termed 'Schottky Barrier Electron Trapping' in the literature (Figure 25b).[13] However, the metallic electron sink explanation is unlikely to be true for our AgCu-TNTA photocatalyst since the presence of the internal electric field in the direction implied by Figure 25a would direct photogenerated electrons toward TiO_2 and holes toward the bimetallic nanoparticles.

The resulting determination of the interfacial band structure confirmed the presence of a Schottky junction in AgCu-TNTA with a concomitant depletion region and built-in potential exceeding 1.2 V (Figure 25a and Figure 25b). Since the number of electron transfer steps required for ethane formation is almost double that required for methane generation, carrier recombination losses are known to cripple ethane production and shift the product selectivity toward C_1 products.[28] The strong built-in electric field at the interface reduces recombination losses by facilitating photogenerated charge carriers' separation.[13, 99] This, in turn, enables the high photocatalytic activity observed in this work and preserves the selectivity for ethane formation (i.e., C_2 product). Hot electrons produced in the metal NP by plasmon decay are injected over the Schottky barrier into TiO_2, where they possess unusually long lifetimes due to the long dielectric relaxation time and low hole concentration of TiO_2.[38, 100, 101]

The resulting positively charged metal NP (due to the residual hole) is a powerful stabilizer of the methyl radical.[102] The $Cu\text{-}CH_3^+$ metal ion stabilized methyl radical has a measured lifetime of at least 50 μs. Metal-carbon bond dissociation energies of 288 kJ mol^{-1} and 177 kJ mol^{-1} have been calculated for $Cu\text{-}CH_3$, and $Ag\text{-}CH_3$ respectively.[102, 103] Hot spots with a high local electric field have been suggested to favor the formation of C_{2+} products in CO_2RR.[29] The plasmonic architecture of AgCu-TNTA samples enables such hot spots where intense local electric fields can polarize CO_2 molecules. We surmise that these hot spots favor C_{2+} products in CO_2 photoreduction as well.

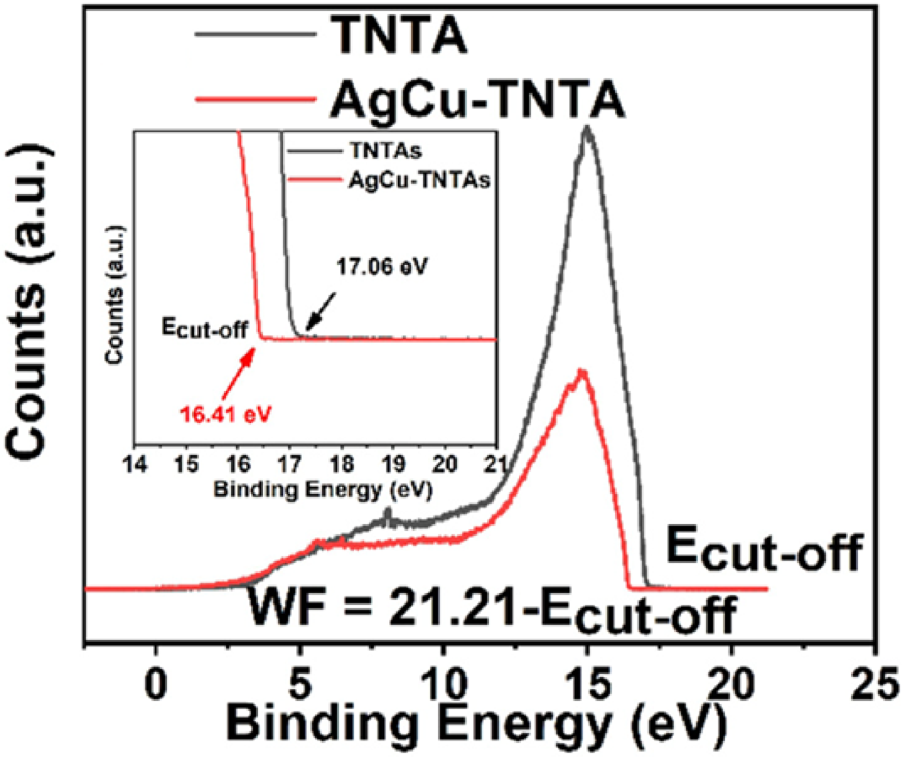

Figure 23. UPS work function spectra of TNTA and AgCu-TNTA. The inset shows the cut-off energy (**$E_{cut\text{-}off}$**) of secondary electrons. The value of work function (WF) was determined using the expression **WF (ϕ) = 21.21 – $E_{cut\text{-}off}$,** where 21.21 eV is the energy of the incident, He I line of He discharge lamp

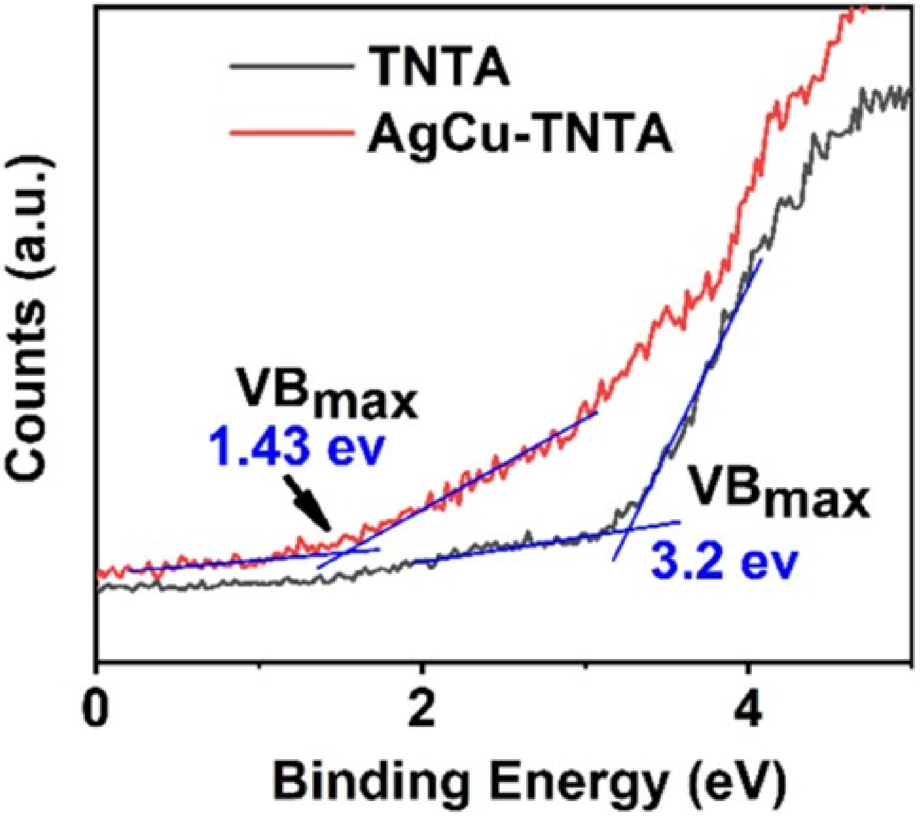

Figure 24. UPS valence band spectra showing the position of the valence band maxima (**VB_{max}**) below the Fermi level

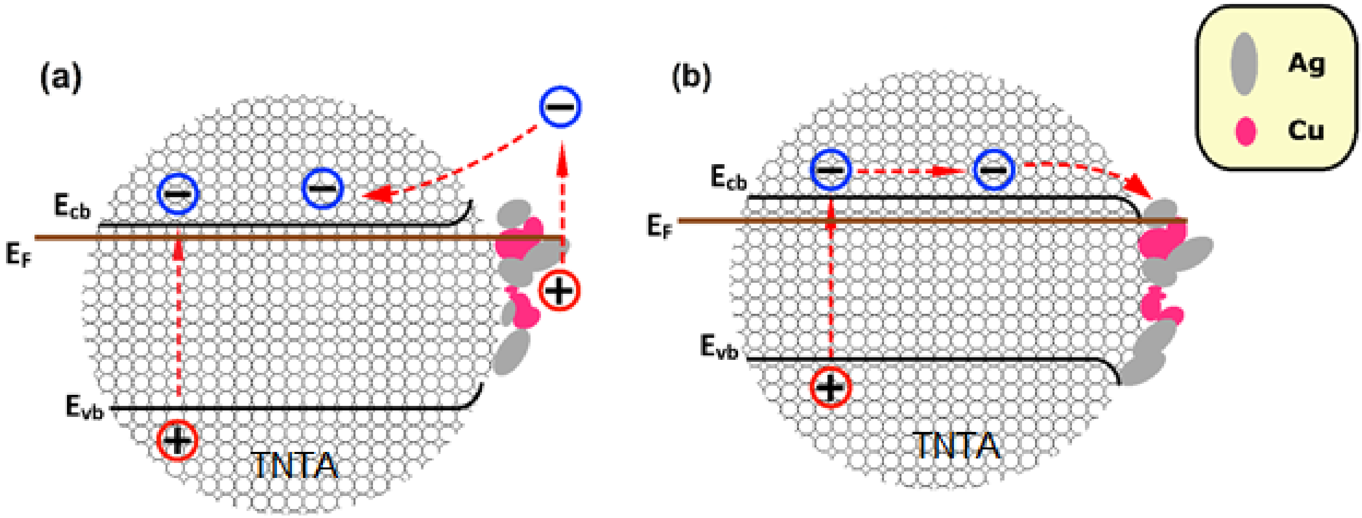

Figure 25. (a) Schematic diagram of the proposed band diagram at the AgCu-TNTA interface showing upward band bending due to the formation of a Schottky barrier and concomitant interfacial depletion region and (b) Schematic

diagram of an accumulation-type heterojunction at the metal/semiconductor interface where metal nanoparticles play the role of an electron sink.

To confirm that the reaction products stem from CO_2 and not from any source of carbon contamination, a series of sanity tests were conducted. The sanity tests performed included conducting the reaction in a reactor filled with nitrogen gas (instead of CO_2), running the reaction in the dark (with and without photocatalyst), conducting the experiment without heating the reactor, illuminating the reactor filled with only water and CO_2 (no photocatalyst), and conducting the reaction using a Titanium foil instead of the photocatalyst. In all these sanity tests, no product could be detected by the gas chromatograph, which provides direct evidence that the simultaneous presence of photocatalyst, water vapor, heat, and light (solar simulator) are essential for driving the chemical reaction. In addition, we performed $^{13}CO_2$ isotope labeling test in which instead of introducing the regular $^{12}CO_2$ gas into the reactor, $^{13}CO_2$ alone was introduced into the reactor while keeping all other reaction conditions identical. The gaseous products of the isotope labeling test were analyzed by gas chromatography-mass spectrometry (GC-MS), and the resulting ion chromatogram is shown in Figure 26. The isotope labeling test confirmed the presence of $^{13}CH_4$ at an *m*/*z* value of 17 and $^{13}C_2H_6$ at an *m*/*z* value of 32.

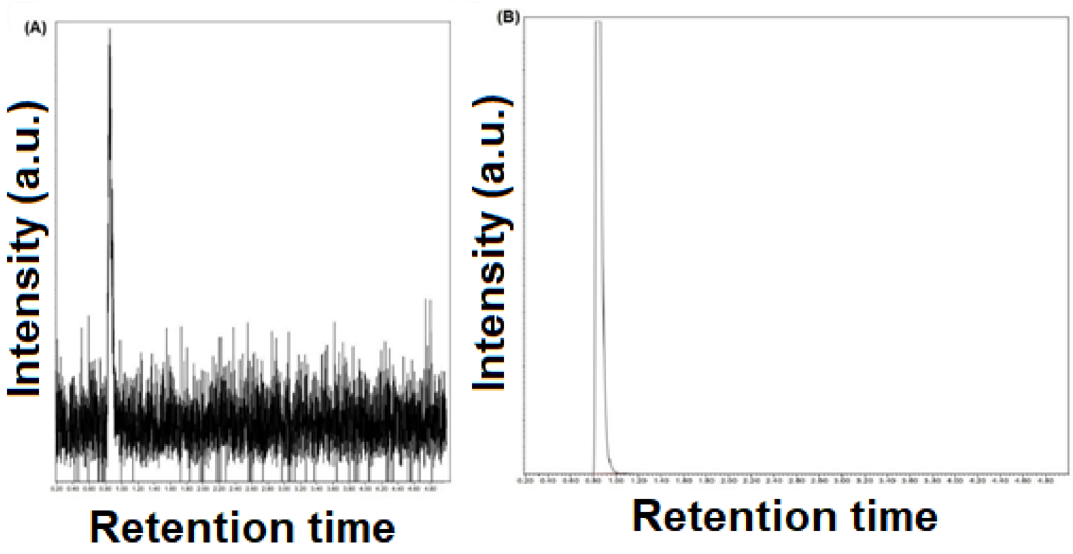

Figure 26. GC-MS ion chromatogram showing the results of ^{13}C isotope-labeled CO_2 photoreduction experiment for the AgCu-TNTA sample (a) The peak at m/z = 17 confirms the presence of $^{13}CH_4$, and (b) The peak m/z = 32 confirms the presence of $^{13}C_2H_6$.

3.4. Conclusion of chapter 3

The next frontier in CO_2 photoreduction research is improving product selectivity. The research focus is shifting from larger yield numbers to higher purity and more valuable products. A gamut of chemicals, including C_1 products (CO, CH_4, and CH_3OH) and heavier C_2 hydrocarbons (C_2H_6, C_2H_5OH), can be produced during the CO_2 photoreduction process. Heavier hydrocarbons are preferred because of their higher energy density and higher economic value. Obtaining heavier hydrocarbons is extremely difficult due to lower yields (recombination and other losses in more numerous electron transfer steps), poorer selectivity (more intermediates and by-products), inter-adsorbate repulsion inhibiting C-C coupling, and less kinetic and thermodynamic preference. Herein we presented a method toward the preferential formation of C_2 products during CO_2 photoreduction using TiO_2 nanotube arrays (TNTA) decorated with large-sized (80-200 nm) photo deposited AgCu nanoparticles (NPs). Large, close-lying plasmonic NPs exhibit an asymmetric surface charge distribution following photoexcitation due to antisymmetric quadrupole resonances and hybrid multipole plasmonic modes with electric fields that vary rapidly in space. AgCu-TNTA exhibited higher absolute product yields (14.5 μmol gr^{-1} hr^{-1} of ethane and 9.38 μmol gr^{-1} hr^{-1} of methane) and higher selectivity (60.7% selectivity toward ethane production) for C_2 product compared to TNTA decorated with monometallic Ag or Cu NPs. We attribute the superior performance to (i) Improved C-C coupling due to lowered dipole repulsion between adsorbed reaction intermediates, (ii) Schottky barrier-mediated long-lived charge separation following excitation and plasmon decay, (iii) Local electric field enhancement at hot spots, and (iv) Enhanced stabilization of methyl radicals by hole-rich AgCu NPs. Until now, the best selectivity for ethane reported in the literature was achieved through expensive cocatalysts such as Pt and Au, with the highest reported selectivity of ~40% using Au NP co-catalysts. In this report, we utilized a relatively cheap cocatalyst consisting of AgCu NPs with an unprecedented selectivity of 60% towards ethane. Our results show that bimetallic co-catalysts made of relatively inexpensive materials can replace the typical expensive cocatalysts used in the literature and even outperform them in selectivity.

4. Au-amorphous TiO_2 heterojunction: Plasmon coupled ultrathin hot carrier photoanode and photocathode for high-performance photoelectrochemical water-splitting

In this chapter, ultrathin, core-shell Au@a-TiO_2 was fabricated using a thermal dewetting method followed by ALD deposition. The fabricated photoelectrodes were characterized thoroughly and their photoelectrocatalytic performance were investigated for photoelectrochemical water-splitting reaction. A novel charge transfer mechanism based on injection of holes to the structure of a-TiO_2 is justified using characterization techniques and presented.

4.1. Background and motivation

Hydrogen produced by photoelectrochemical splitting of water is a clean energy carrier with a zero-carbon footprint directly produced from sunlight through the photoelectrochemical (PEC) water-splitting reaction. Consequently, PEC water-splitting is being actively researched as a promising approach for utilizing freely available solar energy to build out the hydrogen economy and address future energy demand. [104] For splitting of the water to happen, the bonds between hydrogen and oxygen should break. In PEC water-splitting, the energy needed for breaking this bond can be supplied by the photo-generated charge carriers provided by the photoelectrode.[105] Titanium dioxide (TiO_2) is one of the most extensively used semiconductor materials as a photoelectrode in PEC water-splitting. Since TiO_2 is a wide bandgap n-type semiconductor, it can only utilize 5% (ultraviolet) of the solar light spectrum, limiting its efficiency for driving the water-splitting reaction.[106]

In search of an efficient photoelectrode for PEC water-splitting, the fabrication of a heterojunction between TiO_2 and a plasmonic noble metal has been reported to be a versatile approach to push the efficiency of TiO_2 beyond its limits.[107] When the size of noble metal nanoparticles such as Au and Ag are small enough, the light can interact with them through localized surface plasmon resonance (LSPR).[108] The LSPR effect results in the intense interaction of plasmonic nanoparticles with incident electromagnetic waves, especially under visible light excitation. The LSPR can decay through radiative and nonradiative processes. In radiative mode, the plasmons damp through photon emissions, while nonradiative leads to the formation of energetic electron-holes known as hot electron-hole pairs.[109] Since TiO_2 can absorb the light in the ultraviolet (UV) region and LSPR excitation of plasmonic noble metals happens in the visible light region, a carefully devised heterojunction between Au and TiO_2 can potentially be utilized as an efficient photoelectrode in PEC water-splitting with photo-response in the whole solar light spectrum.

The fabrication of a heterojunction between TiO_2 and Au has already been investigated for water-splitting applications. Almost all of these investigations were specifically focused on devising a visible light-responsive photoelectrode that works based on hot electron injection into the conduction band of highly crystalline TiO_2, in which TiO_2 was exploited as an electron-accepting material.[107, 110-113] Recently, amorphous TiO_2 (a-TiO_2) has gained more attention both as a protective layer for a photoelectrode and a charge transport layer. Due to amorphous materials' defective structure, they tend to have energy states between the conduction band and the valance band, acting as a trap or acceptors.[114] Recent studies suggest that under certain conditions, a-TiO_2 can work as a leaky hole transport material as well; the injection of holes into leaky amorphous TiO_2 structure can happen through mid-bandgap energy states exist because of the presence of defects,[115-117] Oxygen vacancies,[118] and dopants such as Carbon, Boron, and Nitrogen in the structure of a-TiO_2.[119]

In this chapter, we devised and fabricated a heterojunction between Au (core) and thin amorphous TiO_2 (a-TiO_2, shell) using core-shell architecture, in which the a-TiO_2 shell in the architecture acts both as the hole transport material and protective layer, which increases the stability of the samples.

Owing to this unique architecture and defective structure of the ultra-thin a-TiO_2 layer, the fabricated samples exhibited remarkable photocurrent density both under standard solar light illumination and visible light excitations, the charge transfer mechanism studies in this report reveals that the fabricated photocathodes work based on the injection of holes from the Au core to the band structure of the a-TiO_2 shell.

4.2. Synthesis of TiO_2 and Au@a-TiO_2 photoelectrodes

Figure 27 exhibits the fabrication process of Au@a-TiO_2 photoelectrodes. All the photoelectrodes were fabricated using fluorine-doped tin oxide (FTO) glass as a substrate. First, the FTO was washed using soap, acetone, and methanol under strong sonication. After that, FTO substrates were loaded into a DC magnetron sputtering system, and a thin layer of Au film with a thickness of 10 nm was deposited on top of the FTO substrates (details of the deposition process can be found on chapter 2). Next, the photoelectrodes were subjected to annealing for 1 hr under an air atmosphere at 550 °C. After this step, spherical-shaped gold islands were formed on top of FTO through spontaneous dewetting of the Au film. Then the photoelectrodes were loaded into an atomic layer deposition system (ALD). A thin (10 nm) layer of amorphous TiO_2 layer was deposited on top of the photoelectrodes to fabricate the Au@a-TiO_2 core-shell films (refer to chapter 2 for details about the ALD deposition). Figure 28 exhibits photographs of the fabricated Au and Au@a-TiO_2 samples. a-TiO_2 photoelectrode was fabricated by directly ALD deposition of amorphous TiO_2 layer on top of a bare FTO electrode.

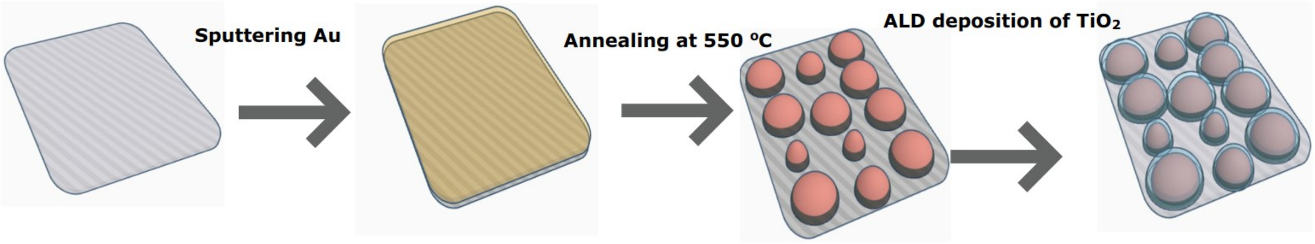

Figure 27. The schematic illustration of the Au@a-TiO$_2$ fabrication process

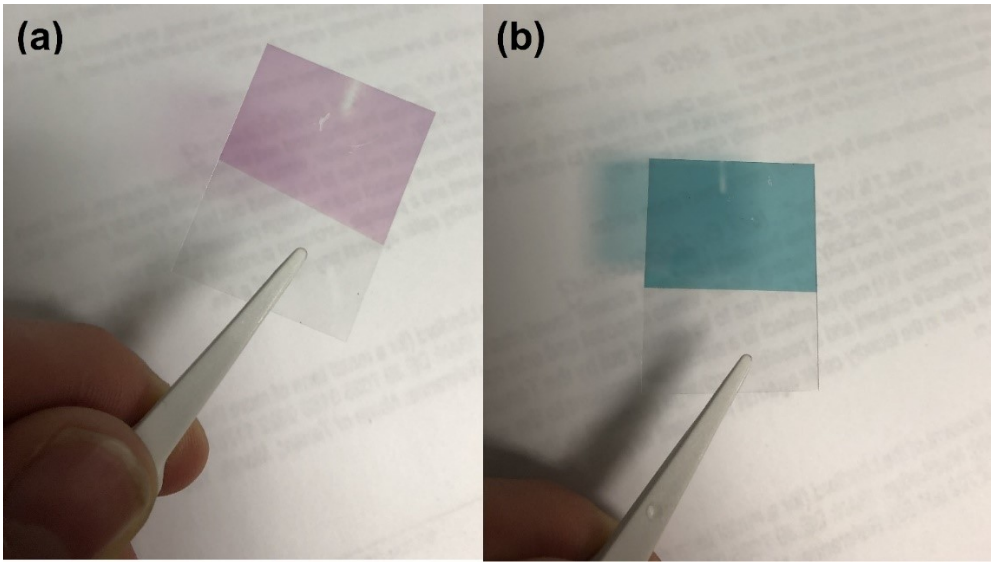

Figure 28. photograph of the Au (a) and (b) Au@a-TiO$_2$ samples.

4.3. Results and Discussions

The morphology of the Au nanoparticles and Au@a-TiO$_2$ were investigated using Helium ion microscopy (Figure 29a,b). Figure 29a provides evidence that annealing at 550 ºC was successful in dewetting the sputtered gold film. The images of annealed Au samples show nearly spherical gold nanoparticles. The clear distinction between the Au (core) and TiO$_2$ (shell) in the core-shell structure of the fabricated photoelectrode is also clearly shown in the Helium ion images of Au@a-TiO$_2$ (Figure 29b). Figure 30 shows the field emission scanning electron microscopy (FESEM) image of the Au and

Au@a-TiO_2 samples. As it can be seen from Figure 30a, after the annealing step, the spherical gold island formed at random places with a size distribution that ranges from 10 nm to 100 nm with an average size of 50 nm (inset of Figure 30a). After the dewetting, the surface of fluorine-doped tin oxide (FTO) was exposed in places where gold islands did not form. Since ALD is a cyclic, conformal, and precise deposition process, after deposition of a-TiO_2 on the gold islands using the ALD technique, it completely covered Au nanoparticles' surface and the exposed surface of FTO in the Au@a-TiO_2 sample (Figure 30b).

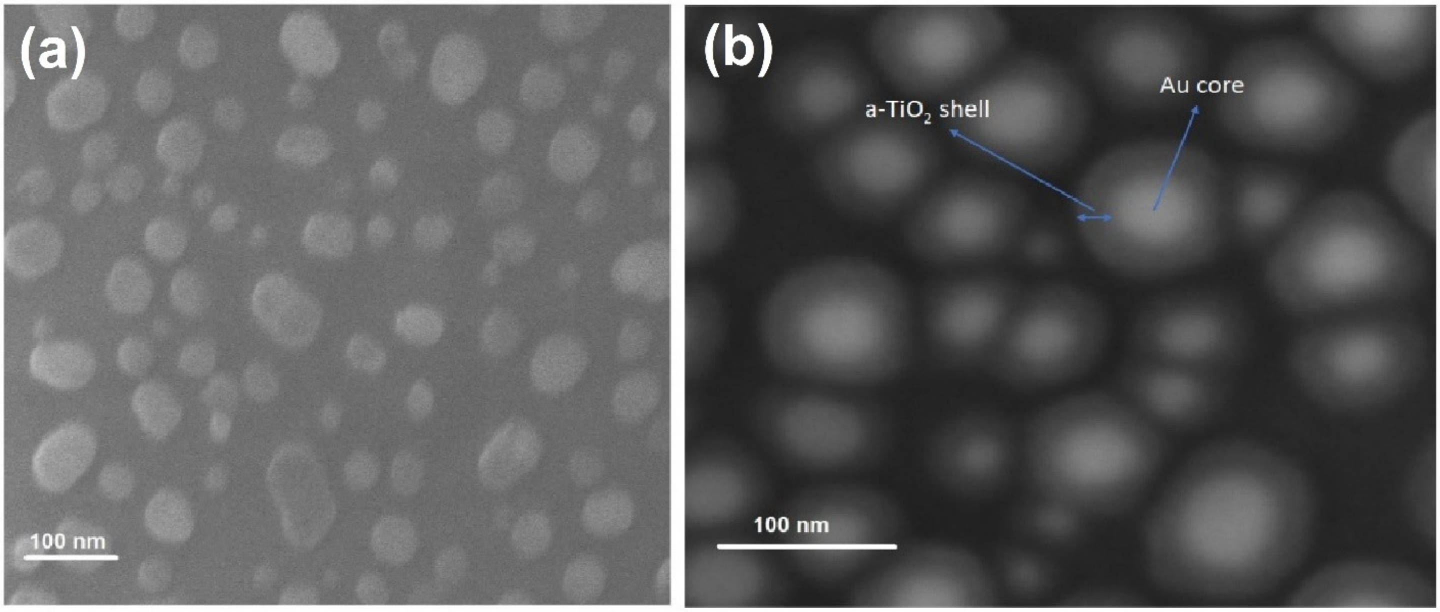

Figure 29. Helium ion images of (a) Au and (b) Au@TiO_2 on FTO substrate.

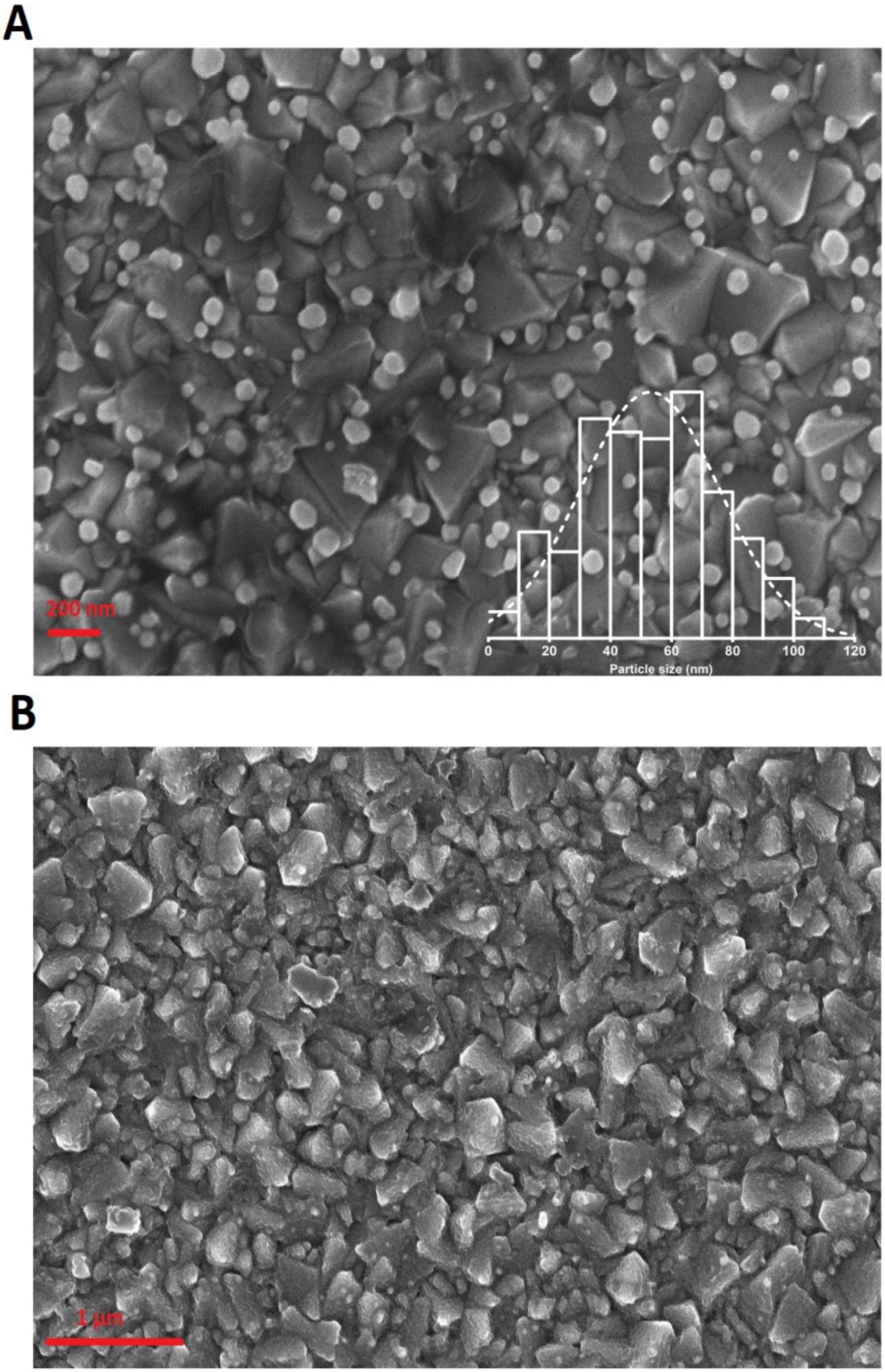

Figure 30. FESEM images of (a) Au nano particles and (b) Au@a-TiO_2.

The fabricated samples' optical properties were investigated using UV-Vis spectroscopy and finite difference time domain (FDTD) simulations. The UV-vis spectra and FDTD simulated absorption cross-section of the Au, a-TiO_2, and Au@a-TiO_2 samples are shown in Figure 31 and Figure 32, respectively. The UV-Vis spectrum of the Au sample (indicated by a solid black line) exhibits a peak at around 560 nm, which is the characteristic LSPR peak of gold nanoparticles, FDTD simulation of bare gold nanoparticles (solid red line in Figure 32) exhibit the LSPR peak at the same wavelength (560 nm). The UV-vis spectrum (solid red line in Figure 31) and simulated absorption cross-section of the Au@a-TiO_2 (solid blue line in Figure 32) sample exhibits a redshift in the plasmon resonance, the LSPR peak of Au shifts from 560 nm to 650 nm after deposition of a-TiO_2 shell which can be attributed to the higher refractive index of a-TiO_2 compared to air. It has been reported that the LSPR peak of gold nanoparticles is extremely sensitive to the refractive index of its surrounding environment. In this case, since the refractive index of TiO_2 is higher than air, a significant redshift to higher wavelengths occurs, the same trend can be seen from the FDTD simulated absorption cross-section of the Au@a-TiO_2 sample where the LSPR peak of the simulated structure was shifted from 560 nm in bare Au to 650 nm in the Au@a-TiO_2 structure.[114, 120] Also, the UV-vis spectra reveal that the absorption of wavelengths shorter than 420 nm for Au@a-TiO_2 increased compared to Au, which shows the contribution of a-TiO_2 in light absorption at the shorter wavelengths. The UV-vis spectra of the amorphous TiO_2 layer (a-TiO_2) exhibits absorption in the UV region with negligible light absorbance in the visible light spectrum. The visible light absorbance of the a-TiO_2 suggests the presence of defects and mid bandgap energy states in its structure.[121] The electric field enhancement at the plasmonic metal/semiconductor interface plays an essential role in generating hot carriers.[122] Figure 33 exhibits the FDTD simulated cross-section of electric field distribution for a single Au@a-TiO_2 particle on (at 650 nm) and of resonance (at 500 nm), Figure 33a demonstrates the generation of a strong electric field at the interface between the gold nanoparticles and the a-TiO_2 shell at 650 nm such strong electric field enhancement was not observed of resonance.

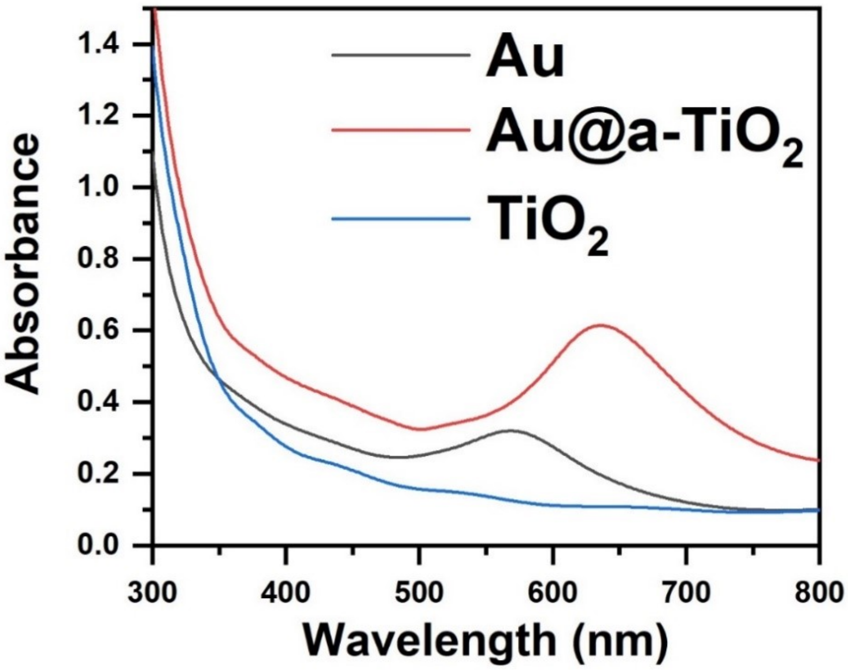

Figure 31. UV-Vis spectrum of Au, a-TiO_2, and Au@a-TiO_2 photoelectrodes.

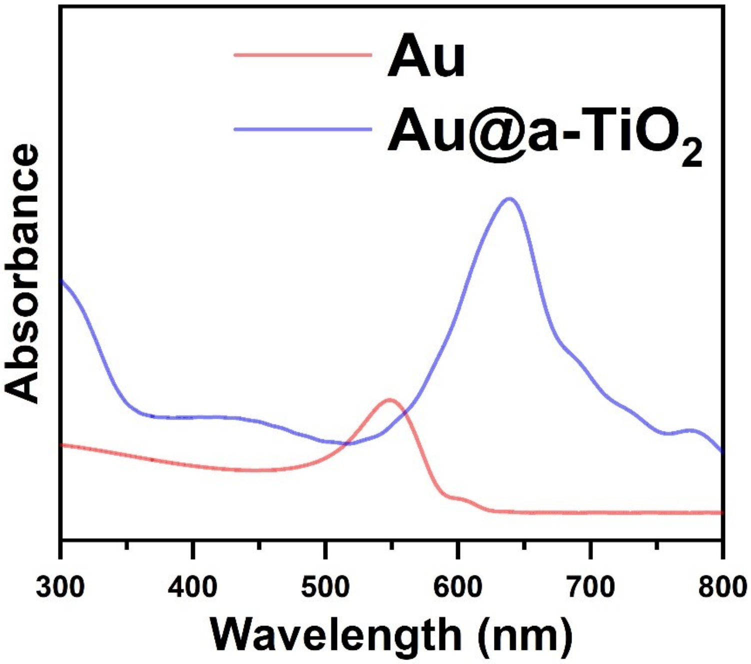

Figure 32. FDTD-simulated absorption cross-section of Au and Au@a-TiO_2 structures.

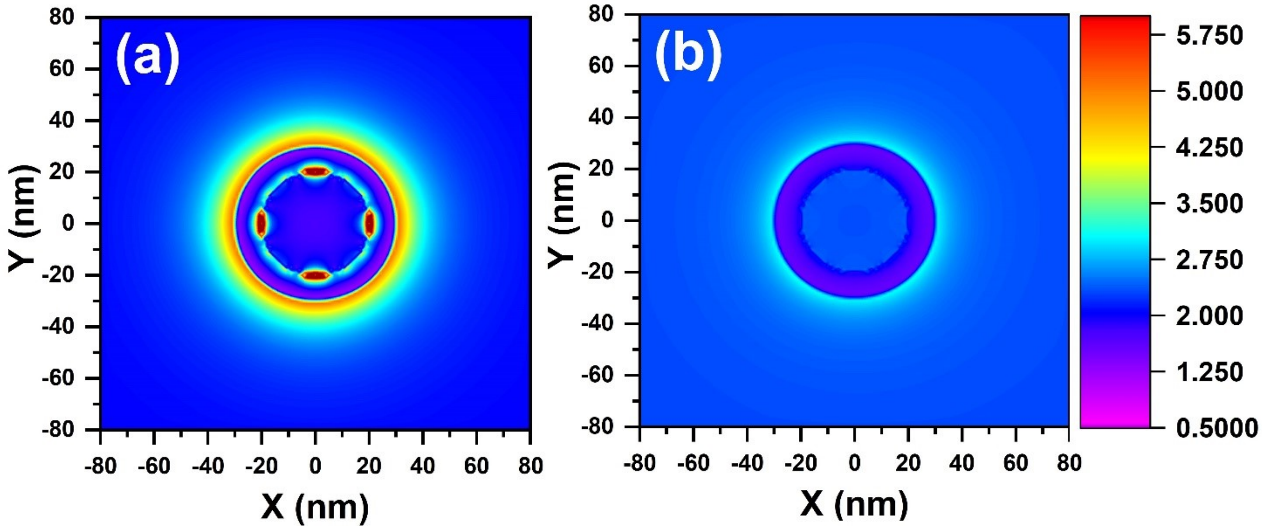

Figure 33. Top view FDTD-simulated electric field profile of Au@a-TiO_2 on (at 650 nm) and of resonance (at 500 nm).

The X-ray diffraction (Figure 34) of the Au and Au@a-TiO_2 reveals the presence of the Au (111) at 2θ=39, no peaks related to Anatase or Rutile TiO_2 can be detected, which proves that the ALD deposited TiO_2 is primarily amorphous. An ALD deposited TiO_2 on a glass substrate sample was annealed at 450 ^{0}C for 2 hours to confirm this. The XRD pattern of this sample (blue line in Figure 34) proves that the annealing can change the structure of TiO_2 from amorphous to crystalline (Anatase). One of the most powerful tools for investigating the ordered/disordered TiO_2 structures is Raman spectroscopy.[123] The Raman spectra of the annealed crystalline Anatase TiO_2 and Au@a-TiO_2 samples are shown in Figure 35. The Anatase TiO_2 sample exhibited an intense peak around 145 $cm^{-1,}$ which belongs to E_g mode with three less intense peaks at 395 cm^{-1}, 516 $cm^{-1,}$ and 640 cm^{-1} related to B_{1g}, A_{2g}, and E_g modes, respectively. Compared to the annealed sample, the Au@a-TiO_2 exhibited less intense peaks at the same wavenumbers, which evidences that the structure of a- TiO_2 is half crystalline-half amorphous, and disordered.[124]

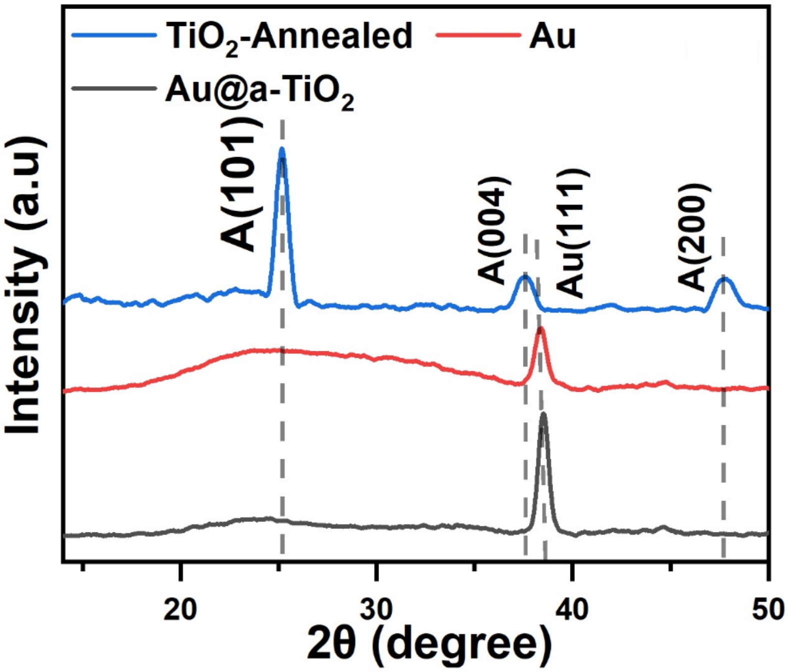

Figure 34. The XRD spectra of Au, annealed TiO$_2$, and Au@a-TiO$_2$ on FTO.

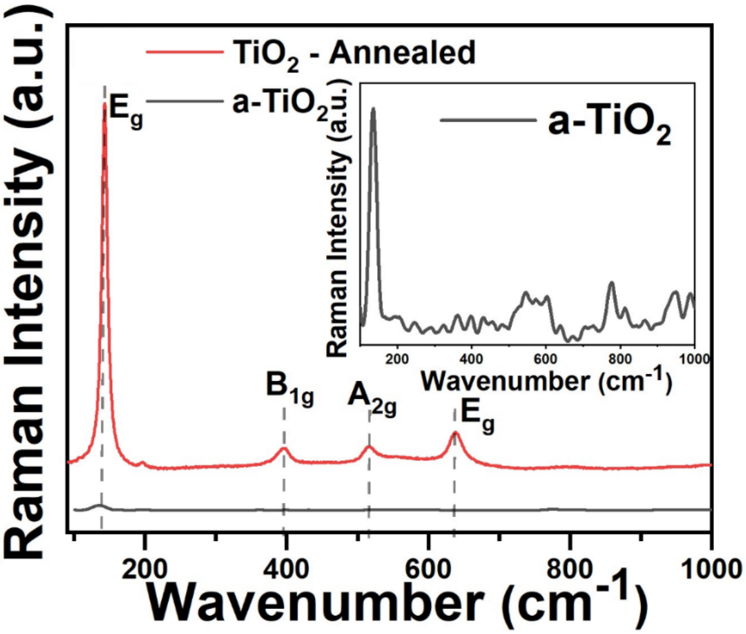

Figure 35. the Raman spectra of annealed TiO$_2$ and Au@a-TiO$_2$ on FTO.

The chemical composition and corresponding binding energies of the Au@a-TiO$_2$ sample were investigated by X-ray photoelectron spectroscopy (XPS). The results of the XPS are shown in Figure 36. XPS elemental survey scan confirms the presence of Ti2p, Ti2s, O1s, Au 4f, and Au 4d (Figure 36a), which evidences all the common main elements of Au and TiO$_2$. Deconvoluted peaks of the high-resolution XPS scan in the O1s region exhibits three peaks centered at 530.2 eV,531.1 eV, and 532.4 eV. These peaks correspond to Ti-O, Oxygen vacancies (V_O), and surface chemisorbed Oxygen (C_O).[125-127] Similarly, the decomposition of the peaks at the Ti2p region exhibits two major peaks centered around 459 eV and 465 eV, which can be attributed to $Ti2p_{3/2}$ and $Ti2p_{1/2}$ of $Ti4^+$ in TiO_2 crystal structure, respectively.[128, 129] Also, the presence of gold in the Au@a-TiO_2 sample was confirmed using two deconvoluted peaks at 84 eV and 87.6 eV, which can be assigned to $Au4f_{7/2}$ and $Au4f_{5/2,}$ respectively.[130] Figure 36e exhibits the XPS depth profile of elements of interests (Ti, Au, and Sn) of the Au@a-TiO_2 photoelectrode to track the presence of a-TiO_2, Au, and SnO_2 respectively, for depth profile scan, the $Ti2p_{3/2}$ has been used to track the abundance of a-TiO_2, $Au4f_{5/2}$ has been used to track the abundance of Au and Sn_{3d} has been used to track the FTO. The core@shell architecture of the Au@a-TiO_2 heterojunction is evidenced by this profile scan in which the depth profile exhibits that the outer surface is completely covered with ALD deposited amorphous TiO_2. As the sputtering continues, the abundance of the Au increases, the depth profile also indicates the ALD deposition of amorphous TiO_2 layer was successful in covering the area of the FTO surface, which got exposed after annealing (dewetting) of the sputtered Au film as Ti could be found even near the surface of FTO (shown by the abundance of the Sn in the XPS depth profile). With core-shell architecture, the Au nanoparticles are not in direct contact with the electrolyte. In this case, the Au core solely acts as an optical antenna and does not act as an active phase for water-splitting reaction.[112] As a result, the amorphous ALD deposited TiO_2 plays the dual role of a charge carrier acceptor and a protective layer for increasing the charge carrier separation benefiting from the core-shell architecture.[121]

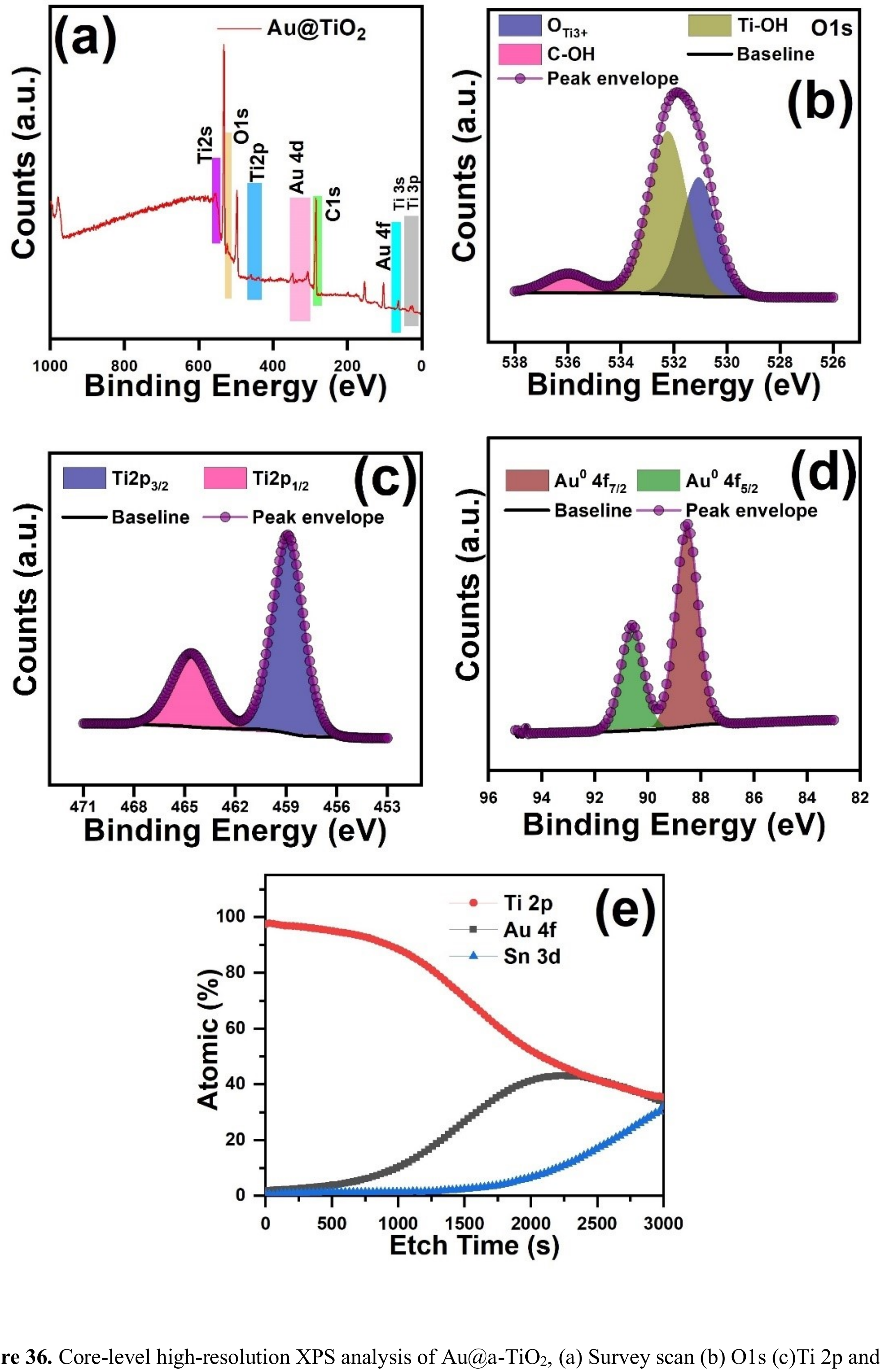

Figure 36. Core-level high-resolution XPS analysis of Au@a-TiO$_2$, (a) Survey scan (b) O1s (c)Ti 2p and (d) Au 4f regions. (e) The XPS depth profile of Au@a-TiO$_2$ by Argon etching.

Based on the UV-Vis spectrum of Au@a-TiO_2, this photoelectrode exhibits appreciable light absorption in the visible light region (>420 nm). As a result, the photocurrent response of Au@a-TiO_2 in comparison with the a-TiO_2 layer was investigated using linear sweep voltammetry (LSV) mode under excitation of 1 sun and visible light (under 1sun with a UV cut-off filter (>420 nm)). Figure 37 exhibits the LSV measurements for Au@a-TiO_2 and a-TiO_2 samples. The photocurrent generated in milliampere per square centimeters was almost zero under dark (no illumination) condition for both samples. Interestingly, under both 1 sun and 1 sun with UV filter illumination, the Au@a-TiO_2 photoelectrode exhibited superior photo response in all applied voltages compared to a-TiO_2 photoelectrode.

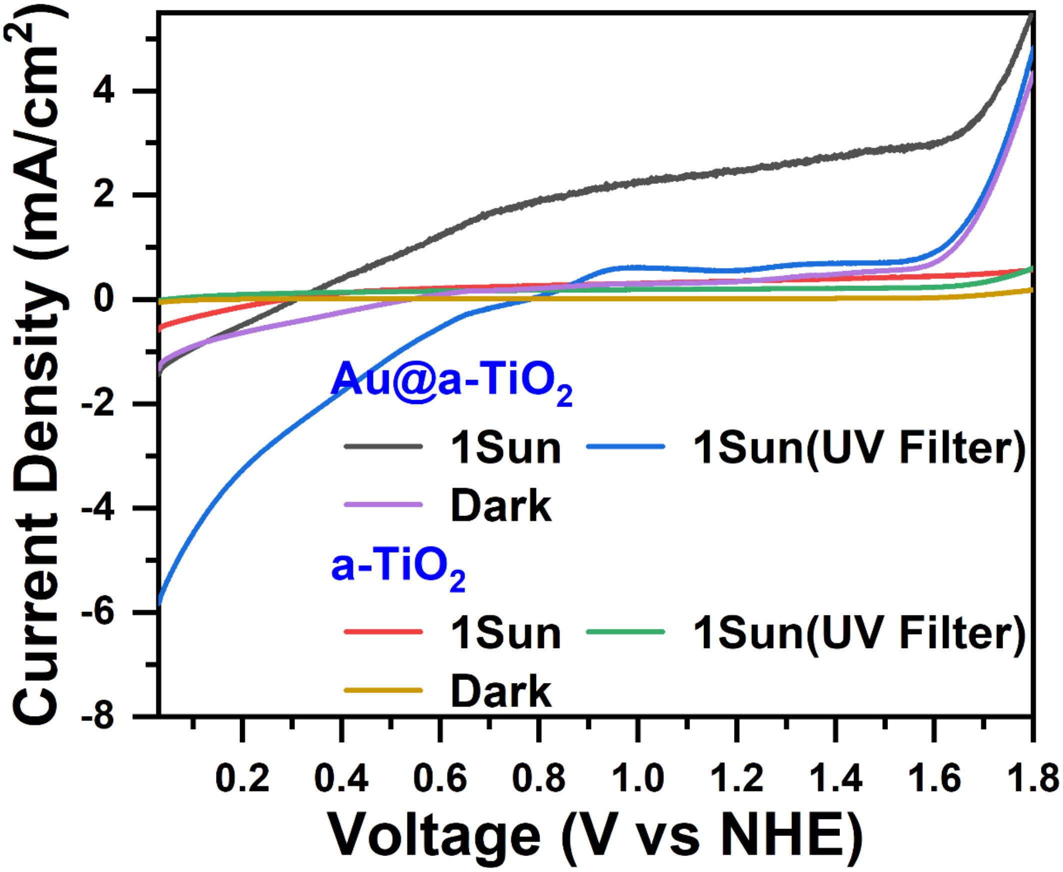

Figure 37. The linear sweep voltammetry (LSV) curves of Au-a-TiO_2 and a-TiO_2 using the solar simulator and solar simulator with UV cut-off illumination under applied potential vs. NHE reference electrode in a 1M KOH electrolyte.

The stability of the photoelectrode is an essential factor for PEC water-splitting applications. To this end, the photocurrent measurement as a function of time (*I-t* curve) can be used as a figure of merit for a photoelectrode's stability.[111] The *I-t* curves of the Au@a-TiO_2 and a-TiO_2 photoelectrodes at an applied bias of +0.6 V versus the Ag/AgCl reference electrode are shown in Figure 38, the superior photoresponse of Au@a-TiO_2 sample compared to a-TiO_2 sample under both 1 sun and 1 sun with UV cut-off illumination is evident in the *I-t* curves.

It is also worthy of mentioning that both of the samples exhibited stable photo response during 3-minute irradiation. Under 1 Sun illumination, Au@a-TiO_2 revealed a remarkable photoresponse of 2.5 mA Cm^{-2} while photoresponse of a-TiO_2 was only 0.3 mA Cm^{-2}. Under visible light illumination, the Au@a-TiO_2 and a-TiO_2 exhibited photocurrent of 0.5 mA Cm^{-2} and 0.1 mA $Cm^{-2,}$ respectively. Based on these results, the photoresponse of Au@a-TiO_2 is almost 8.3 and 5 times higher than the a-TiO_2 photoelectrode under the 1 Sun and 1 Sun with UV cut-off illumination.

These results also indicate that even though the Au@a-TiO_2 sample considerably absorbs the light in the visible region, excitation under UV light contributes a lot to generating electron-hole pairs in this sample. The remarkable photo-response of the Au@a-TiO_2 photoelectrode encouraged us to conduct the hydrogen evolution reaction using H-Cell (details of the experiments are explained in chapter 2), the results are shown in Figure 39. Under 1 sun illumination, the Au@a-TiO_2 exhibits a remarkable H_2 production rate of 22.8 µmol.h^{-1} corresponding to Faradaic efficiency of 78.9 % while the H_2 production rate of a-TiO_2 photoelectrode was only 2.6 µmol.h^{-1} with Faradaic efficiency of 65.5%.

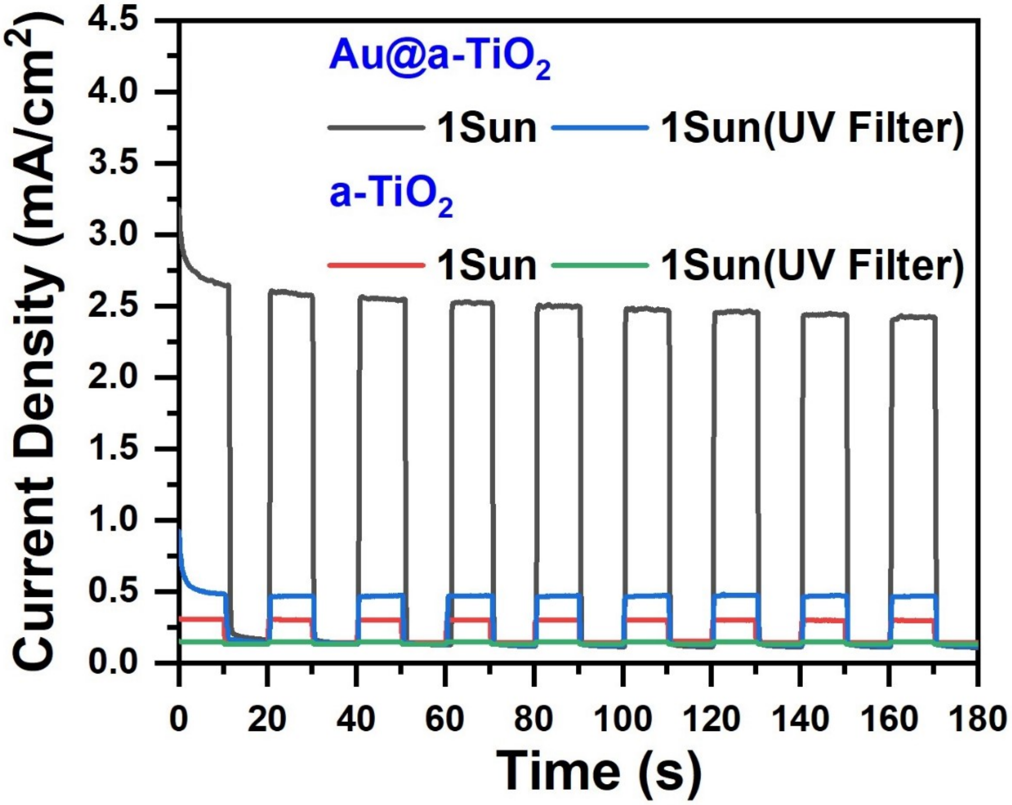

Figure 38. Photoelectrochemical measured it curves of Au@a-TiO$_2$ and a-TiO$_2$ using the solar simulator and solar simulator with UV cut-off illumination under +0.6 V applied potential vs. Ag/AgCl reference electrode in a 1M KOH electrolyte.

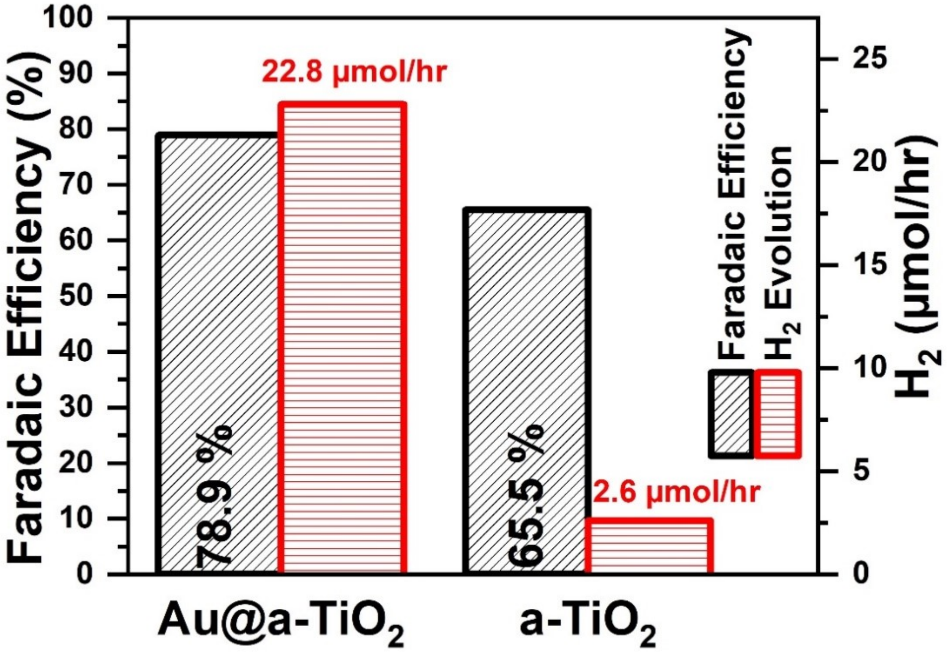

Figure 39. Corresponding H$_2$ evolution and Faradaic efficiency of Au@a-TiO$_2$ under solar simulator illumination.

Investigation of the visible light photocurrent generation of Au@a-TiO_2 sample has been done using a set of LEDs with wavelengths centered at 460 nm, 520 nm, 620 nm, 640 nm, and 730 nm with 10 nm bandwidth. The *I-t* curves using this set of LEDs are shown in Figure 40. From these results, the photocurrent was anodic under the excitation of all of these LEDs. Au@a-TiO_2 showed the highest photoresponse under the 460 nm excitation. As the LED's wavelength increased further to the visible light region (excitation under less energy), this sample's photoresponse gradually decreased.

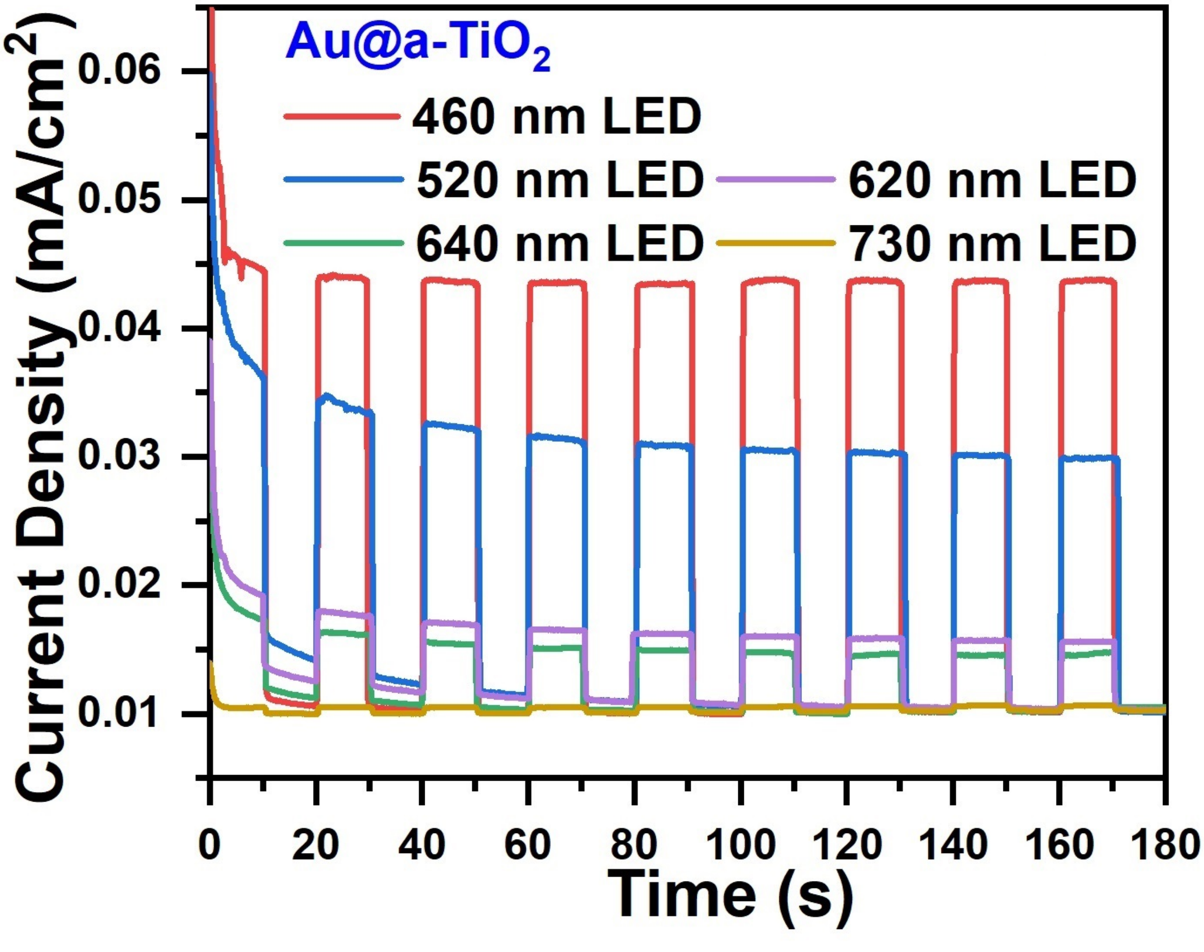

Figure 40. Photoelectrochemical measured I-t curves of Au@a-TiO_2 using visible LEDs illumination under +0.6 V applied potential vs. Ag/AgCl reference electrode in a 1M KOH electrolyte.

To investigate the charge transfer mechanism in Au@a-TiO_2 photoanodes, a series of scavenger tests were conducted. Scavengers are the materials that can react with electrons (electron scavengers) or holes (hole scavengers) and prevent the recombination of photo-generated electron-hole pairs at the photoelectrode/electrolyte interface.[131] To this end, methanol, a known hole scavenger, was used in the electrolyte (see experimental procedures section in chapter 2). Figure 41 exhibits the *I-t* curves of Au@a-TiO_2 photoanode using methanol as the hole scavenger. An apparent photocurrent enhancement effect has been seen when methanol was used in the electrolyte as a hole scavenger under the excitation of 1 Sun and visible light (using the UV cut-off filter). This further proves that the fabricated Au@a-TiO_2 photoelectrode providing holes to the electrolyte during the water-splitting reaction.

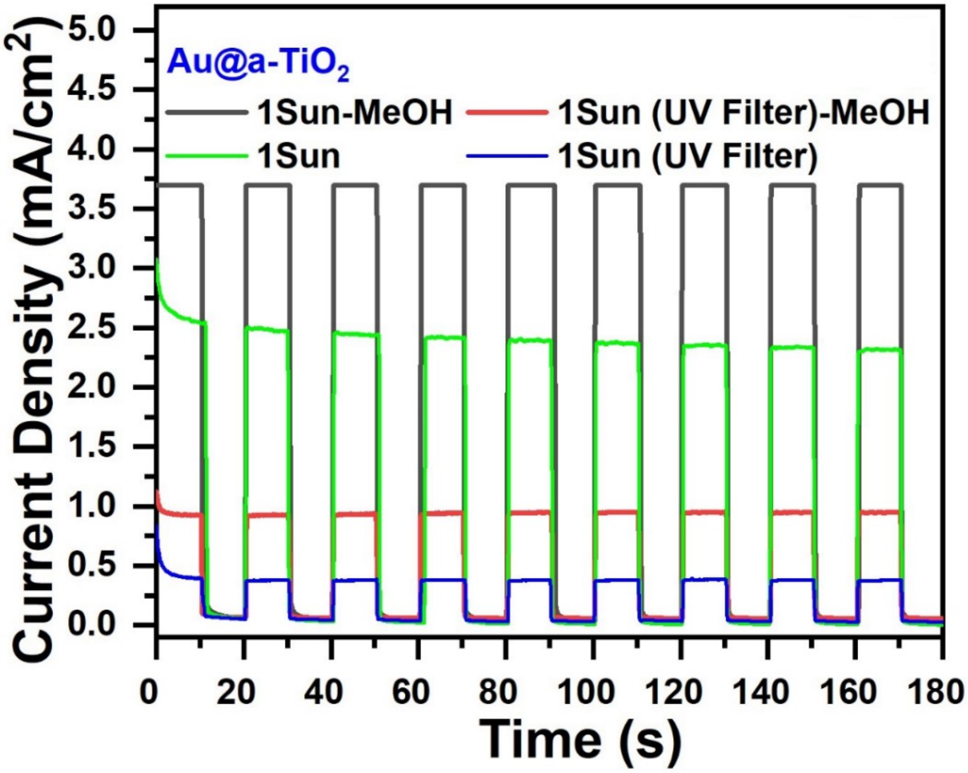

Figure 41. Comparison between the photoelectrochemical measured I-t curves of Au@a-TiO_2 using the solar simulator and solar simulator with UV cut-off illumination under +0.6 V applied potential vs. Ag/AgCl reference electrode in a 1M KOH electrolyte with and without hole scavengers (MeOH).

Another figure of merit for evaluation of plasmon-induced PEC water-splitting is the photocurrent measurement as a function of excitation wavelength, also known as action spectrum.[110, 132] Figure 42 exhibits the corresponding visible light action spectrum of the Au@a-TiO$_2$ photoanode using the *I-t* curves (the absorption spectrum of Au@a-TiO$_2$ in the visible light region is also shown by a dotted blue line to guide the eyes). Previous reports claim that the action spectrum of a plasmonic photoanode should usually follow the absorption spectrum and shows a peak around the photoanode's plasmonic peak, which is an indication of hot electron injection.[132] The action spectra of the Au@a-TiO$_2$ photoanode did not follow the LSPR peak and showed a gradual decrease as the wavelength increased. It has been reported that when the photoresponse of the photoelectrode does not follow the LSPR, the measured photoresponse can be attributed to the injection of holes from the plasmonic material to its surroundings which in this case is an a-TiO$_2$ shell.[110, 133] To investigate this, we utilized one of the most robust techniques to elucidate the charge transfer mechanism in plasmonic materials: the Kelvin probe force microscope (KPFM), with the capabilities to measure the surface potential of a sample in nanometer resolution.[134, 135] To analyze the viability of the injection of holes to the outer a-TiO$_2$ shell, the surface potential of Au@a-TiO$_2$ photoelectrode was measured using KPFM under two illumination sources of 520 nm and 635 nm. The results are shown in Figure 43. Since the a-TiO$_2$ Shell is the outer layer in Au@a-TiO$_2$ sample, the KPFM result represents the shell's (a-TiO$_2$'s) potential. According to Figure 43, when Au@a-TiO$_2$ is under both 635 nm and 520 nm excitations, the surface potential is shifted to positive side compared to the dark condition. Interestingly, the 520 nm excitation resulted in the most positive surface potential compared to 635 nm and dark condition, which is in good agreement with the action spectrum graph. The photocurrent generation was higher for excitation under wavelengths with higher energy.

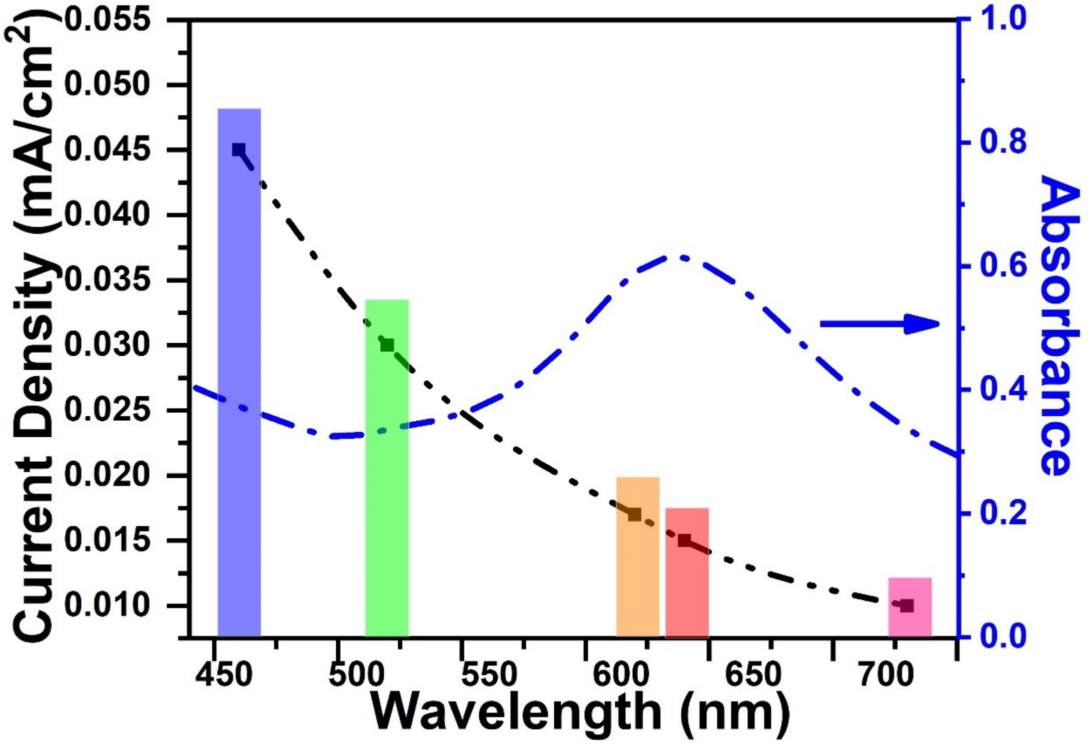

Figure 42. Corresponding action spectrum of Au@a-TiO_2 under LEDs illumination.

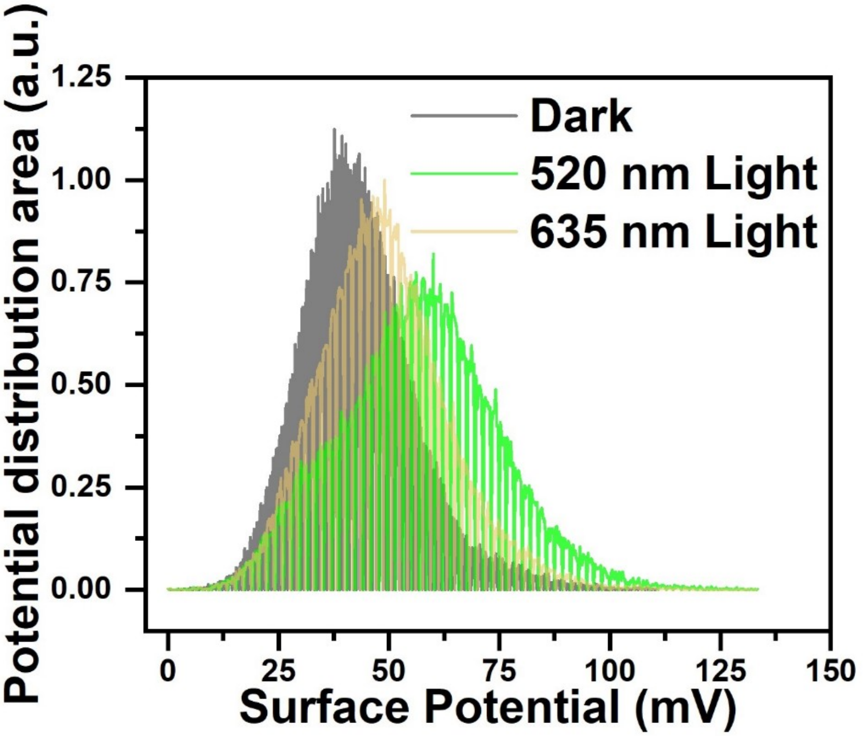

Figure 43. The surface potential of the Au@a-TiO_2 photoelectrode under 520 nm and 635 nm excitations.

Since the work function (the energy needed to extract an electron to a point in vacuum) of the metals are usually lower than the semiconductors (Figure 44), formation of a heterojunction between the metal and the semiconductor, creates a depletion region at the interface of the metal/semiconductor. The depletion region acts as a potential barrier and bends the band at the metal/semiconductor interface.[13, 14] The ultraviolet photoelectron spectra (UPS) of the Au, a-TiO_2, and Au@a-TiO_2 are shown in Figure 44, the work function (ϕ_s) of Au, a-TiO_2, and Au@a-TiO_2 photoelectrodes were calculated to be 4.61 eV, 3.5 eV, and 3.81 eV using $\phi_s = h\nu - E_{SE}$ formula in which $h\nu$ is the energy of the photons used to investigate the band structure (21.21 eV) and E_{SE} is the secondary electron cut-off energy [13], the measured work functions are in good agreement with the band diagram of a plasmonic noble metal and TiO_2 heterojunction which after the formation of the heterojunction and equilibrium in Au@a-TiO_2 the work function settled on 3.81 eV (a value between 3.5 eV and 4.61 eV). The valence band spectrum (Figure 45) shows that the valence band maximum of the a-TiO_2 and Au@a-TiO_2 is located at 3.5 eV and 3.27 eV, respectively. The decrease in the valence band maximum for the Au@a-TiO_2 photoelectrode compared to a-TiO_2 suggests forming a Schottky junction and an upward band bending at the Au/a-TiO_2 interface.[13] Further proof for the formation of the Schottky junction between the Au nanoparticles and a-TiO_2 comes from the Mott-Schottky (MS) plots of a-TiO_2 and Au@ a-TiO_2 (Figure 46). The MS plot for a-TiO_2 exhibits a typical steep positive slope of an n-type semiconductor. The carrier concentration for a-TiO_2 was estimated to be 10^{20}- 10^{21} cm^{-3} which is relatively high. This can indicate the presence of oxygen vacancies in a-TiO_2. Au's presence caused an increase in the slope of the MS plot of Au@a-TiO_2, which corresponds to lower carrier concentration and formation of a depletion region in the a-TiO_2 side with an estimated 3-10 nm length.

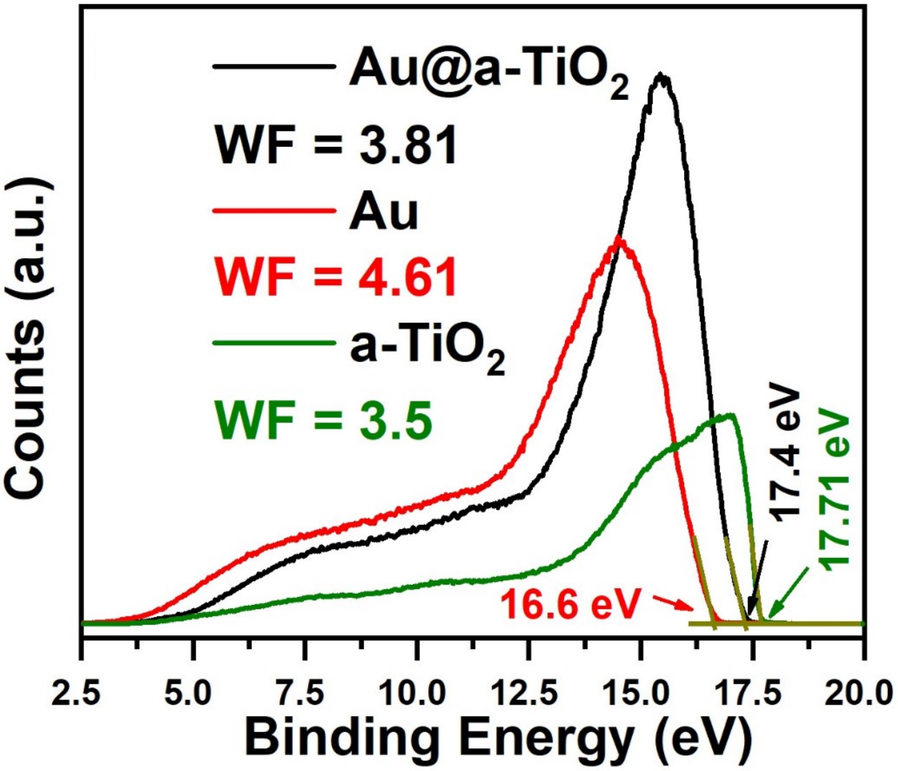

Figure 44. UPS work function of Au, a-TiO$_2$, and Au@a-TiO$_2$ photoelectrodes.

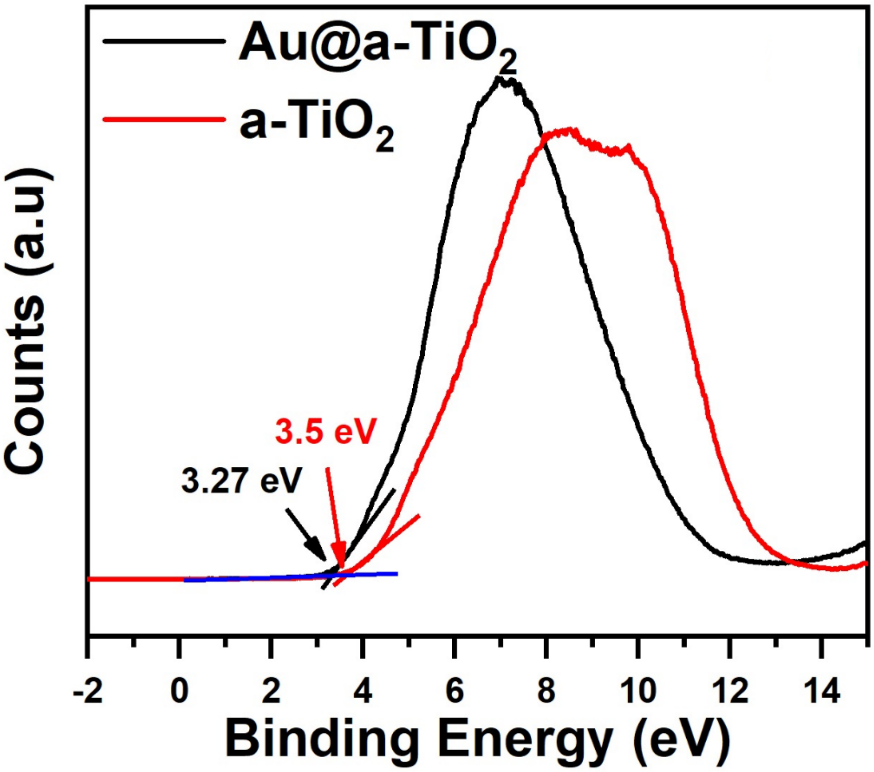

Figure 45. Valance band spectra of Au@a-TiO$_2$ and a-TiO$_2$ photoelectrodes.

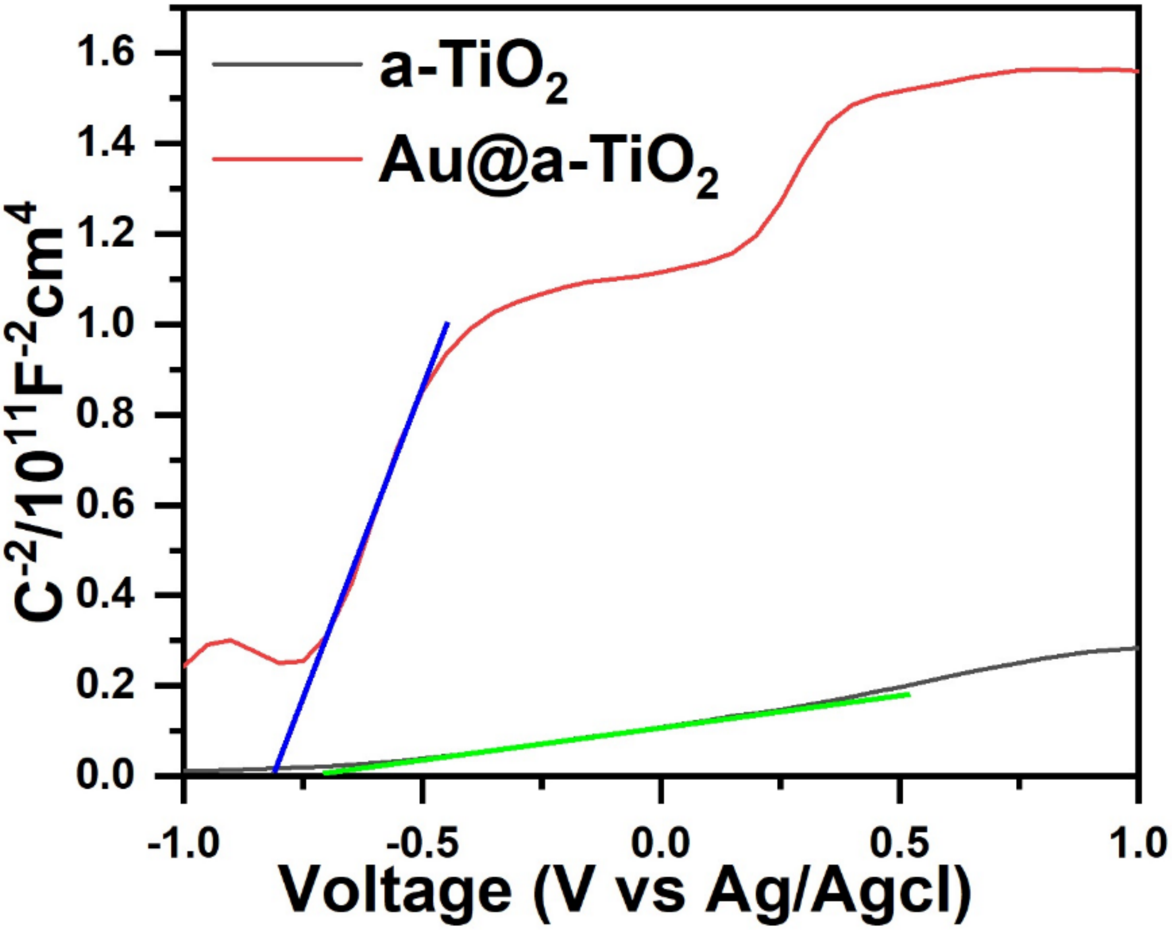

Figure 46. Mott-Schottky plots of Au@a-TiO_2 and a-TiO_2 photoelectrodes.

So far, the *I-t* curves, scavenger tests, and KPFM suggest that under visible light irradiation, Au nanoparticles can inject holes to the a-TiO_2 shell, probably through mid-gap defects, the presence of oxygen deficiencies were already suggested by XPs and MS analysis. To further analyze the defected structure of the a-TiO_2 shell in Au@a-TiO_2, the UV-Vis spectra of the Au@a-TiO_2 from ultraviolet to near-infrared (NIR) region were recorded before, and after 1 hour of visible light illumination (Figure 47), the illumination with visible light excites the LSPR of Au nanoparticles.

As suggested by the results so far, the concentration of holes in the outer a-TiO_2 should significantly increase, since free carriers exhibit enhanced absorption in the NIR region [135], it is expected that the visible light excitation would increase the absorbance of Au@a-TiO_2 in NIR, which is clearly shown in Figure 47. The inset of Figure 47 exhibits the difference between the LSPR peak-normalized UV-vis spectra of Au@a-TiO_2 before and after visible light illumination. Interestingly the normalized difference spectra show a dip around 1750 nm which is pertinent to the absorbance of Ti^{3+} defect states [136], the absence of this dip in the UV-vis spectra of Au@a-TiO_2 can be attributed to the fact that when Au is getting excited with the visible light, the holes from Au gets injected to the a-TiO_2 shell and heal the Ti^{3+} defects so this dip also disappears in the normal UV-vis spectrum.

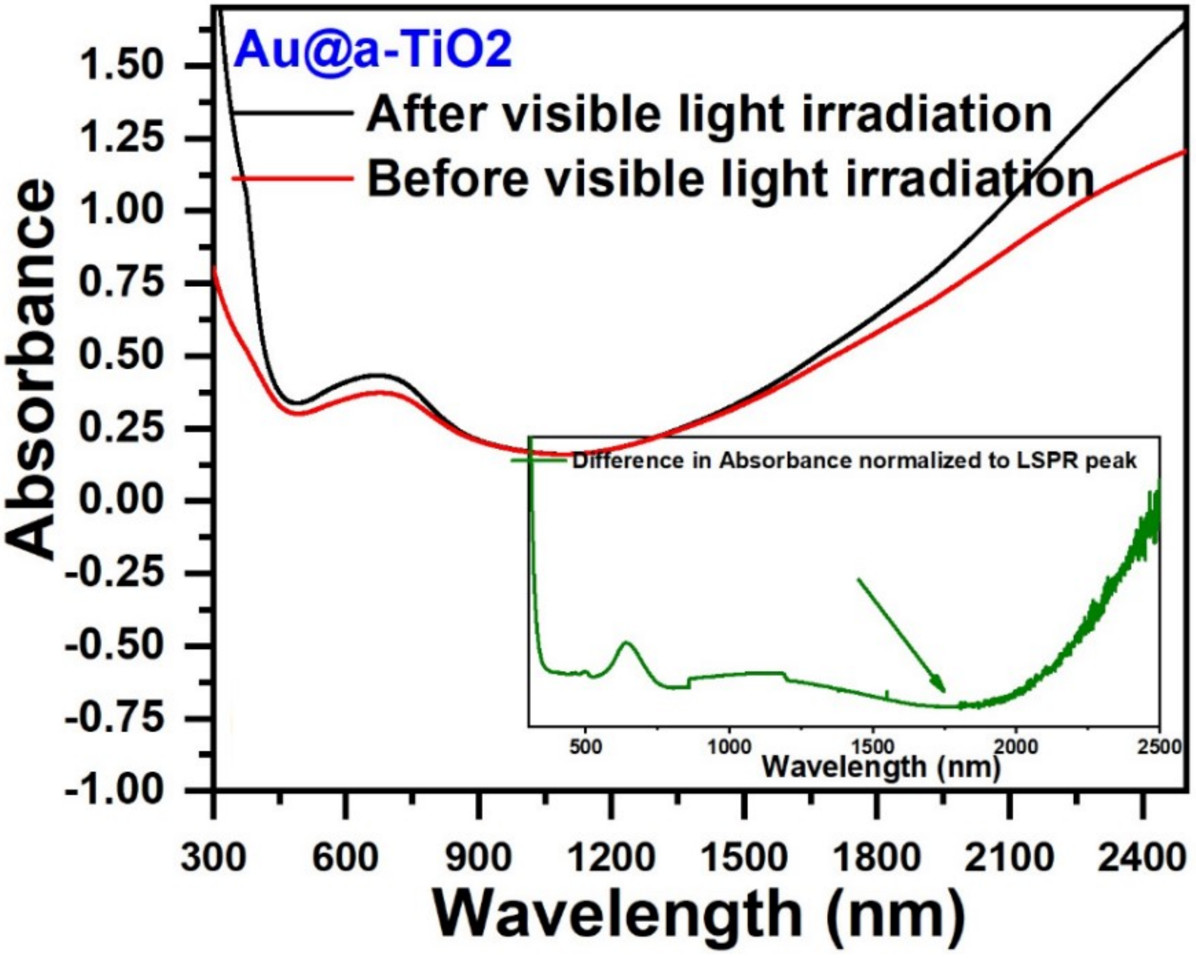

Figure 47. Long-range absorption spectra of the Au@a-TiO_2 before and after visible light irradiation (the NIR absorption corresponds to absorption related to the free charge carriers), the inset exhibits the difference between LSPR peak normalized absorption spectra of Au@a-TiO_2, before and after visible light irradiation.

When the size of the plasmonic nanoparticle is small enough (< 100 nm) in an LSPR excited plasmonic metal /semiconductor heterojunction, there are two possible ways that the charge can transfer between the excited plasmon and the semiconductor, the first way is the plasmon resonance energy transfer (PRET), and the second one is hot-carrier injection.[110, 137, 138] In PRET, the plasmon energy transfers to the nearby semiconductor and makes electron-hole pairs inside the semiconductor's band structure. The main prerequisite for the PRET is the spectral overlap between the absorption band of the semiconductor.[139] Based on the UV-vis spectra, such overlap does not exist in the Au@a-TiO_2 sample; the PRET mechanism is not valid in the Au@a-TiO_2 case, narrowing the possible mechanism of charge transfer to hot-carrier injection mechanism. The hot-carrier injection mechanism's precondition is the direct contact between the metal and the semiconductor, which is valid for the fabricated Au@a-TiO_2 sample.[139]

To provide evidence that a-TiO_2 is an integral entity in Au@a-TiO_2 photoelectrode, two supplementary experiments were conducted. In the first measurement, the a-TiO_2 shell was replaced with Al_2O_3 (Au@Al_2O_3). Figure 48 exhibits *I-t* curves of the Au@Al_2O_3 under 1 sun and 1 sun with UV filter illumination. It is evident that coating the surface with an insulator dramatically decreased the photocurrent. In the next experiment, the Au@a-TiO_2 was annealed to reach crystallinity. This sample was named Au@TiO_2. *I-t* curves of this sample for 1 sun and 1 sun with UV filter illumination are shown in Figure 49. The Au@TiO_2 exhibited 1.75 mA Cm^{-2} and 0.25 mA $Cm^{-2,}$ which is almost half of the photocurrent values obtained by Au@a-TiO_2. These experiments verify that the a-TiO_2 is an essential component in the Au@a-TiO_2. Its amorphous nature helps the electron-hole separation in Au@a-TiO_2 photoelectrode and dramatically enhances the photo response of this electrode.

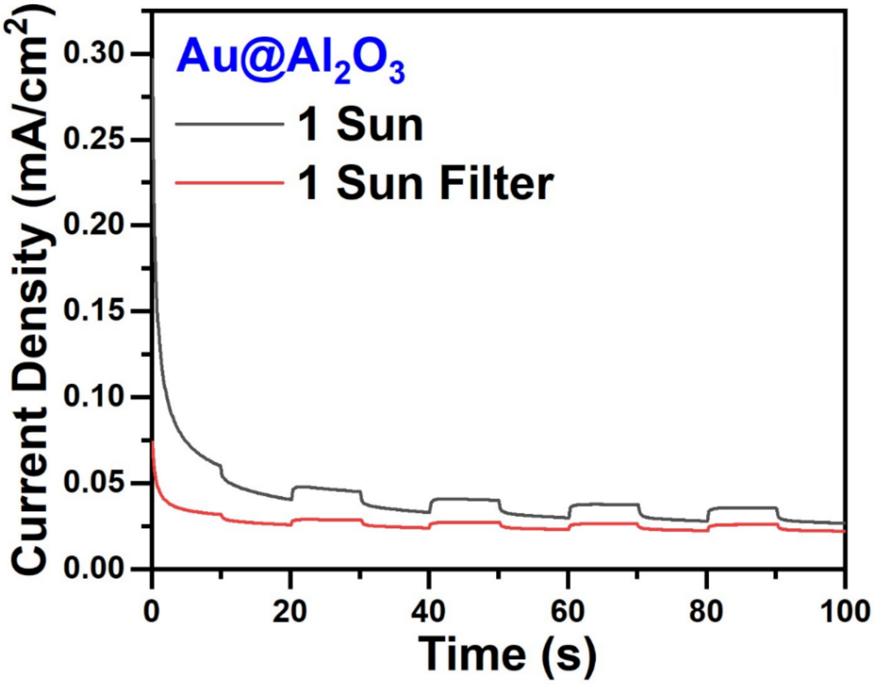

Figure 48. Photoelectrochemical measured I-t curves of Au@ Al_2O_3 photoelectrode using the solar simulator and solar simulator with UV cut-off illumination under +0.6 V applied potential vs. Ag/AgCl reference electrode in a 1M KOH electrolyte.

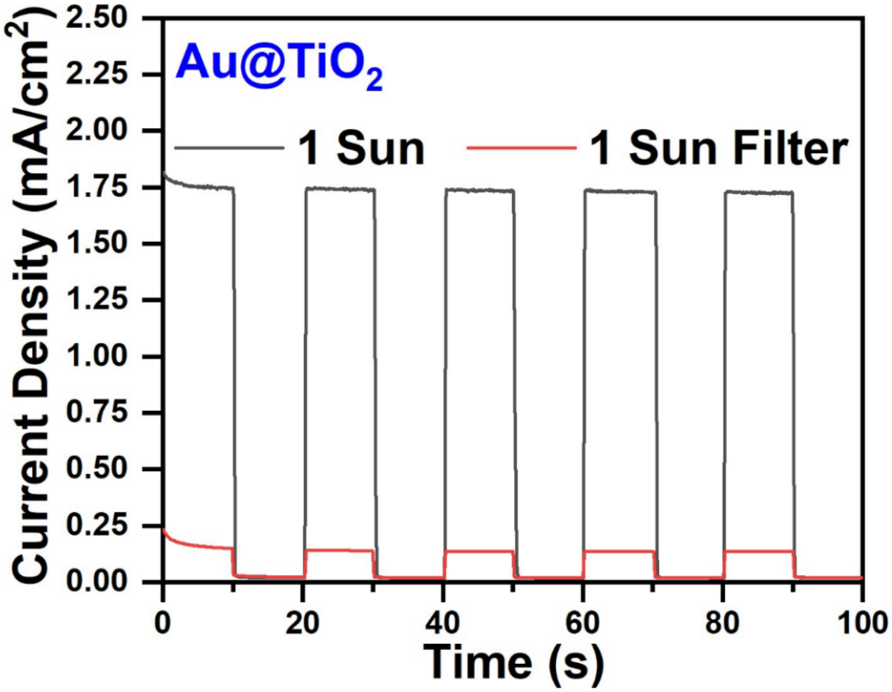

Figure 49. Photoelectrochemical measured I-t curves of Au@TiO_2 photoelectrode using the solar simulator and solar simulator with UV cut-off illumination under +0.6 V applied potential vs. Ag/AgCl reference electrode in a 1M KOH electrolyte.

In the hot carrier injection mechanism, depending on the generated hot electrons and hot holes' energy, both of them can get injected into the suitable host semiconductor. When Au nanoparticles are under visible light excitation, Au's holes can get excited both from the d band (interband transition) or within the s band (intraband transition) of Au. Usually, when holes are generated from the s band, the resulting electrons are energetic enough (hot electrons) to pass the Schottky barrier formed between the Au/semiconductor interface and get injected into the conduction band of the semiconductor. This well-studied process is known as hot electron injection. For Au nanoparticles, since excitation of charge carriers between the occupied energy levels of 6sp (near Fermi level) to unoccupied energy states of 6sp (intraband transition) is dominant under the excitation in resonant with LSPR [140], the action spectra of the photoelectrodes which work based on the hot-electron injection should usually follow the plasmon spectra.[120, 132, 141]

On the other hand, when the d band transition happens, the electrons' energy is not high enough to pass the Schottky barrier and get injected into the conduction band of TiO_2. In turn, the resulted holes generated from the d band transition are energetic enough to get injected into the defect states or valance band of a host semiconductor. This process is known as the hot hole injection process.[115, 133, 142, 143] The hot hole injection model predicts that as the energy of the incident photon decreases (from 460nm to 730 nm), the photocurrent should also decrease since the higher energy of the incident photon results in the formation of holes deeper in the d band states below the Fermi level of the Au. As the incident photon's energy decreases, the formed holes are less energetic, resulting in lower photocurrent density. Overall, the action spectrum trends of Au@a-TiO_2 photoelectrode suggest the injection of holes from the Au into the defect states or valance band of a-TiO_2 and KPFM result provides solid evidence for this theory.

Additionally, two sets of complementary experiments were conducted to study the charge transfer mechanism in the Au@a-TiO_2 photoelectrode. Firstly, instead of using the Au@a-TiO_2 as a photoanode (applying positive +0.6 V bias to the photoelectrode), this photoelectrode has been used as a photocathode by applying a negative bias to it (-0.6 V), Figure 50 exhibits the 1 sun photocurrent response of this photoelectrode under negative bias. Interestingly, the results again show a weak anodic photocurrent which means that even under applied negative bias to the Au@a-TiO_2 photoelectrode, Au nanoparticles are still injecting the holes to the outer a-TiO_2 shell. Secondly, the architecture of the Au@a-TiO_2 was reversed by changing the sequence of deposition of a-TiO_2 and Au (the thin amorphous layer of TiO_2 was deposited on the FTO substrate at first, and then the Au film were sputtered on top of it). This photoelectrode was named as a-TiO_2-Au Photoelectrode. In this case, the Au nanoparticles are only in direct contact with the thin amorphous TiO_2 layer and not with the FTO. Interestingly, when the applied voltage was -0.6 V against the reference electrode, the a-TiO_2-Au photoelectrode exhibited cathodic photocurrent (Figure 51), which indicates the injection of holes into the a-TiO_2 layer and deriving the reduction reaction at the interface of the a-TiO_2-Au and the electrolyte, these results again confirm the possibility of the injection of holes into the thin amorphous TiO_2 layer. Overall, the action spectrum measurement, electron/hole scavenger tests, KPFM, NIR UV-vis spectra, and changing the architecture of the Au@a-TiO_2 photoelectrode are well aligned with each other and suggest the injection of hot holes to the outer a-TiO_2 shell.

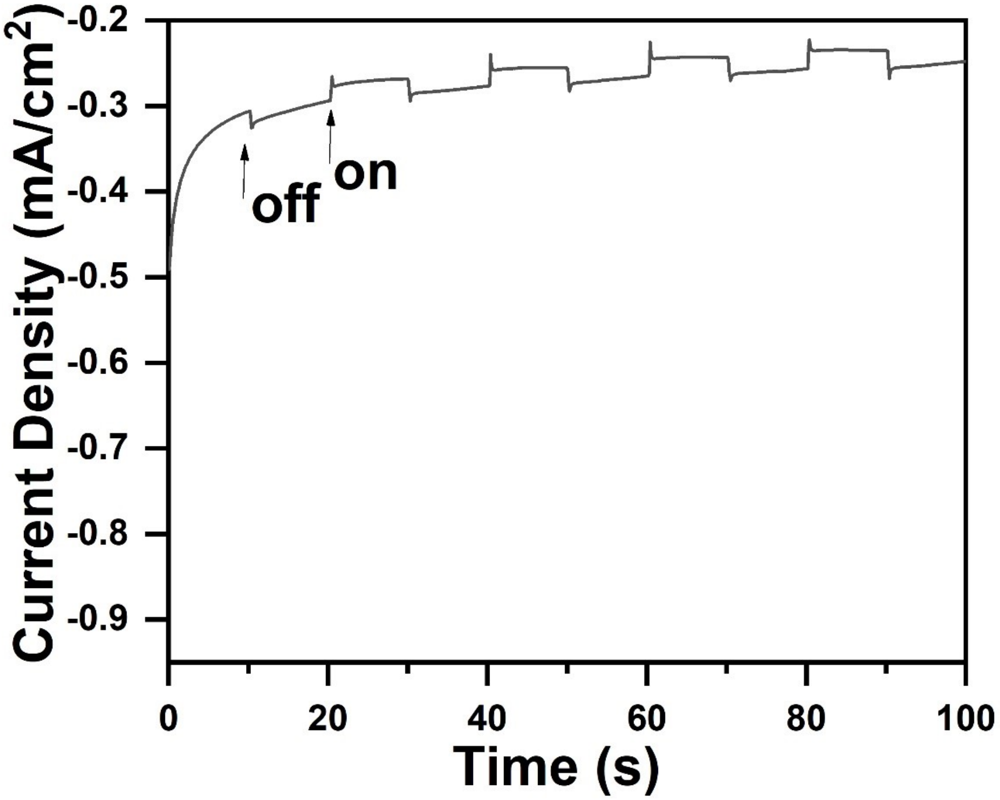

Figure 50. Measured it curves of Au@a-TiO$_2$ using solar simulator under -0.6 V applied potential vs. Ag/AgCl reference electrode in a 1M Na$_2$SO$_4$ electrolyte.

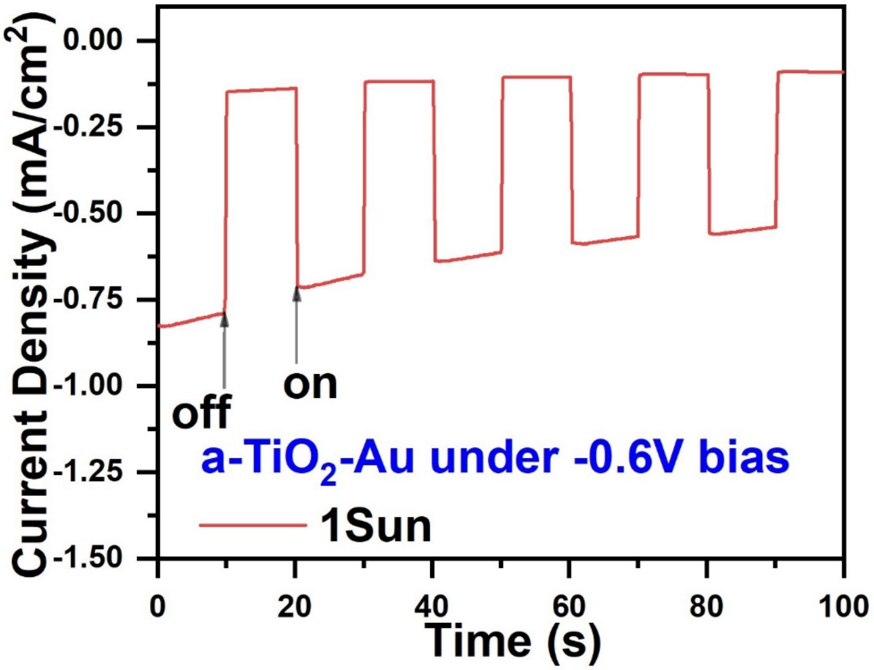

Figure 51. Measured it curves of a-TiO$_2$- Au photoelectrode using solar simulator under -0.6 V applied potential vs. Ag/AgCl reference electrode in a 1M Na$_2$SO$_4$ electrolyte.

Based on all these explanations, the charge transfer mechanism under visible light illumination for both Au@a-TiO_2 and a-TiO_2-Au configurations is depicted in Figure 52. Regardless of the positive or negative applied potential to the electrode, when Au@a-TiO_2 is under visible light excitation, it results in holes in the d band of Au nanoparticles which can get injected into the a-TiO_2 shell through defect states (Figure 52a). From there, these holes can participate in oxidation reaction at the photoelectrode/electrolyte interface. The electrons in this process will form near the Au's fermi level, which then can get injected to FTO and from there from the external circuit can reach the counter electrode (Pt electrode) to drive reduction reaction. For the a-TiO_2-Au architecture (Figure 52b), under visible light irradiation and negative applied potential, almost the same process will happen. The holes will form in Au's d-band. The holes get injected into the thin a-TiO_2 later. From there to the FTO and the counter electrode, electrons accumulated in Au participate in the reduction reaction at the a-TiO_2-Au/electrolyte interface.

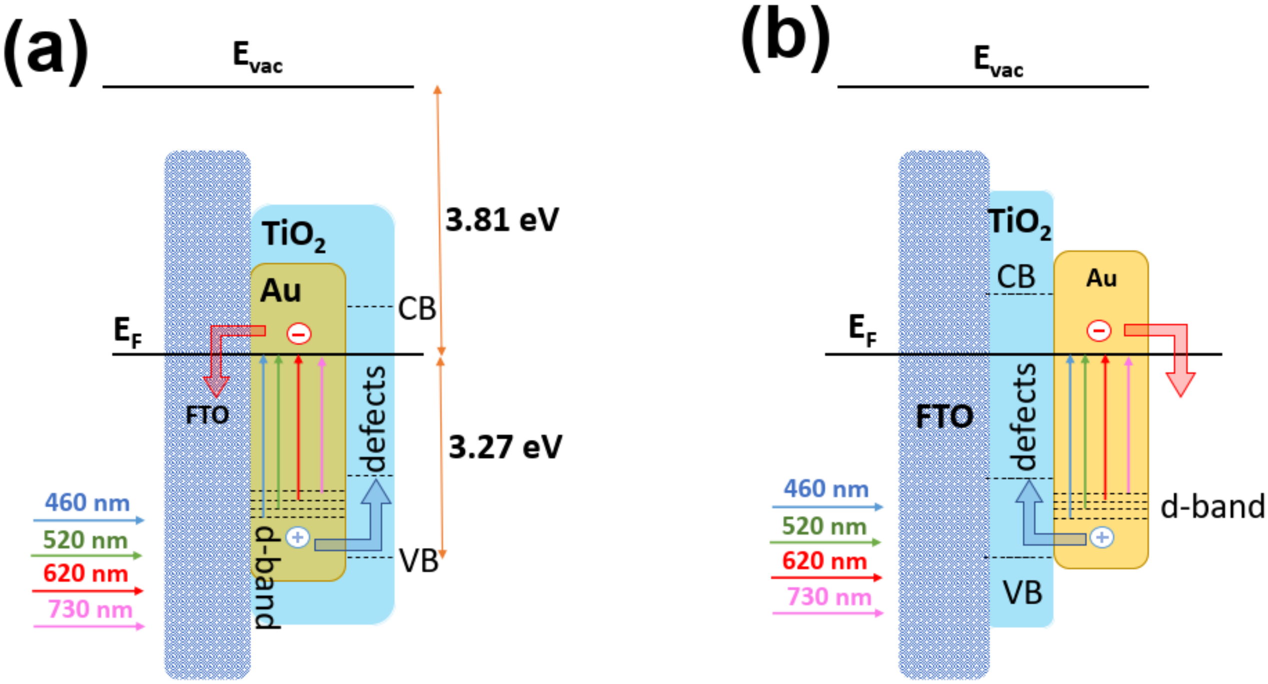

Figure 52. The proposed charge transfer mechanism of (a) Au@a-TiO_2 and (b) TiO_2-Au photoelectrodes.

4.4. Conclusion of chapter 4

In conclusion, we demonstrated that contrary to what is conventionally believed about the TiO_2 to be an excellent electron-accepting material, a thin amorphous layer TiO_2 (a-TiO_2) could act as a hole accepting material and a protective layer in PEC water-splitting photoelectrodes. Highly stable ultrathin Au@a-TiO_2 photoelectrode was fabricated by sputtering followed by ALD deposition methods. The photocurrent measurements were done on KOH and Na_2SO_4 aqueous electrolytes. The results show an outstanding photocurrent of 2.5 mA.cm^{-2} under 1 Sun illumination, which is almost 8.3 times higher than an ALD deposited amorphous TiO_2 (a-TiO_2) layer. In addition, the Au@a-TiO_2 photoelectrode exhibited strong absorption in the visible part of the solar spectrum and enhanced photocurrent generation compared to the a-TiO_2 layer under visible light irradiation. Substantial experimental and theoretical evidence of injection of holes from the decay of plasmon resonance of Au nanoparticles to the defects and mid bandgap energy states of a-TiO_2 was presented using action spectrum, hole scavenger test, NIR UV-vis spectra, and KPFM measurements. In the end, an unconventional mechanism of charge transfer in Au@a-TiO_2 based on hole injection was proposed.

5. Sponge shaped Au nanoparticles: A stand-alone photocatalyst for driving light-induced CO_2 reduction reaction via interband transition

In this chapter, background information about one of the essential attributes of a catalyst, porosity, is discussed. Highly porous gold nanoparticles (Au-Sponge) and spherical gold nanoparticles (Au-Island) were fabricated using thermal dewetting and subsequent acid etching process. Thorough characterization of the fabricated samples and measurement of the activity of the samples for CO_2 photoreduction reaction were also discussed.

5.1. Background and Motivation

Owing to their highly porous structure, supported metal catalysts are an essential family of heterogeneous catalysts with a wide range of applications in oxidation and reduction reactions.[144] In heterogeneous catalysis, the substrate is a highly porous material (usually made of metal oxides) that helps the reactants' adsorption and provides a platform for dispersing the metal nanoparticles. Metal nanoparticles made of materials such as Au, Pt, Pd, etc., act as the active phase where chemical reactions can happen.[144, 145] Unlike metals such as Pt and Pd, which lose their activity at low temperatures, Au remains active even at low temperatures, making it an attractive, active phase for catalytic applications. Au has been used to drive different chemical reactions such as CO_2 hydrogenation, CO oxidation, CH_4 Oxidation, and C-C coupling.[144, 146] Spherical gold nanoparticles with various sizes are the most common structure of the active phase, which have been utilized in different reports. Being metal, gold has the flexibility to deform into various shapes; gold nanoparticles with different shapes, including cubes, triangles, and sponge shapes, were fabricated using clever approaches such as the dealloying technique.[146-149] Because of its highly porous nature, the sponge shaped Au nanoparticles is of great importance for catalytic research as it has the potential to prevent the need for a highly porous substrate to operate as a catalyst in a catalytic process. Surprisingly, Au nanosponges have drawn little attention for catalytic applications so far; only a few reports successfully utilized this unique structure for purely catalytic CO oxidation and oxidative coupling of Methanol.[146, 150]

In addition to these properties, Au belongs to a family of metals known as plasmonic materials. Plasmonic materials can interact with incident visible light through excitation of localized surface plasmon resonance (LSPR) as well as incident UV-light through interband tranistion.[151] [147, 152] These interesting attributes of gold nanoparticles further increased the interests to utilize them for driving modern chemical reactions such as light-driven water-splitting or CO_2 photoreduction.[93, 151, 153]

While most of the studies were focused on the utilization of LSPR energy to drive chemical reactions, little attention was given to the utilization of hot electron-hole pairs generated by the interband transitions.[152] Interband transition is essential for photocatalytic applications as thermodynamic limitations of important photocatalytic reactions such as water-splitting and CO_2 photoreduction impose minimum energy for both the electrons and holes. For example, in a CO_2 photoreduction reaction, only electrons with energies higher than the reduction potential of CO_2 and holes with energies lower than the water's oxidation potential can participate in the overall reaction.[151, 154] Electron-hole pairs generated by interband transitions can meet these essential minimum energy requirements.

The unique physical (porousness) and optical properties (LSPR and interband transition) of sponge-shaped gold nanoparticles render them a suitable catalyst for light-driven CO_2 photoreduction reaction. Herein, we successfully fabricated nanosponge Au nanoparticles and successfully utilized them to reduce CO_2 using water under UV light excitation. The results of this work open a new door in the field of plasmonic catalysis, where unsupported porous plasmonic metal nanoparticles can facilitate complicated chemical reactions such as CO_2 photoreduction.

5.2. Plasmonic Catalysts preparation

Two different catalysts were fabricated. The first one was hemispherical-shaped gold nanoparticles which were named Au-Island, and the second one was sponge-shaped gold nanoparticles which were named as Au-Sponge. The Au-Sponge sample's fabrication process is similar to previous reports with minor modifications where Ag was used as a sacrificial metal.[147] Reports suggest that submerging a metallic alloy in an acidic environment dissolves the less-noble metal.[155] Figure 53 exhibits the schematic diagram of the fabrication process of Au-Sponge samples. Fluorine doped tin oxide glass (FTO) was used as the substrate. The substrates were cleaned with soap, methanol, and acetone first. Then the substrates were loaded inside a DC magnetron sputtering apparatus (Kurt J. Lesker Co.). After reaching the base pressure of 7 mtorr, the sputtering of the gold was done for 30 seconds with an applied potential of 75 W. The thickness of the sputtered Au film was 10 nm. After this step, the samples were unloaded, the target was replaced with an Ag target, the Ag sputtering was done for 15 seconds under the same pressure and applied potential of 300 W. After the sputtering step, the samples were placed inside a tube furnace (STF55666C-1, Thermo Scientific), the tube furnace had three controllers for accurately ramping up the temperature to 450 ^{0}C, the ramping up duration was 2 hours. Then the samples were annealed at 450 ^{0}C for 1 hour. Annealing of the samples resulted in hemispherical nanoparticles made of Au or Au-Ag alloy.[156] The annealed Au-Ag alloy nanoparticles (Figure 54a) were submerged inside the HNO_3 aqueous solution for 5 minutes to completely remove the Ag (sacrificial metal) the obtained transparent sample was named as Au-Sponge (Figure 54b). The fabrication process for Au-Island samples was the same without the sputtering deposition of the Ag and the subsequent acid treatment.

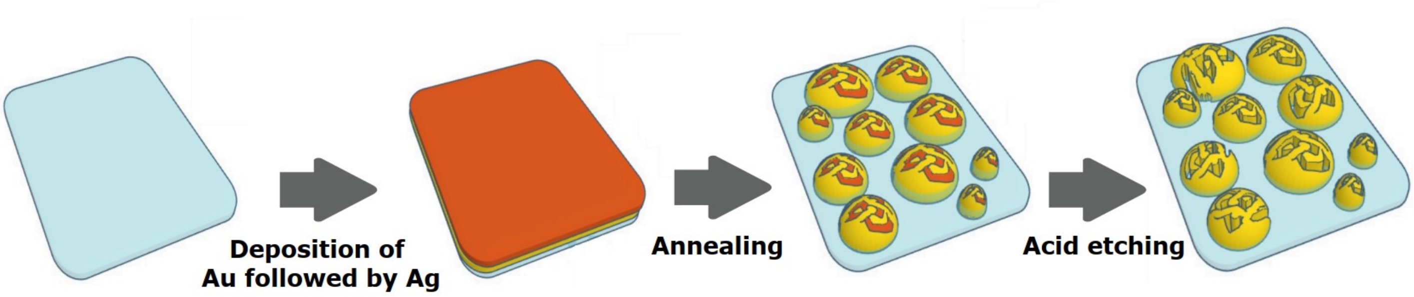

Figure 53. Schematic diagram of the fabrication process of the Au-Sponge sample.

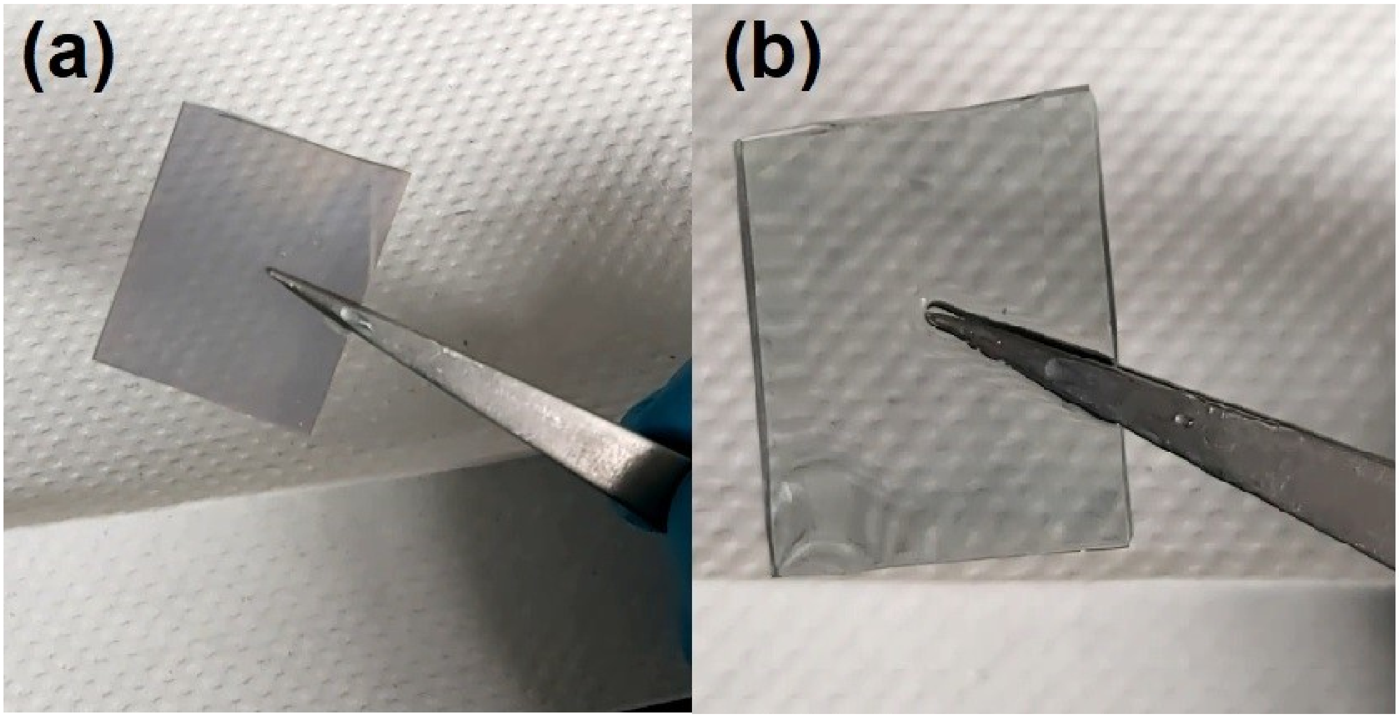

Figure 54. Photograph of the (a) Au-Ag alloy nanoparticles and (b) Au-Sponge sample (right after acid etching step).

5.3. Results and Discussion

The morphology of the fabricated samples were investigated by field emission scanning electron microscopy (FESEM). Figure 55 exhibits the FESEM images of the Au-Island sample. The successful dewetting of the sputtered gold film, and formation of the hemispherical-shaped gold nanoparticles is evident from this image. The fabricated Au nanoparticles had different sizes from 20 nm to 140 nm with an average size of 100 nm, shown by the particle size distribution in Figure 55. Figure 56a exhibits the morphology of the Au-Sponge sample. The porous structure of the Au-Sponge sample is conspicuous from the SEM image. The particle size distribution is also shown in the inset of this figure. The nanoparticles' size varied from 20 nm to 180 nm with a mean particle size of 100 nm. The Energy-dispersive X-ray spectroscopy (EDS) elemental mapping of the Au-Sponge sample indicated the presence of O, Sn, and Au (Figure 56b), no peak related to Ag was detected, which confirms the successful removal of the sacrificial Ag layer by acid treatment.

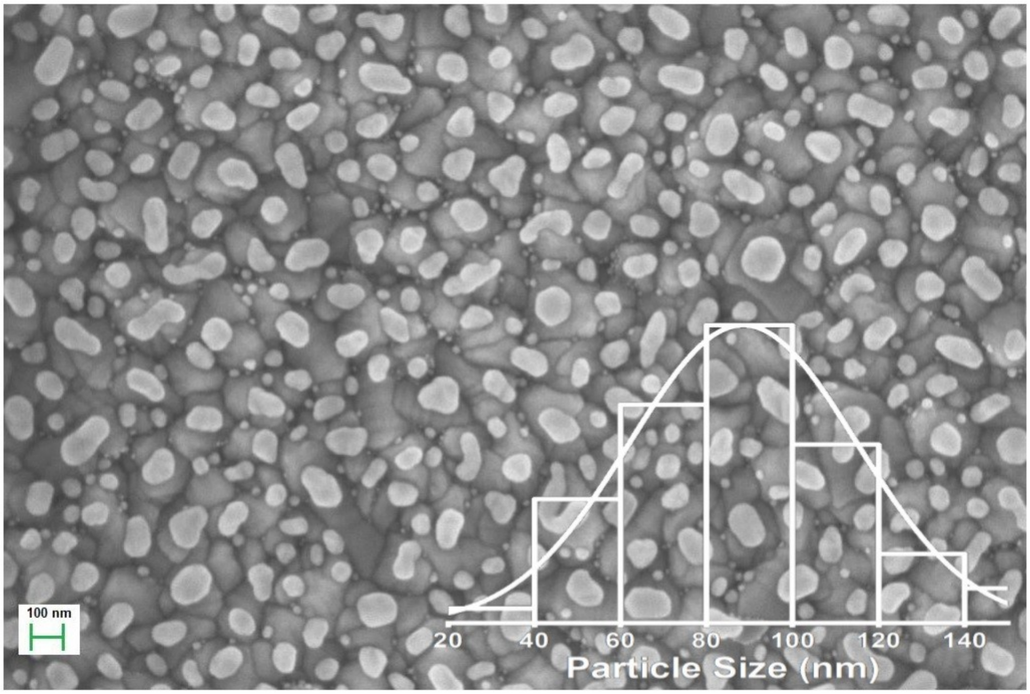

Figure 55. Scanning electron microscopy (SEM) images of Au-Island sample.

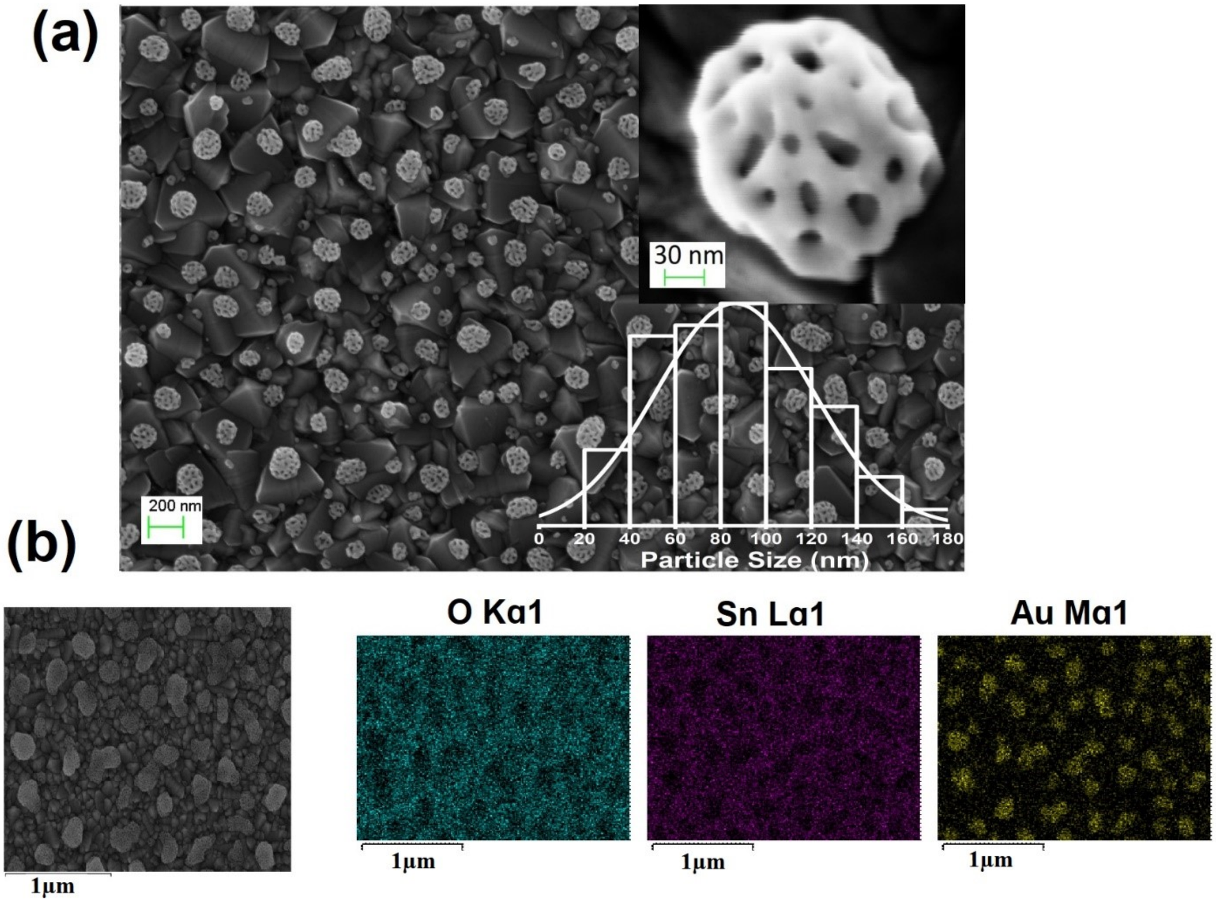

Figure 56. (a) Scanning electron microscopy (SEM) images of Au-Sponge sample and (b) SEM image of the selected region of Au-Sponge sample for energy-dispersive x-ray spectroscopy (EDS) mapping along with elemental mapping of O, Sn, and Au.

The interaction of nanomaterials with an incident electromagnetic wave can provide helpful information for plasmonic and photocatalytic applications. To investigate this, the UV-vis-NIR spectroscopy and finite difference time domain (FDTD) simulations were conducted. Figure 57a exhibits the UV-Vis-NIR spectra of the Au-Island and Au-Sponge samples and Figure 57b displays the corresponding absorption cross-section of these two structures obtained from FDTD simulation. Au-Island sample exhibited LSPR at 550 nm, which is the intrinsic LSPR peak of gold; this is also supported by the FDTD simulation (dashed red lines in Figure 57b).[151]

The presence of holes inside the Au-Sponge structure makes its refractive index different from pure gold. The different refractive index of Au-Sponge renders its structure to interact differently with the incident electromagnetic wave. Compared to the Au-Island sample, the Au-Sponge nanoparticles' LSPR peak shifted to 825 nm as a result.[147] The FDTD simulated absorption cross-section of the Au-Sponge (dashed black lines in Figure 57b) also exhibits the same trend.

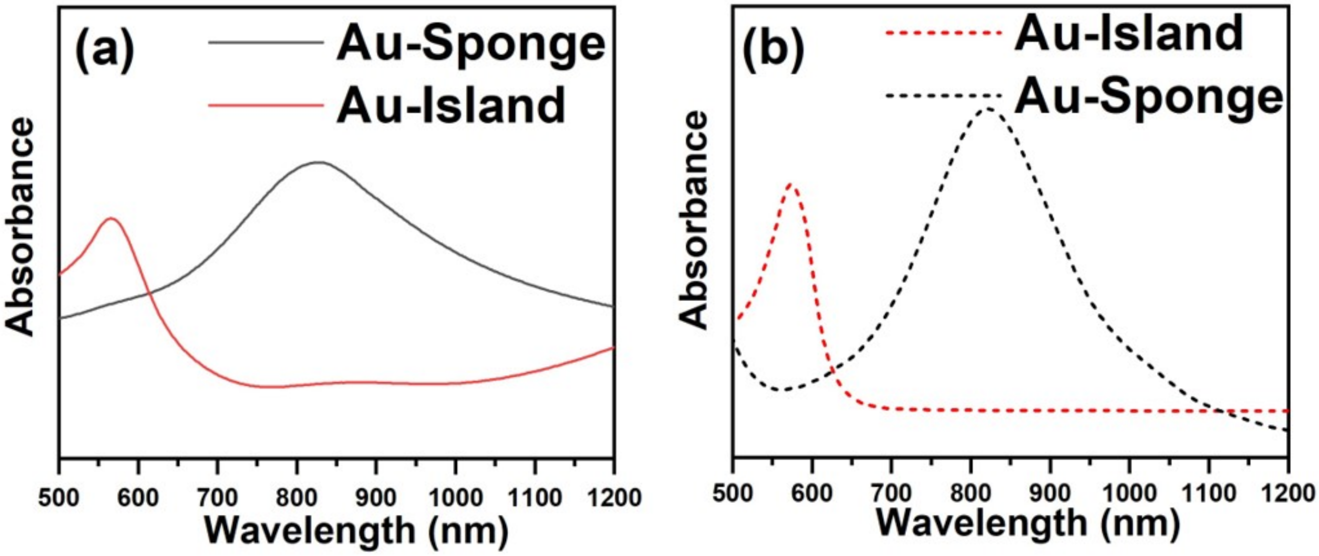

Figure 57. UV-Vis spectra of Au-Sponge and Au-Island samples. (b) FDTD simulated absorption cross-section of Au-Sponge and Au-Island samples.

The XRD pattern of Au-Island and Au-Sponge samples are shown in Figure 58. These samples' XRD pattern exhibit a sharp peak at $2\theta = 38$ corresponding to Au (111) plane. Smaller peaks related to Au (200) and Au (311) at $2\theta = 44$ and $2\theta = 77$ were also detected.[151, 157] Other peaks related to FTO could also be found in the XRD pattern of these samples.[158, 159] The XRD could not observe any peak related to Ag, which again suggests that the sacrificial Ag layer was completely removed during the HNO_3 acid treatment.

The nature of bonds and the chemical composition of atoms at the surface of the Au-Island and Au-Sponge samples were investigated using X-ray photoelectron spectroscopy (XPS) (Figure 59). The long-range survey scan of both samples revealed Sn, Au, O, and carbon impurities (Figure 59a). To further confirm Au's presence, higher resolution XPS spectra at the Au4f region were collected for both Au-Island and Au-Sponge samples (Figure 59b,c). The collected spectra exhibited two peaks centered at BE= 83.87 eV and BE= 87.64 eV, which correspond to Au4f$_{7/2}$ and Au4f$_{5/2}$, respectively which further proves that the chemical state of Au did not change during the fabrication process.[151]

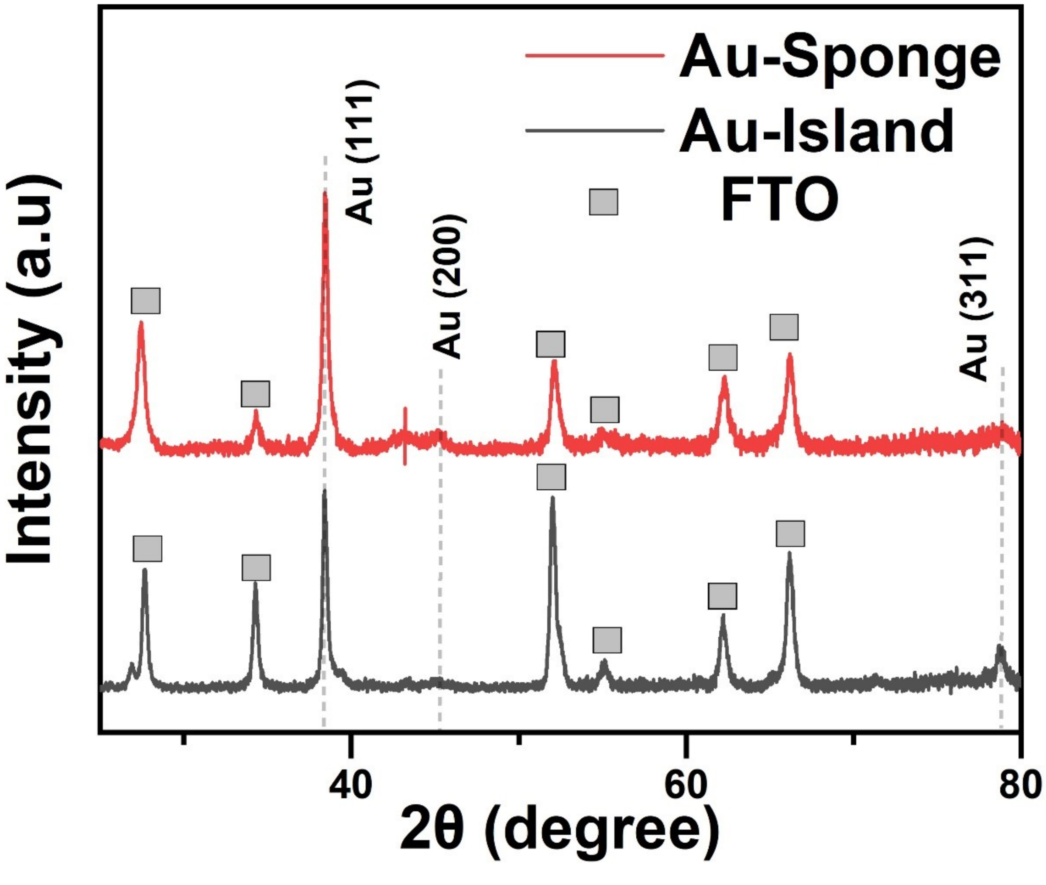

Figure 58. The XRD pattern of Au-Island and Au-Sponge samples, gray box shows the peaks related to FTO.

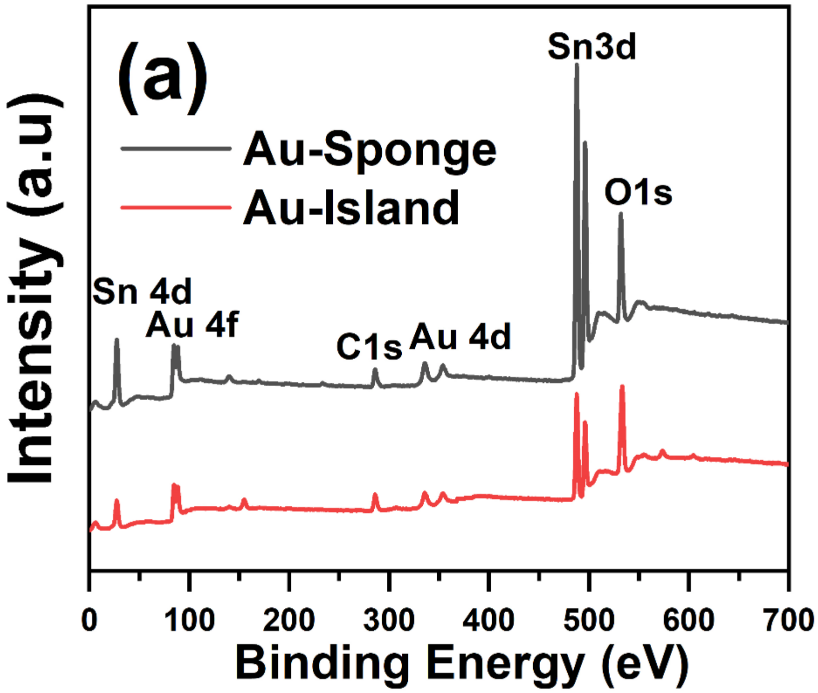

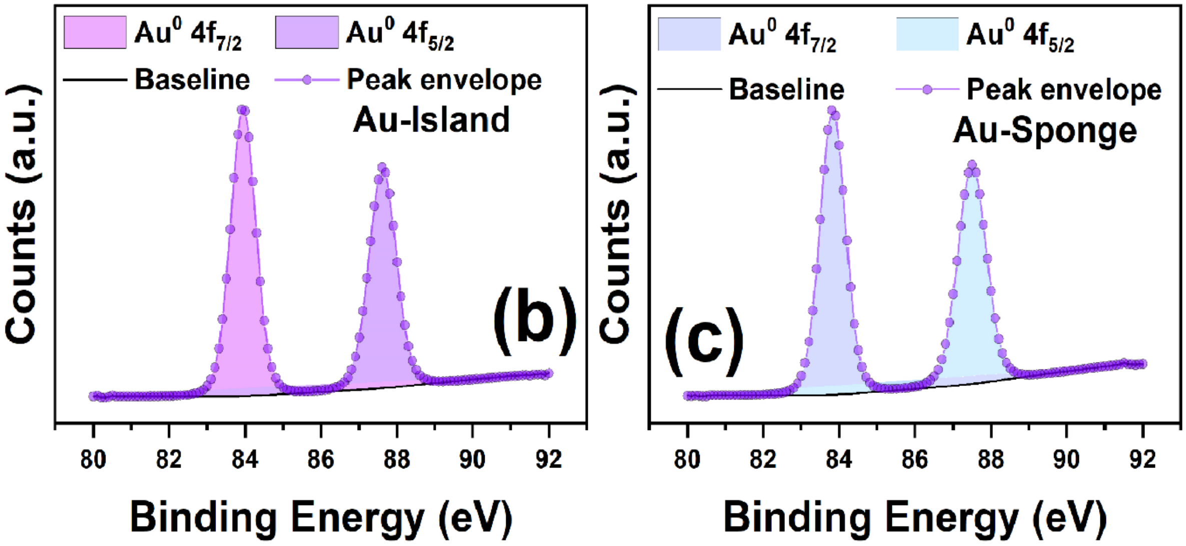

Figure 59. (a) XPS survey scan of Au-Island and Au-Sponge, high-resolution XPS spectra of (b) Au-Island and (c) Au-Sponge sample in Au 4f region.

The performance of fabricated samples for CO_2 photoreduction was investigated using the high-pressure stainless-steel reactor using CO_2 and water vapor as the reactants. After 2 hours of irradiation using the 255 nm U.V. lamp (Figure 60 exhibits the emission spectrum of the U.V. lamp), the headspace gas was analyzed with the GC, which reported the product in ppm, the amount of products was converted into μmol. g-1.hr^{-1} using ideal gas law (refer to chapter 2 for the conversion process).

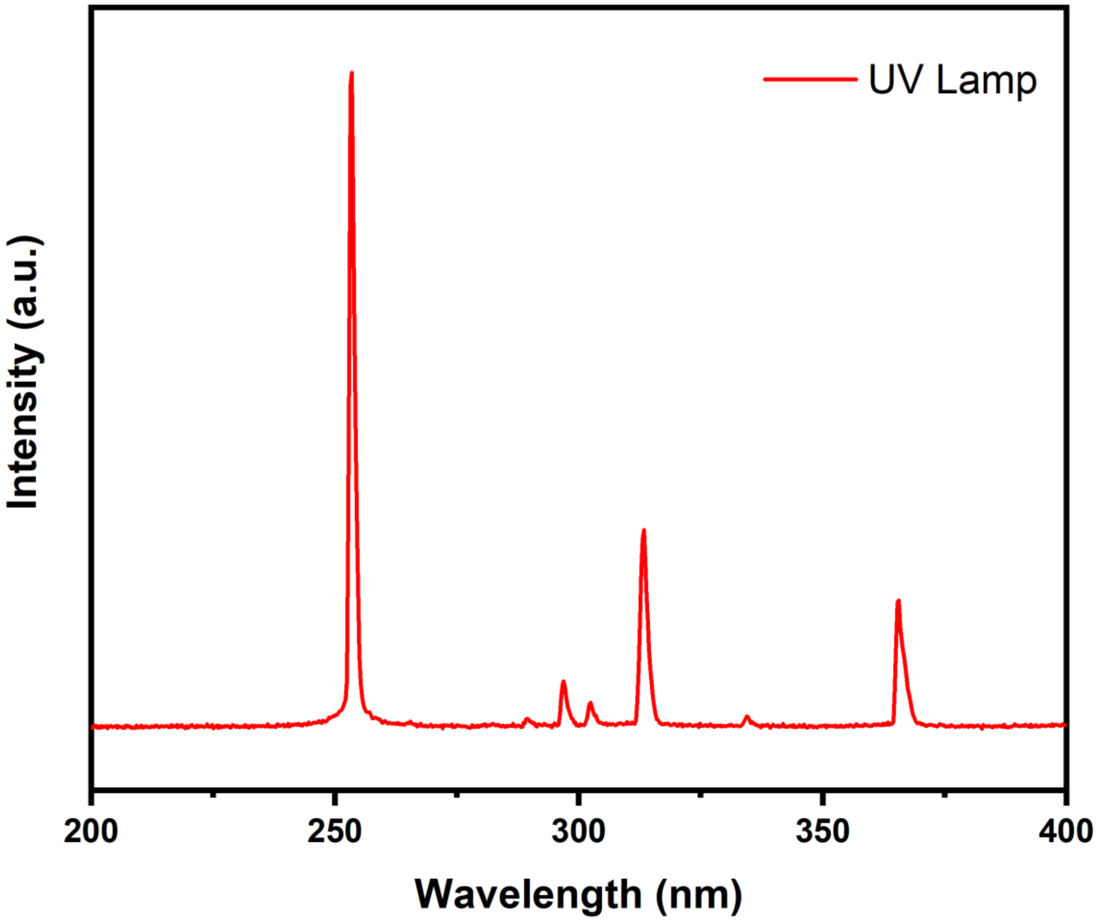

Figure 60. The emission spectrum of the U.V. light source used for CO_2 photoreduction reaction.

The rate of methane production under UV lamp irradiation is reported in Figure 61. The superior performance of Au-Sponge photocatalyst for CO_2 photoreduction is evident from these results as the rate of methane production was 153 μmol. g-1.hr^{-1} and 582 μmol. g-1.hr^{-1} for the Au-Island and Au-Sponge samples, respectively. This is a remarkable 3.8-fold increase in photocatalytic performance as the structure changes from regular hemispheres to porous nanosponges, proving that the shape of the nanostructure has a major effect on their photocatalytic activity. A few sanity tests were conducted to confirm that the methane was produced due to the photoreduction process. The sanity tests were including using high-pressure nitrogen instead of CO_2 inside the reactor, conducting the CO_2 photoreduction reaction without the photocatalyst, and conducting the reaction under dark conditions (without U.V. light illumination). No methane could be detected in all these sanity tests, which proves CO_2, photocatalyst, and light are vital for the successful photoreduction of CO_2. To rule out any carbon contamination effect on the production of observed products, a labeling test using $^{13}CO_2$ instead of $^{12}CO_2$ was done under identical conditions. GC-MS was used to analyze the product of the labeling test. Figure 62 exhibits the labeling test result, which shows a peak at m/z = 17, related to $^{13}CH_4$. The result of the labeling test rules out the contribution of Carbon contaminations in the observed product.

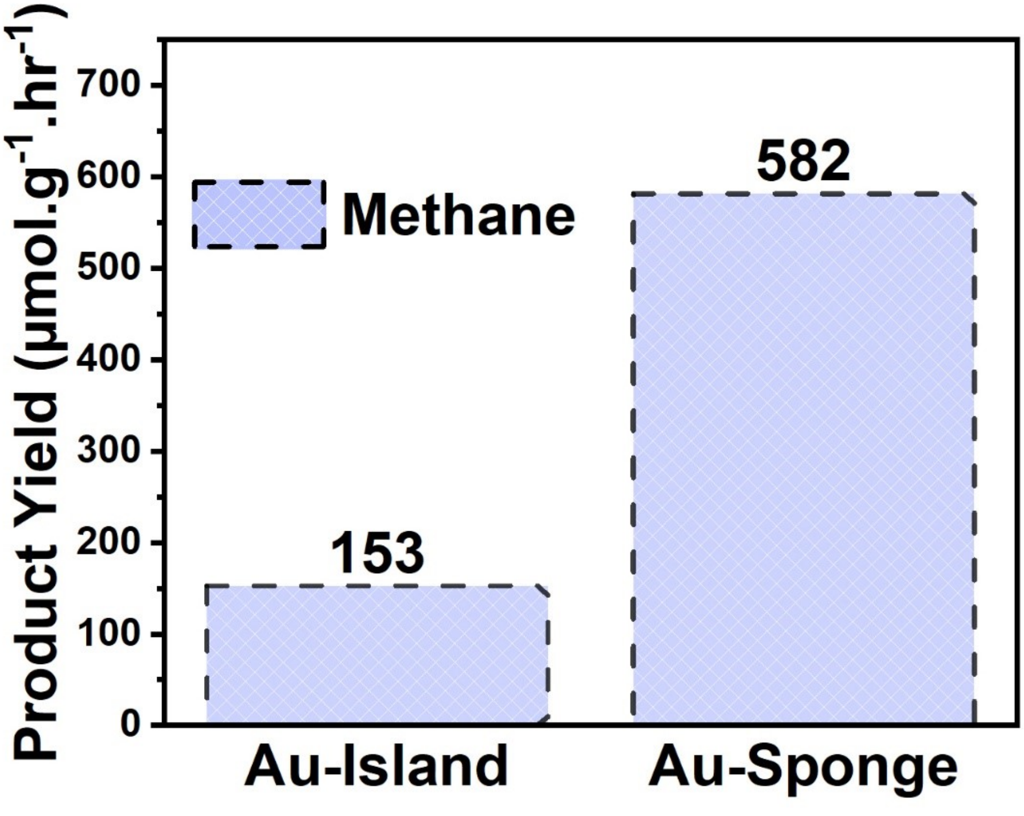

Figure 61. CO_2 photoreduction product yields of Au-Sponge and Au-Island samples.

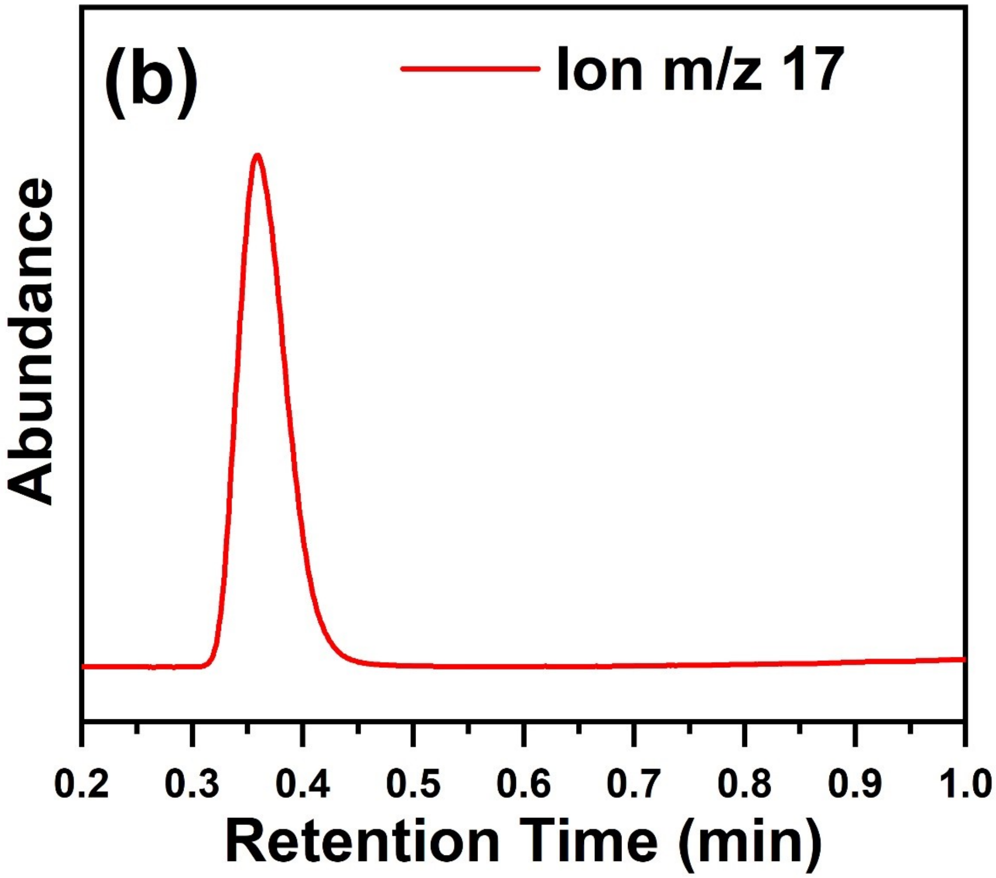

Figure 62. GC-Ms ion chromatography at ion m/z = 17 obtained from labeling test, which confirms the presence of $^{13}CH_4$.

The outstanding performance of the Au-Sponge sample compared to Au-Island raises this critical question that what would the possible reason/mechanism for this exceptional performance? To answer this question, a few complementary investigations were conducted. As previously mentioned in the introduction, one of the essential features of a potent catalyst is its porosity; porosity helps the catalyst bring the reactants to close contact at the surface (adsorption of the reactants) of the catalyst more efficiently. While SEM images clearly show Au-Sponge's porous structure, it also shows the lack of porosity in the Au-Island sample. Cyclic voltammetry (CV) measurements were conducted to estimate the surface area of the Au-Island and Au-Sponge samples (refer to chapter 2 for details about the procedure).[160-162] Figure 63 exhibits the oxidation and successive reduction of Au-Island and Au-Sponge samples during the CV measurements. The CV of an unannealed Au Film (Au-Film) was also measured as a reference. The forward bias oxidation of the Au-Sponge sample exhibits three peaks (Figure 64) corresponding to the AuO formation. The first two peaks are related to the following reaction:

$$Au + H_2O \rightarrow Au - OH + H^+ + e^- \qquad (19.)$$

While the third peak is related to the reaction:

$$Au - OH \rightarrow Au - O + H^+ + e^- \qquad (20.)$$

The first two peaks in the CV of Au-Sponge are related to the preferential adsorption of OH^- on step and terrace adsorption sites.[160] The absence of such a peak in the CV of Au-Film and Au-Island samples shows the lack of such adsorption sites on these samples. The surface RF, ECSA, and SSA of the samples were calculated using equations 14 and 15 (chapter 2), and the results are reported in Table 2. The SSA of the Au-Sponge sample is almost 2.6 times higher than the SSA of the Au-Island sample. The higher SSA of Au-Sponge results in this sample's higher ability to absorb the gaseous reactants and enhance its ability to catalyze a chemical reaction.[163]

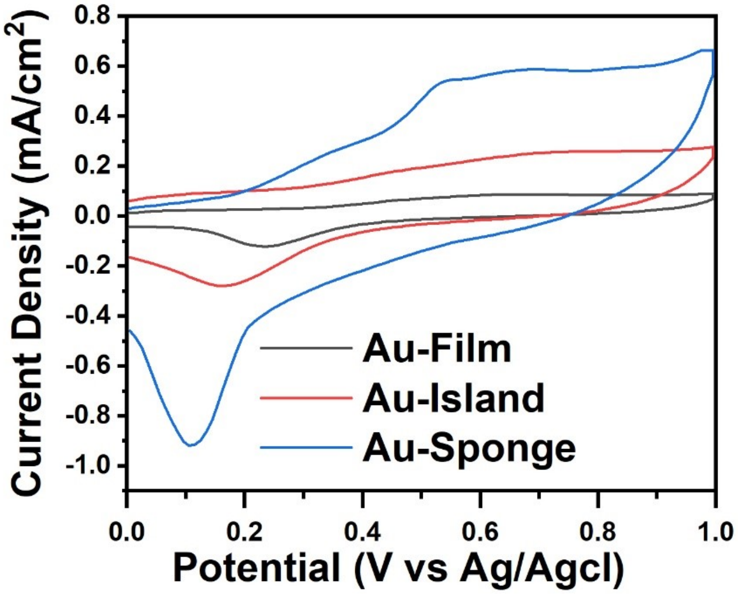

Figure 63. CV measurements of Au-Island, Au-Sponge, and Au-Film sample.

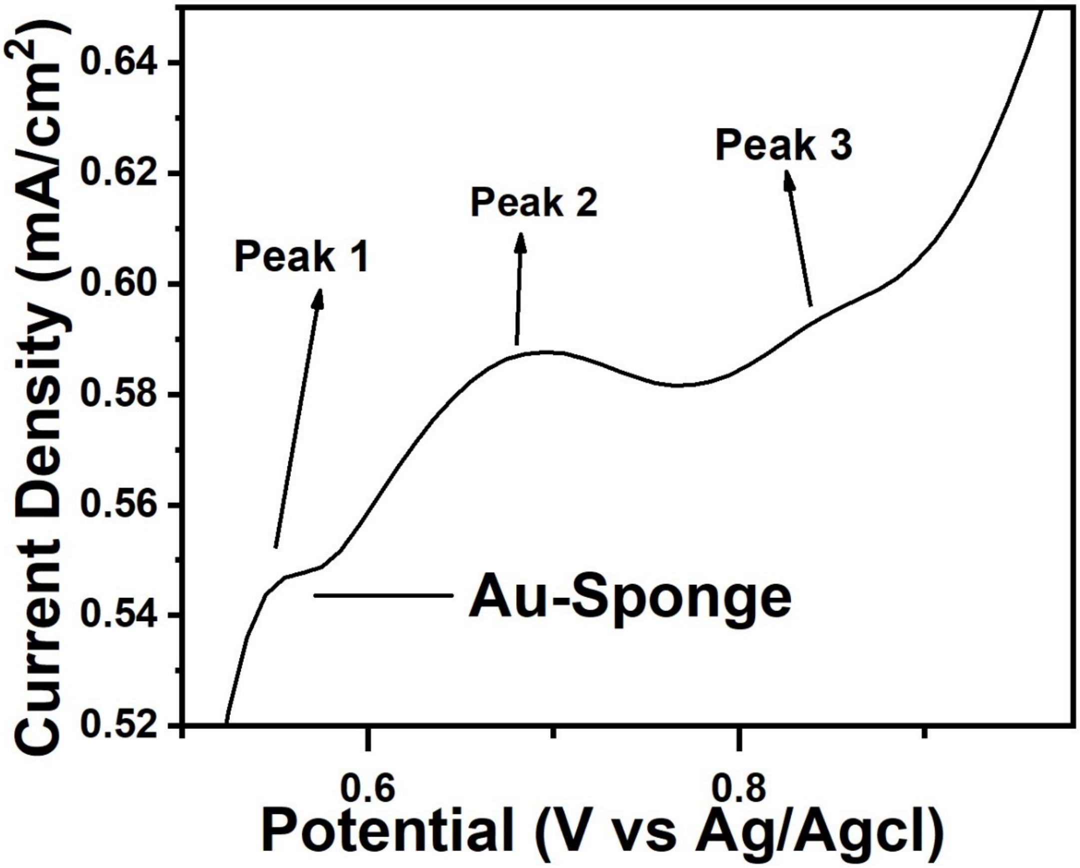

Figure 64. Peaks related to oxidation of Au in forward bias scan of the Au-Sponge sample.

In heterogeneous catalysis, a catalyst's overall activity is the sum of different active sites' contributions.[164] The presence of low coordinates surface sites such as steps, terraces, and kink atoms is highly beneficial for a heterogeneous catalyst's catalytic activity.[165]

For instance, the low coordinate surface sites can enhance the adsorbate-catalyst adsorption energy, which enhances the catalyst's catalytic activity.[163] The density functional theory (DFT) calculations also suggested that the catalytic activity of Au atoms with the lower coordinate number are significantly higher.[166, 167] The CV peaks related to the oxidation of Au-Sponge in the forward bias sweep already suggest the presence of such low coordinate surface atoms in the Au-Sponge sample. Besides, curved shapes of the ligaments and high surface to volume ratio of the Au-Sponge also increase the chance of the presence of low coordinate Au atoms at the surface of the Au-Sponge.[146, 166] Overall, the SSA measurement of the Au-Sponge is suggestive of the fact that this sample possess all the traditional attributes of an efficient heterogeneous catalyst such as high surface area and high density of low coordinate surface active sites.

Table 2. The calculated RF, ECSA and SSA of Au-Island and Au-Sponge.

Sample name	RF	ECSA (cm2)	SSA (m2/g)
Au- Island	2.83	0.89	14.6
Au-Sponge	7.28	2.30	37.76

For a light-induced reaction such as CO_2 photoreduction, in addition to porosity, the interaction of light with the catalyst is of most significant importance. The interaction of the Au-Island and Au-Sponge sample with UV light was investigated by obtaining their visible to near-infrared (NIR) light absorbance before and after irradiation with the UV light (Figure 65).

It is well-known that the free charge carriers exhibit light absorption in the NIR.[151] It is evident from Figure 65 that both Au-Island and Au-Sponge samples showed enhanced light absorption after UV light irradiation which suggests the excitation of electron-hole pairs in both of these samples. Interestingly, the enhancement of NIR light absorbance for Au-Sponge is more pronounced compared to the Au-Island sample, which suggests that interaction with UV light resulted in more concentration of free carriers in the Au-Sponge sample. To get an insight into the interaction of UV light with these samples, FDTD simulations were carried out. Figure 66a,b,c,d exhibits the top and cross-sectional view of the simulated electric field profile of Au-Island and Au-Sponge samples under 255 nm excitation. The electric field profiles suggest the strong interaction of the Au-Sponge sample with incident UV light at areas in the vicinity of the pores known as hot spots.[168] Compared to Au-Sponge, the Au-Island exhibit the hot spots only on the gold/air interface edges.

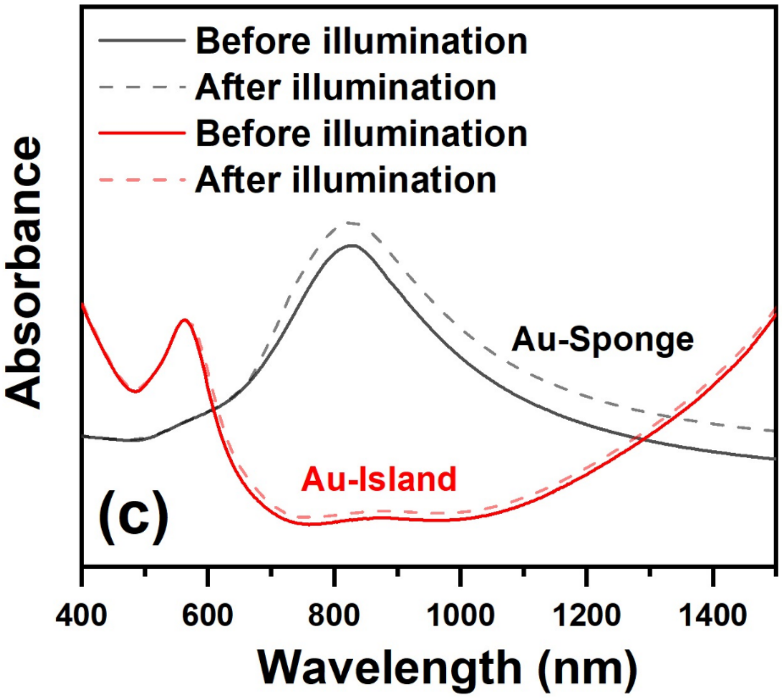

Figure 65. Vis-NIR absorption spectra of Au-Sponge and Au-Island samples before and after UV light irradiation.

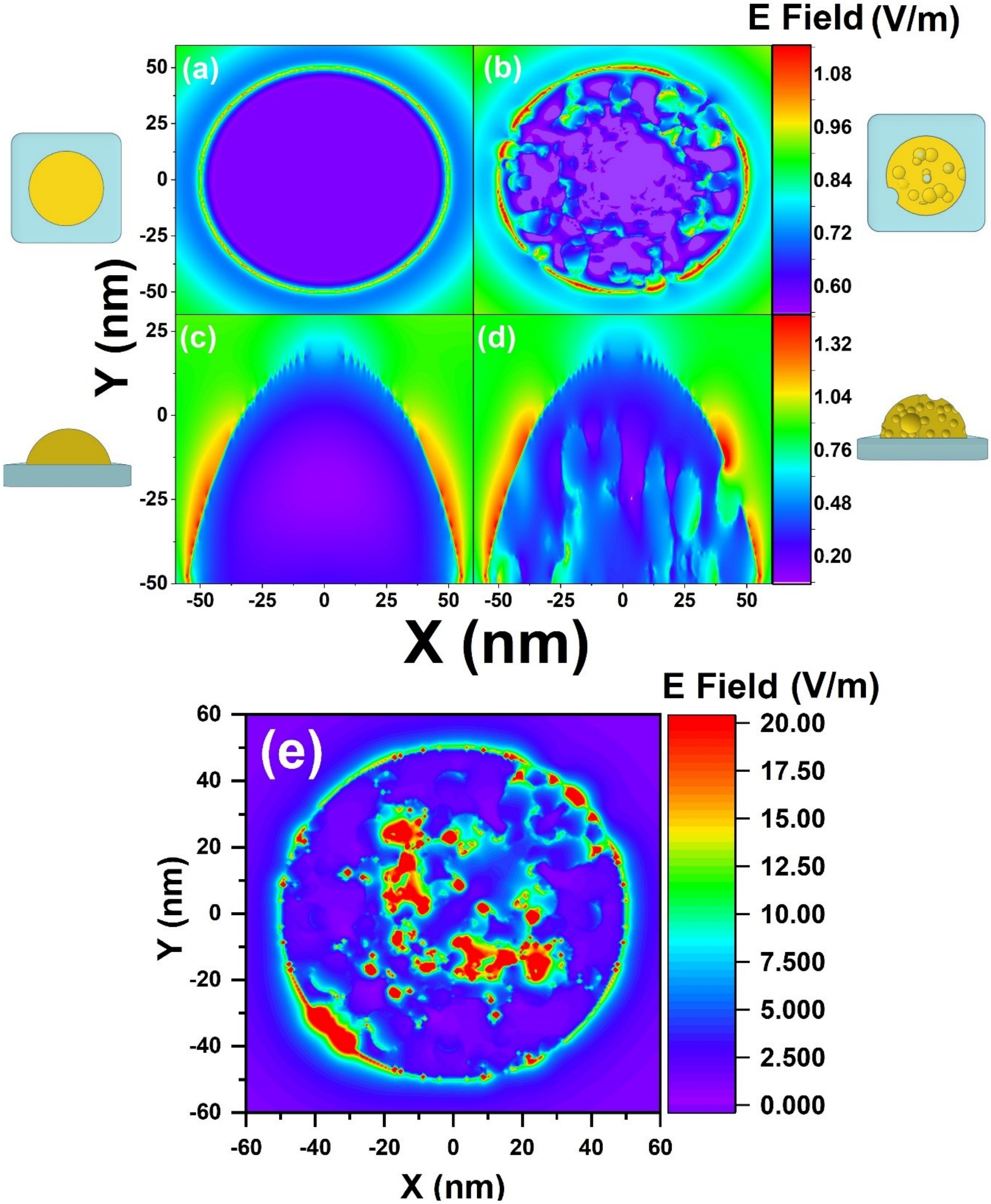

Figure 66. Top view (a,b) and cross-sectional view (c,d) of FDTD-simulated electric field intensity of Au-Sponge (b,d) and Au-Island (a,c) samples under 255 nm excitation. (e) Top view of FDTD- simulated electric field intensity of Au-Sponge under LSPR (825 nm) excitation.

The simulations were checked with literature and found to agree. Figure 67 replicates the simulations of Au-sponge nanoparticles under LSPR excitation reported in the literature.[169] As seen from these simulations, hot spots can be seen right at the pores (Au/air interface). My simulations (Figure 66e) close to the resonance frequency (825 nm) also show the same behavior. However off resonance (255 nm) simulations show the hot spots at the Au/glass substrate interface and the Au/air interface. In contrast, the Au/glass substrate exhibited a higher density of hot spots, probably due to the higher refractive index of the glass substrate.

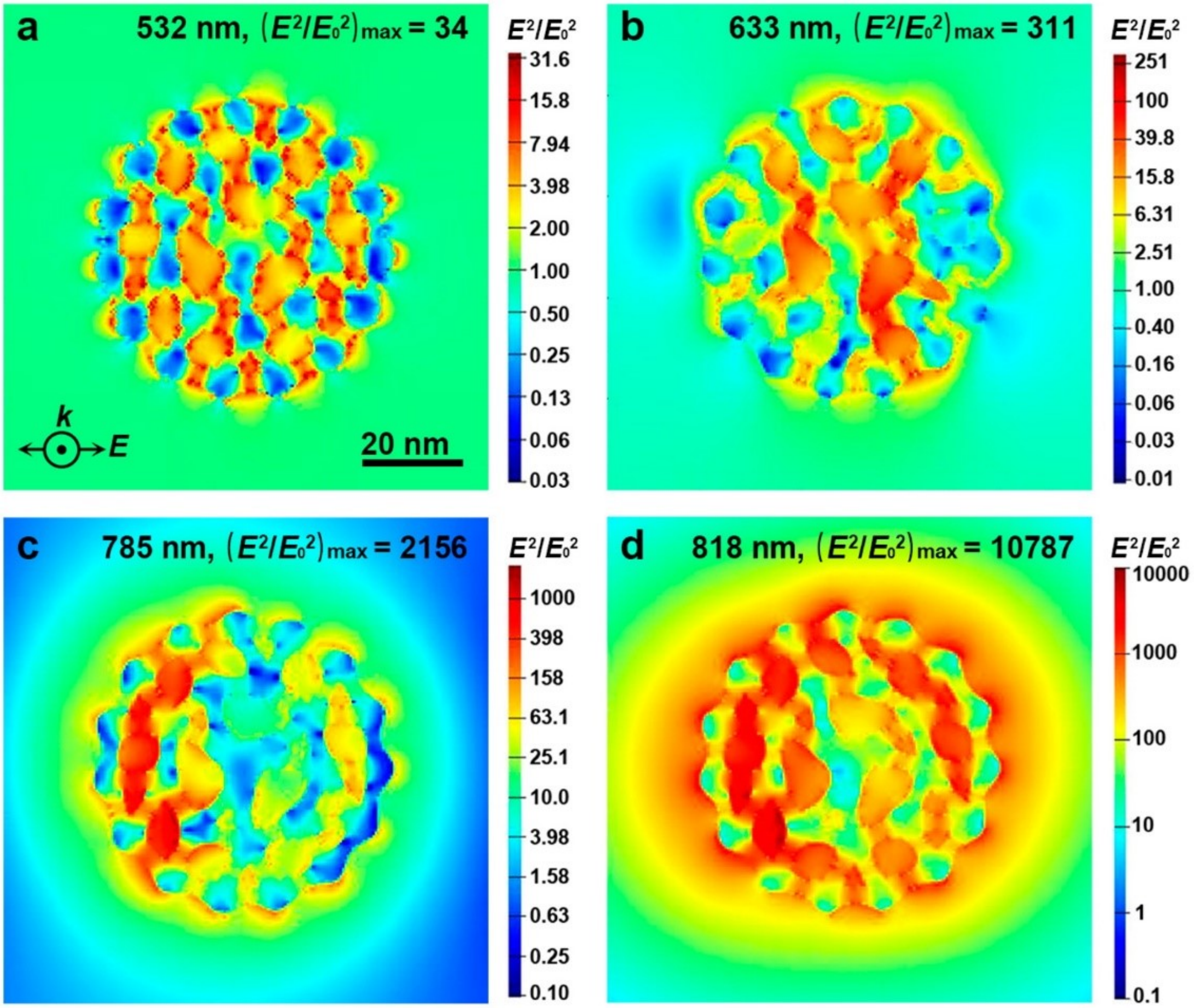

Figure 67. Simulated near-field electromagnetic field distributions of 60 nm diameter porous AuAg NPs in air medium irradiated by an incident plane wave with wavelength of (a) 532 nm, (b) 633 nm, (c) 785 nm, and (d) 818 nm (on-resonance condition), respectively. Reprinted with permission from K. Liu et al. Nano Letters (2014). All simulations were performed in Lumerical FDTD Solutions.[169]

The field outside the Au-sponge looks relatively high (the green area surrounding the Au-Sponge nanoparticles); this is probably because of the reflection of light by glass and the size of the monitor.

Carrier confinement effects cannot be ignored in Au and Ag nanoparticles while they play a minor role in thin films of Au and Ag.[170] One of the effects of carrier confinement is a heightened interaction between electrons and holes, which results in a much stronger interband-type Landau damping (hot carrier pair creation) effect in nanoparticles.[170] In very high surface area, porous metallic nanostructures (e.g., Au-sponge), it is conceivable that a substantial fraction of the hot carrier population produced by Landau damping is created within a mean free path of the surface, where reactant or adsorbed species are present. Therefore, a much higher efficiency of utilization of even short-lived hot carriers produced by interband damping, can be expected in an Au-sponge even in the absence of built-in electric fields such as those afforded by a heterojunction. The differences between the energy distribution of electron-hair pairs produced by interband and intraband damping could explain the high product yields observed solely in UV photon-initiated CO_2 photoreduction using Au-sponge. When photoexcited by visible photons close to the localized surface plasmon resonance, CO_2 photoreduction was not observed. While broad spectrum visible light harvesting is desired, this was not achieved for isolated Au-sponge nanoparticles on glass substrates. The main reason for this is that hot d-band holes generated by interband damping of the bulk and surface plasmon modes in Au have 1.5-2.5 eV available to them to drive CO_2 photoreduction (more thermodynamic driving force). On the other other hand, s-band holes formed by intraband damping of the surface plasmon are close to the Fermi level and have < 1 eV of excess energy available to drive chemical reactions. These facts are well-established by the work of Atwater and others.[171] It is expected that well-designed Z-scheme heterojunctions of the Au sponges with suitable semiconductors will enable higher reaction rates driven by visible photons through the use of energetic valence band holes of the semiconductor working synergistically with the energetic hot electrons of Au to perform CO_2 photoreduction.

Overall, the investigation of the NIR light absorption of the Au-Island and Au-Sponge sample along with the FDTD simulated electric profile of these two samples suggest the strong interaction of Au-Sponge with incident UV light and generation of electron-hole pairs because of UV light excitation. These results with the results obtained from the SSA calculations in the previous section evidence that the porosity prizes the Au-Sponge sample with multiple valuable attributes that help Au-Sponge outperform the Au-Island sample in CO_2 photoreduction reaction.

Ultraviolet photoelectron spectrum (UPS) of Au-Sponge was acquired to understand the charge transfer mechanism (Figure 68). The work function value was estimated using WF (ϕ) = 21.21−$E_{\text{cut-off}}$, where 21.21 eV is the energy of the incident, He I line of a He discharge lamp, and $E_{\text{cut-off}}$ is the cut-off energy of secondary electrons.[172] The ionization potential (the equivalent of the position of the d-band in Au containing structure) was estimated by subtracting the width of the UPS spectrum from the energy of the excitation source (21.21 eV).[93, 153] The values calculated for the WF and d-band position was 4.8 eV and 7.8 eV respectively which is well aligned with the values reported in the literature.[173] Based on the experimental findings and the WF's calculated values, and the d-band position of Au-Sponge, a proposed charge transfer mechanism is deduced and illustrated in Figure 69. For CO_2 photoreduction reaction, the energy of generated electrons and holes should meet a specific threshold to drive the oxidation and reduction half-reactions. The photo-generated electron's energy should be more negative than the reduction potential of CO_2/CH_4 (-0.244 V vs. NHE). The energy of the photo-generated hole should be more positive than the oxidation potential of H_2O/O_2 (0.82 V vs. NHE).[70, 93, 151] Based on the calculated values for the WF and d-band position, the energy of the UV lamp (255 nm = 4.86 eV) will result in an interband transition from d-band to s-band of the Au-Sponge, both electron, and holes produced by this transition meet the thermodynamic criteria needed for CO_2 photoreduction.

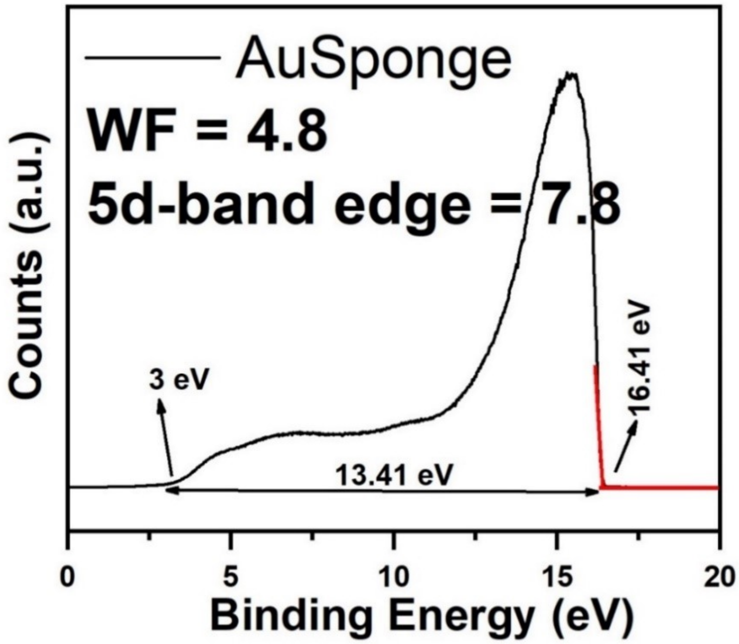

Figure 68. UPS work function spectra of Au-Sponge sample showing the calculated values for the WF and ionization potential.

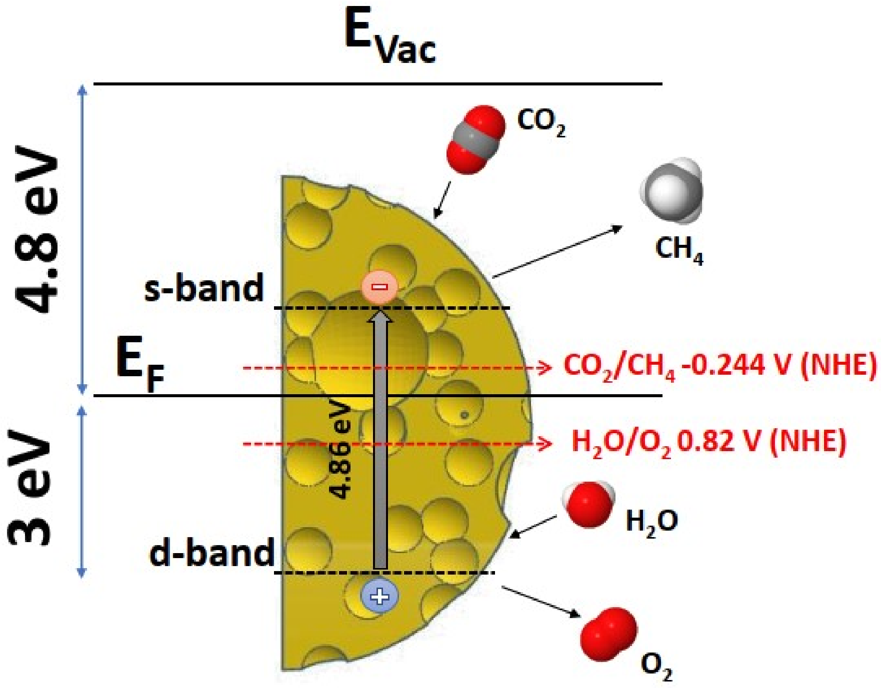

Figure 69. The proposed charge transfer mechanism of CO_2 photoreduction on the Au-Sponge sample.

5.4. Conclusion of chapter 5

Conventionally, gold alone was not considered as a suitable catalyst for driving a complex chemical reaction due to its inertness, but gold nanoparticles supported on top of highly porous substrates were proven to be potent catalysts. Highly porous gold nanoparticles are the new generation of heterogeneous catalysts where gold nanoparticles themselves are porous. Therefore, they obviate the need for a highly porous scaffold to drive the chemical reaction. Porosity can increase reactants' absorption ability and bring them in the close vicinity to increase the chance of the chemical reaction to occur, so highly porous gold nanoparticles possess the main attribute of a potent catalyst. Besides, since gold nanoparticles are a member of plasmonic metals, they can themselves act both as the light-absorbing material and the activation site for driving a light-induced chemical reaction. All of these attributes potentially make porous gold a powerful catalyst for plasmonic photocatalysis applications.

Plasmonic materials can interact with light through interband and intraband transitions and continuously supply reactive electrons and hole pairs to activate chemical species. While this novel family of catalysts shown promising results for several applications so far, their catalytic applications are still limited to drive simple chemical reactions. To further investigate the caliber of these materials in driving a chemical reaction, we fabricated highly porous sponge-shaped plasmonic Au nanoparticles (Au-Sponge). We utilized them to accelerate the complex light-induced CO_2 reduction reaction vis interband transition. Our results indicate that the Au-Sponge sample exhibits a 3.8-fold increase in methane production compared to the non-porous Au-Island sample. Furthermore, FDTD simulations of the Au-Sponge sample suggest that in addition to the benefits mentioned above, the porousness can increase the Au-Sponge sample's interaction with an incident electromagnetic wave which is a crucial step in a light-induced catalytic reaction.

6. Conclusion

There is a growing need for finding alternative sources of energy to meet the energy demands globally. Since solar energy is freely available worldwide, solar energy conversion is considered a promising solution for addressing the increasing energy demands. Solar energy can be utilized to produce hydrogen from water through water-splitting reaction. Also, it can be used to convert CO_2 into fuels such as methane or ethane through CO_2 photoreduction reaction. In this thesis, we utilized plasmonic nanoparticles with various shapes and structures for solar energy conversion applications. Ag and Au, the most common plasmonic materials, were chosen as the case studies for CO_2 photoreduction and water-splitting applications.

In the first step, we utilized bimetallic AgCu nanoparticles. We made heterojunctions between these nanoparticles and TiO_2 nanotube arrays (TNTA) using a photo deposition method. We reported the dominant formation of a C_2 product, namely, ethane, from the gas-phase photoreduction of CO_2 using TiO_2 nanotube arrays (TNTA) decorated with large-sized (80–200 nm) Ag and Cu nanoparticles without the use of a sacrificial agent or hole scavenger. Isotope-labeled mass spectrometry was used to verify the origin and identity of the reaction products. Under two-hour AM1.5G 1-sun illumination, the total rate of hydrocarbon production (methane + ethane) was highest for AgCu-TNTA with a total C_xH_{2x+2} rate of 23.88 μmol g–1 h–1. Under identical conditions, the C_xH_{2x+2} production rates for Ag-TNTA and Cu-TNTA were 6.54 and 1.39 μmol g–1 h–1, respectively. The formation of C_{2+} products such as ethane and ethanol rather than methane is more attractive due to their higher energy density and economic value, but the formation of C–C bonds is currently a major challenge in CO_2 photoreduction. For future works, a rational design of heterojunction between AgCu nanoparticles and TNTA, including careful investigation of the effect of the particle size and TNTA surface coverage by AgCu nanoparticles on the photocatalytic activity, can be investigated. In addition, improving the selectivity of CO_2 photoreduction reaction toward production of C_{2+} products should be investigated in the future steps.

Next, we fabricated ultrathin core-shell Au@a-TiO_2 nanoparticles for photoelectrochemical water-splitting reaction. To fabricate these samples, Au nanoparticles were fabricated on top of FTO substrate using a thermal annealing dewetting process. A thin layer of amorphous TiO_2 was deposited on top of them using the ALD deposition method. Under AM1.5 one sun illumination, photoanodes consisting of a single layer of ~50 nm diameter Au NPs coated with a shell of amorphous TiO_2 (Au@a-TiO_2) generate 2.5 mA cm^{-2} of photocurrent in 1 M KOH under 0.6 V external bias. Under the same conditions, the photoresponse of a-TiO_2 was only 0.3 mA Cm^{-2}. These results indicate that making a heterojunction between a plasmonic metal nanoparticle with a semiconductor is an efficient method for increasing the efficiency of a photoelectrode for photoelectrochemical water-splitting reaction. The next step in this project should focus on stacking multiple layers of Au@ a-TiO_2 on top of each other and investigating the ability of the gap-plasmon architecture to drive the photoelectrochemical water-splitting reaction. Also, the effect of the size of the Au nanoparticles on the photoresponse of the samples should be investigated and efforts should be focused on improving the visible-light response of the Au@a-TiO_2 photoelectrode.

In the last step, we fabricated sponge-shaped Au nanoparticles (Au-Sponge) using a combination of thermal dewetting and subsequent acid etching technique. Ag was chosen ad a sacrificial metal in the fabrication process of Au-Sponge. These samples were utilized CO_2 photoreduction reaction. Under the irradiation of a UV lamp, the rate of methane production was 582 µmol. g-1.hr^{-1} for the Au-Sponge samples, which was 3.8 times higher than the methane production rate using regular spherical-shaped Au nanoparticles (Au-Island) sample. These results indicate that due to their unique structure (porousness), the Au-Sponge sample can be utilized as standalone plasmonic catalysis for driving complex chemical reactions without the need to be hosted into the structure of a semiconductor material such as TiO_2 or a highly porous substrate. The next step in this project should be focused on investigating the effect of incorporation of a co-catalyst such as small-size Pt nanoparticles on the activity of Au-Sponge plasmonic catalysis for driving the CO_2 photoreduction.

In general, the future works in solar energy conversion should focus on increasing the efficiency of these processes. While the results of our works are promising, there is still a long way to commercializing these processes, specifically in the CO_2 photoreduction case where conversions are still below 1%. Increasing the efficiency of CO_2 photoreduction can be pursued in two different directions. The first direction should focus on fabrication of more efficient photocatalysts and the second direction should focus on the design and optimization of a reactor for CO_2 photoreduction reaction.

References

1. Qazi, A., et al., *Towards sustainable energy: a systematic review of renewable energy sources, technologies, and public opinions.* IEEE Access, 2019. **7**: p. 63837-63851.
2. Kruse, O., et al., *Photosynthesis: a blueprint for solar energy capture and biohydrogen production technologies.* Photochemical & Photobiological Sciences, 2005. **4**(12): p. 957-970.
3. Lincot, D., *The new paradigm of photovoltaics: From powering satellites to powering humanity.* Comptes Rendus Physique, 2017. **18**(7-8): p. 381-390.
4. Van de Krol, R. and M. Grätzel, *Photoelectrochemical hydrogen production*. Vol. 90. 2012: Springer.
5. Chang, X., T. Wang, and J. Gong, *CO 2 photo-reduction: insights into CO 2 activation and reaction on surfaces of photocatalysts.* Energy & Environmental Science, 2016. **9**(7): p. 2177-2196.
6. Bravo-Suárez, J.J., R.V. Chaudhari, and B. Subramaniam, *Design of heterogeneous catalysts for fuels and chemicals processing: An overview*, in *Novel Materials for Catalysis and Fuels Processing*. 2013, ACS Publications. p. 3-68.
7. Vaiano, V., D. Sannino, and P. Ciambelli, *Steam reduction of CO 2 on Pd/TiO 2 catalysts: a comparison between thermal and photocatalytic reactions.* Photochemical & Photobiological Sciences, 2015. **14**(3): p. 550-555.
8. Meng, X., et al., *Direct Methane Conversion under Mild Condition by Thermo-, Electro-, or Photocatalysis.* Chem, 2019.
9. Yang, X. and D. Wang, *Photocatalysis: from fundamental principles to materials and applications.* ACS Applied Energy Materials, 2018. **1**(12): p. 6657-6693.
10. van de Krol, R., Y. Liang, and J. Schoonman, *Solar hydrogen production with nanostructured metal oxides.* Journal of Materials Chemistry, 2008. **18**(20): p. 2311-2320.
11. Dutta, S.K., S.K. Mehetor, and N. Pradhan, *Metal semiconductor heterostructures for photocatalytic conversion of light energy.* The journal of physical chemistry letters, 2015. **6**(6): p. 936-944.
12. Su, J., et al., *2D/2D heterojunctions for catalysis.* Advanced Science, 2019. **6**(7): p. 1801702.
13. Farsinezhad, S., H. Sharma, and K. Shankar, *Interfacial band alignment for photocatalytic charge separation in TiO 2 nanotube arrays coated with CuPt nanoparticles.* Physical Chemistry Chemical Physics, 2015. **17**(44): p. 29723-29733.
14. Khan, M.R., et al., *Schottky barrier and surface plasmonic resonance phenomena towards the photocatalytic reaction: study of their mechanisms to enhance photocatalytic activity.* Catalysis Science & Technology, 2015. **5**(5): p. 2522-2531.
15. Hou, W. and S.B. Cronin, *A review of surface plasmon resonance-enhanced photocatalysis.* Advanced Functional Materials, 2013. **23**(13): p. 1612-1619.
16. Wu, N., *Plasmonic metal–semiconductor photocatalysts and photoelectrochemical cells: a review.* Nanoscale, 2018. **10**(6): p. 2679-2696.
17. Zhang, Y., et al., *Surface-plasmon-driven hot electron photochemistry.* Chemical reviews, 2017. **118**(6): p. 2927-2954.
18. Zhang, X., et al., *Plasmonic photocatalysis.* Reports on Progress in Physics, 2013. **76**(4): p. 046401.

19. Miller, D.C., et al. *Analysis of transmitted optical spectrum enabling accelerated testing of CPV designs*. in *High and Low Concentrator Systems for Solar Electric Applications IV*. 2009. International Society for Optics and Photonics.
20. Lee, D., T. Kim, and Q.-H. Park, *Performance analysis of parallelized PSTD-FDTD method for large-scale electromagnetic simulation.* Computer Physics Communications, 2021. **259**: p. 107631.
21. Siefke, T., et al., *Materials pushing the application limits of wire grid polarizers further into the deep ultraviolet spectral range.* Advanced Optical Materials, 2016. **4**(11): p. 1780-1786.
22. Inoue, T., et al., *Photoelectrocatalytic reduction of carbon dioxide in aqueous suspensions of semiconductor powders.* Nature, 1979. **277**(5698): p. 637-638.
23. Fu, J., et al., *Product selectivity of photocatalytic CO2 reduction reactions.* Materials Today, 2020. **32**: p. 222-243.
24. Yu, S., et al., *Plasmonic control of multi-electron transfer and C–C coupling in visible-light-driven CO2 reduction on Au nanoparticles.* Nano letters, 2018. **18**(4): p. 2189-2194.
25. Zhang, X., et al., *Photocatalytic conversion of diluted CO2 into light hydrocarbons using periodically modulated multiwalled nanotube arrays.* Angewandte Chemie International Edition, 2012. **51**(51): p. 12732-12735.
26. Sorcar, S., et al., *High-rate solar-light photoconversion of CO 2 to fuel: controllable transformation from C 1 to C 2 products.* Energy & Environmental Science, 2018. **11**(11): p. 3183-3193.
27. Kar, P., et al., *High rate CO2 photoreduction using flame annealed TiO2 nanotubes.* Applied Catalysis B: Environmental, 2019. **243**: p. 522-536.
28. Albero, J., Y. Peng, and H. Garcia, *Photocatalytic CO2 reduction to C2+ products.* ACS Catalysis, 2020. **10**(10): p. 5734-5749.
29. Li, J., et al., *Hydroxide Is Not a Promoter of C2+ Product Formation in the Electrochemical Reduction of CO on Copper.* Angewandte Chemie International Edition, 2020. **59**(11): p. 4464-4469.
30. Lum, Y., et al., *Optimizing C–C Coupling on Oxide-Derived Copper Catalysts for Electrochemical CO2 Reduction.* The Journal of Physical Chemistry C, 2017. **121**(26): p. 14191-14203.
31. Resasco, J., et al., *Promoter Effects of Alkali Metal Cations on the Electrochemical Reduction of Carbon Dioxide.* Journal of the American Chemical Society, 2017. **139**(32): p. 11277-11287.
32. Du, C., et al., *CO2 transformation to multicarbon products by photocatalysis and electrocatalysis.* Materials Today Advances, 2020. **6**: p. article no 100071.
33. Habisreutinger, S.N., L. Schmidt-Mende, and J.K. Stolarczyk, *Photocatalytic Reduction of CO2 on TiO2 and Other Semiconductors.* Angewandte Chemie International Edition, 2013. **52**(29): p. 7372-7408.
34. Henderson, M.A., A. Szabó, and J.T. Yates, *Direct observation of adsorbate-adsorbate repulsions along a one-dimensional array: CO on the steps of Pt(112).* Chemical Physics Letters, 1990. **168**(1): p. 51-55.
35. Borguet, E. and H.-L. Dai, *Probing Surface Short Range Order and Inter-Adsorbate Interactions through IR Vibrational Spectroscopy: CO on Cu(100).* The Journal of Physical Chemistry B, 2005. **109**(17): p. 8509-8512.
36. Wei, D.H., D.C. Skelton, and S.D. Kevan, *Trends in lateral interactions between CO chemisorbed on low index copper surfaces.* Surface Science, 1995. **326**(1): p. 167-176.

37. Bartels, L., G. Meyer, and K.H. Rieder, *The evolution of CO adsorption on Cu(111) as studied with bare and CO-functionalized scanning tunneling tips.* Surface Science, 1999. **432**(3): p. L621-L626.
38. Manuel, A.P., et al., *Plexcitonics – fundamental principles and optoelectronic applications.* Journal of Materials Chemistry C, 2019. **7**(7): p. 1821-1853.
39. Wang, W.-N., et al., *Size and Structure Matter: Enhanced CO2 Photoreduction Efficiency by Size-Resolved Ultrafine Pt Nanoparticles on TiO2 Single Crystals.* Journal of the American Chemical Society, 2012. **134**(27): p. 11276-11281.
40. Varghese, O.K., et al., *High-Rate Solar Photocatalytic Conversion of CO2 and Water Vapor to Hydrocarbon Fuels.* Nano Letters, 2009. **9**(2): p. 731-737.
41. Wang, C., et al., *Visible Light Photoreduction of CO2 Using CdSe/Pt/TiO2 Heterostructured Catalysts.* The Journal of Physical Chemistry Letters, 2010. **1**(1): p. 48-53.
42. Kar, P., et al., *Enhanced CH4 yield by photocatalytic CO2 reduction using TiO2 nanotube arrays grafted with Au, Ru, and ZnPd nanoparticles.* Nano Research, 2016. **9**(11): p. 3478-3493.
43. Low, J., et al., *Direct evidence and enhancement of surface plasmon resonance effect on Ag-loaded TiO2 nanotube arrays for photocatalytic CO2 reduction.* Applied Surface Science, 2018. **434**: p. 423-432.
44. Jiao, J., et al., *AuPd/3DOM-TiO2 catalysts for photocatalytic reduction of CO2: High efficient separation of photogenerated charge carriers.* Applied Catalysis B: Environmental, 2017. **209**: p. 228-239.
45. Neaţu, Ş., et al., *Gold–Copper Nanoalloys Supported on TiO2 as Photocatalysts for CO2 Reduction by Water.* Journal of the American Chemical Society, 2014. **136**(45): p. 15969-15976.
46. Lin, L.-Y., et al., *Engineering stable Pt nanoparticles and oxygen vacancies on defective TiO2 via introducing strong electronic metal-support interaction for efficient CO2 photoreduction.* Chemical Engineering Journal, 2020. **389**: p. article no 123450.
47. Tanaka, Y., A. Sanada, and K. Sasaki, *Nanoscale interference patterns of gap-mode multipolar plasmonic fields.* Scientific Reports, 2012. **2**(1): p. article no 764.
48. Manuel, A.P., et al., *Plasmonic photocatalysis and SERS sensing using ellipsometrically modeled Ag nanoisland substrates.* Nanotechnology, 2020. **31**(36): p. article no 365301.
49. Park, S.Y. and D. Stroud, *Surface-plasmon dispersion relations in chains of metallic nanoparticles: An exact quasistatic calculation.* Physical Review B, 2004. **69**(12): p. article no 125418.
50. Chen, F., N. Alemu, and R.L. Johnston, *Collective plasmon modes in a compositionally asymmetric nanoparticle dimer.* AIP Advances, 2011. **1**(3): p. article no 032134.
51. Jiang, M.-M., et al., *Hybrid quadrupolar resonances stimulated at short wavelengths using coupled plasmonic silver nanoparticle aggregation.* Journal of Materials Chemistry C, 2014. **2**(1): p. 56-63.
52. Zhu, Z., et al., *Preparation of Pd–Au/TiO2–WO3 to enhance photoreduction of CO2 to CH4 and CO.* Journal of CO2 Utilization, 2018. **28**: p. 247-254.
53. Varghese, O.K., et al., *Crystallization and high-temperature structural stability of titanium oxide nanotube arrays.* Journal of Materials Research, 2003. **18**(1): p. 156-165.
54. Shankar, K., et al., *Highly-ordered TiO2 nanotube arrays up to 220 µm in length: use in water photoelectrolysis and dye-sensitized solar cells.* Nanotechnology, 2007. **18**(6): p. article no 065707.

55. Macak, J.M., et al., *TiO2 nanotubes: Self-organized electrochemical formation, properties and applications.* Current Opinion in Solid State and Materials Science, 2007. **11**(1-2): p. 3-18.
56. Scirè, S., et al., *Supported silver catalysts prepared by deposition in aqueous solution of Ag nanoparticles obtained through a photochemical approach.* Applied Catalysis A: General, 2009. **367**(1): p. 138-145.
57. Singh, M.K., et al., *Localized surface plasmon behavior of Ag-Cu alloy nanoparticles stabilized by rice-starch and gelatin.* AIP Advances, 2015. **5**(10): p. article no 107108.
58. Bronneberg, A.C., C. Höhn, and R. van de Krol, *Probing the interfacial chemistry of ultrathin ALD-grown TiO2 films: An in-line XPS study.* The Journal of Physical Chemistry C, 2017. **121**(10): p. 5531-5538.
59. Yan, J., et al., *Fabrication of TiO2/C3N4 heterostructure for enhanced photocatalytic Z-scheme overall water splitting.* Applied Catalysis B: Environmental, 2016. **191**: p. 130-137.
60. Yang, T., et al., *Enhanced photocatalytic ozonation degradation of organic pollutants by ZnO modified TiO2 nanocomposites.* Applied Catalysis B: Environmental, 2018. **221**: p. 223-234.
61. Tahir, M. and N.S. Amin, *Indium-doped TiO2 nanoparticles for photocatalytic CO2 reduction with H2O vapors to CH4.* Applied Catalysis B: Environmental, 2015. **162**: p. 98-109.
62. Hu, J., et al., *Construction of solid-state Z-scheme carbon-modified TiO2/WO3 nanofibers with enhanced photocatalytic hydrogen production.* Journal of Power Sources, 2016. **328**: p. 28-36.
63. Hao, R., et al., *Template-free preparation of macro/mesoporous g-C3N4/TiO2 heterojunction photocatalysts with enhanced visible light photocatalytic activity.* Applied Catalysis B: Environmental, 2016. **187**: p. 47-58.
64. Balajka, J., et al., *High-affinity adsorption leads to molecularly ordered interfaces on TiO2 in air and solution.* Science, 2018. **361**(6404): p. 786-789.
65. Qi, L., et al., *High-surface area mesoporous Pt/TiO2 hollow chains for efficient formaldehyde decomposition at ambient temperature.* Journal of hazardous materials, 2016. **301**: p. 522-530.
66. Chen, B., et al., *Carbon-coated Cu-Co bimetallic nanoparticles as selective and recyclable catalysts for production of biofuel 2, 5-dimethylfuran.* Applied Catalysis B: Environmental, 2017. **200**: p. 192-199.
67. Zhang, P., et al., *In-situ synthesis of Cu nanoparticles hybridized with carbon quantum dots as a broad spectrum photocatalyst for improvement of photocatalytic H2 evolution.* Applied Catalysis B: Environmental, 2017. **206**: p. 328-335.
68. Ge, M.-Z., et al., *In situ plasmonic Ag nanoparticle anchored TiO 2 nanotube arrays as visible-light-driven photocatalysts for enhanced water splitting.* Nanoscale, 2016. **8**(9): p. 5226-5234.
69. Benipal, N., et al., *Carbon nanotube supported PdAg nanoparticles for electrocatalytic oxidation of glycerol in anion exchange membrane fuel cells.* Applied Catalysis B: Environmental, 2017. **210**: p. 121-130.
70. Kar, P., et al., *High rate CO2 photoreduction using flame annealed TiO2 nanotubes.* Applied Catalysis B: Environmental, 2019. **243**: p. 522-536.

71. Kar, P., et al., *Heterojunctions of mixed phase TiO2 nanotubes with Cu, CuPt, and Pt nanoparticles: interfacial band alignment and visible light photoelectrochemical activity.* Nanotechnology, 2017. **29**(1): p. article no 014002.
72. Mogensen, K.B. and K. Kneipp, *Size-dependent shifts of plasmon resonance in silver nanoparticle films using controlled dissolution: monitoring the onset of surface screening effects.* The Journal of Physical Chemistry C, 2014. **118**(48): p. 28075-28083.
73. Mohammadpour, A. and K. Shankar, *Anodic TiO 2 nanotube arrays with optical wavelength-sized apertures.* Journal of Materials Chemistry, 2010. **20**(39): p. 8474-8477.
74. Katyal, J., *Plasmonic coupling in Au, Ag and Al nanosphere homo-dimers for sensing and SERS.* Advanced Electromagnetics, 2018. **7**(2): p. 83-90.
75. Chen, F., N. Alemu, and R.L. Johnston, *Collective plasmon modes in a compositionally asymmetric nanoparticle dimer.* AIP Advances, 2011. **1**(3): p. 032134.
76. Zayats, A.V., I.I. Smolyaninov, and A.A. Maradudin, *Nano-optics of surface plasmon polaritons.* Physics Reports, 2005. **408**(3): p. 131-314.
77. Ishii, S., S.L. Shinde, and T. Nagao, *Nonmetallic Materials for Plasmonic Hot Carrier Excitation.* Advanced Optical Materials, 2019. **7**(1): p. 1800603.
78. Zorić, I., et al., *Gold, Platinum, and Aluminum Nanodisk Plasmons: Material Independence, Subradiance, and Damping Mechanisms.* ACS Nano, 2011. **5**(4): p. 2535-2546.
79. Hubenthal, F., *Increased Damping of Plasmon Resonances in Gold Nanoparticles Due to Broadening of the Band Structure.* Plasmonics, 2013. **8**(3): p. 1341-1349.
80. Manuel, A.P., et al., *Plexcitonics - fundamental principles and optoelectronic applications.* Journal of Materials Chemistry C, 2019. **7**(7): p. 1821-1853.
81. Bernardi, M., et al., *Theory and computation of hot carriers generated by surface plasmon polaritons in noble metals.* Nature Communications, 2015. **6**(1): p. 7044.
82. Axelevitch, A., B. Apter, and G. Golan, *Simulation and experimental investigation of optical transparency in gold island films.* Optics express, 2013. **21**(4): p. 4126-4138.
83. Oulton, R.F., et al., *Plasmon lasers at deep subwavelength scale.* Nature, 2009. **461**(7264): p. 629-632.
84. Akbari-Moghanjoughi, M., *Plasmon Oscillations and de Broglie's Matter Waves Instabilities.* arXiv preprint arXiv:2002.04690, 2020.
85. Yu, B., et al., *Photocatalytic reduction of CO2 over Ag/TiO2 nanocomposites prepared with a simple and rapid silver mirror method.* Nanoscale, 2016. **8**(23): p. 11870-11874.
86. Kong, D., et al., *Electrodeposited Ag nanoparticles on TiO2 nanorods for enhanced UV visible light photoreduction CO2 to CH4.* Applied Surface Science, 2013. **277**: p. 105-110.
87. Hong, D., et al., *Plasmonic Ag@ TiO2 Core–Shell Nanoparticles for Enhanced CO2 Photoconversion to CH4.* ACS Sustainable Chemistry & Engineering, 2019. **7**(23): p. 18955-18964.
88. Zhai, Q., et al., *Photocatalytic conversion of carbon dioxide with water into methane: platinum and copper (I) oxide co-catalysts with a core–shell structure.* Angewandte Chemie, 2013. **125**(22): p. 5888-5891.
89. Wang, Z., et al., *Enhanced Photocatalytic CO2 Reduction over TiO2 Using Metalloporphyrin as the Cocatalyst.* Catalysts, 2020. **10**(6): p. article no 654.
90. Mekasuwandumrong, O., et al., *Synthesis of Cu/TiO2 catalysts by reactive magnetron sputtering deposition and its application for photocatalytic reduction of CO2 and H2O to CH4.* Ceramics International, 2019. **45**(17): p. 22961-22971.

91. Fresno, F., et al., *Mechanistic View of the Main Current Issues in Photocatalytic CO2 Reduction.* The Journal of Physical Chemistry Letters, 2018. **9**(24): p. 7192-7204.
92. Park, S.-M., et al., *Hybrid CuxO–TiO2 Heterostructured Composites for Photocatalytic CO2 Reduction into Methane Using Solar Irradiation: Sunlight into Fuel.* ACS Omega, 2016. **1**(5): p. 868-875.
93. Hou, W., et al., *Photocatalytic conversion of CO2 to hydrocarbon fuels via plasmon-enhanced absorption and metallic interband transitions.* Acs Catalysis, 2011. **1**(8): p. 929-936.
94. Vu, N.-N., S. Kaliaguine, and T.-O. Do, *Critical Aspects and Recent Advances in Structural Engineering of Photocatalysts for Sunlight-Driven Photocatalytic Reduction of CO2 into Fuels.* Advanced Functional Materials, 2019. **29**(31): p. article no 1901825.
95. Handoko, A.D., K.W. Chan, and B.S. Yeo, *–CH3 Mediated Pathway for the Electroreduction of CO2 to Ethane and Ethanol on Thick Oxide-Derived Copper Catalysts at Low Overpotentials.* ACS Energy Letters, 2017. **2**(9): p. 2103-2109.
96. Sorcar, S., et al., *CO 2, water, and sunlight to hydrocarbon fuels: a sustained sunlight to fuel (Joule-to-Joule) photoconversion efficiency of 1%.* Energy & Environmental Science, 2019. **12**(9): p. 2685-2696.
97. Chen, W., et al., *Silver addition to a cobalt Fischer–Tropsch catalyst.* Journal of Catalysis, 2018. **366**: p. 107-114.
98. Mohammadpour, A., et al., *Electron transport, trapping and recombination in anodic TiO2 nanotube arrays.* Current Nanoscience, 2015. **11**(5): p. 593-614.
99. Feizpoor, S. and A. Habibi-Yangjeh, *Integration of Ag2WO4 and AgBr with TiO2 to fabricate ternary nanocomposites: Novel plasmonic photocatalysts with remarkable activity under visible light.* Materials Research Bulletin, 2018. **99**: p. 93-102.
100. Amidani, L., et al., *Probing Long-Lived Plasmonic-Generated Charges in TiO2/Au by High-Resolution X-ray Absorption Spectroscopy.* Angewandte Chemie International Edition, 2015. **54**(18): p. 5413-5416.
101. Zeng, S., et al., *Optical control of selectivity of high rate CO2 photoreduction via interband- or hot electron Z-scheme reaction pathways in Au-TiO2 plasmonic photonic crystal photocatalyst.* Applied Catalysis B: Environmental, 2020. **267**: p. article no 118644.
102. Ziegler, T., V. Tschinke, and A. Becke, *Theoretical study on the relative strengths of the metal-hydrogen and metal-methyl bonds in complexes of middle to late transition metals.* Journal of the American Chemical Society, 1987. **109**(5): p. 1351-1358.
103. Ferraudi, G., *Photochemical generation of metastable methylcopper complexes. Oxidation-reduction of methyl radicals by copper complexes.* Inorganic Chemistry, 1978. **17**(9): p. 2506-2508.
104. Tayebi, M. and B.-K. Lee, *Recent advances in BiVO4 semiconductor materials for hydrogen production using photoelectrochemical water splitting.* Renewable and Sustainable Energy Reviews, 2019. **111**: p. 332-343.
105. Park, K., et al., *A methodological review on material growth and synthesis of solar-driven water splitting photoelectrochemical cells.* RSC Advances, 2019. **9**(52): p. 30112-30124.
106. Kumar, P., et al., *Noble Metal Free, Visible Light Driven Photocatalysis Using TiO2 Nanotube Arrays Sensitized by P-Doped C3N4 Quantum Dots.* Advanced Optical Materials, 2019.
107. Atta, S., et al., *TiO2 on gold nanostars enhances photocatalytic water reduction in the near-infrared regime.* Chem, 2018. **4**(9): p. 2140-2153.

108. Eustis, S. and M.A. El-Sayed, *Why gold nanoparticles are more precious than pretty gold: noble metal surface plasmon resonance and its enhancement of the radiative and nonradiative properties of nanocrystals of different shapes.* Chemical society reviews, 2006. **35**(3): p. 209-217.
109. Sönnichsen, C., et al., *Drastic reduction of plasmon damping in gold nanorods.* Physical review letters, 2002. **88**(7): p. 077402.
110. Tan, F., et al., *Rough gold films as broadband absorbers for plasmonic enhancement of TiO 2 photocurrent over 400–800 nm.* Scientific reports, 2016. **6**: p. 33049.
111. Sreedhar, A., et al., *Charge carrier generation and control on plasmonic Au clusters functionalized TiO2 thin films for enhanced visible light water splitting activity.* Ceramics International, 2018. **44**(15): p. 18978-18986.
112. Hoang, C.V., et al., *Interplay of hot electrons from localized and propagating plasmons.* Nature communications, 2017. **8**(1): p. 771.
113. Chen, H., G. Liu, and L. Wang, *Switched photocurrent direction in Au/TiO 2 bilayer thin films.* Scientific reports, 2015. **5**: p. 10852.
114. Seh, Z.W., et al., *Janus Au-TiO2 photocatalysts with strong localization of plasmonic near-fields for efficient visible-light hydrogen generation.* Advanced Materials, 2012. **24**(17): p. 2310-2314.
115. Hu, S., et al., *Amorphous TiO2 coatings stabilize Si, GaAs, and GaP photoanodes for efficient water oxidation.* Science, 2014. **344**(6187): p. 1005-1009.
116. Guo, Z., F. Ambrosio, and A. Pasquarello, *Hole diffusion across leaky amorphous TiO 2 coating layers for catalytic water splitting at photoanodes.* Journal of Materials Chemistry A, 2018. **6**(25): p. 11804-11810.
117. Nunez, P., et al., *Characterization of Electronic Transport through Amorphous TiO2 Produced by Atomic Layer Deposition.* The Journal of Physical Chemistry C, 2019. **123**(33): p. 20116-20129.
118. Pham, H.H. and L.-W. Wang, *Oxygen vacancy and hole conduction in amorphous TiO 2.* Physical Chemistry Chemical Physics, 2015. **17**(1): p. 541-550.
119. Pham, H.H. and L.-W. Wang, *Electronic structures and current conductivities of B, C, N and F defects in amorphous titanium dioxide.* Physical Chemistry Chemical Physics, 2015. **17**(17): p. 11908-11913.
120. Kontoleta, E., S.H. Askes, and E.C. Garnett, *Self-optimized catalysts: Hot-electron driven photosynthesis of catalytic photocathodes.* ACS applied materials & interfaces, 2019. **11**(39): p. 35713-35719.
121. Moehl, T., et al., *Investigation of (Leaky) ALD TiO2 Protection Layers for Water-Splitting Photoelectrodes.* ACS applied materials & interfaces, 2017. **9**(50): p. 43614-43622.
122. Moon, S.Y., et al., *Plasmonic hot carrier-driven oxygen evolution reaction on Au nanoparticles/TiO 2 nanotube arrays.* Nanoscale, 2018. **10**(47): p. 22180-22188.
123. Smith, K.A., et al., *Effects of proton irradiation on structural and electrochemical charge storage properties of TiO 2 nanotube electrodes for lithium-ion batteries.* Journal of Materials Chemistry A, 2017. **5**(23): p. 11815-11824.
124. Niilisk, A., et al., *Structural study of TiO2 thin films by micro-Raman spectroscopy.* Open Physics, 2006. **4**(1): p. 105-116.
125. Ghobadi, A., et al., *A heterojunction design of single layer hole tunneling ZnO passivation wrapping around TiO 2 nanowires for superior photocatalytic performance.* Scientific reports, 2016. **6**: p. 30587.

126. Ulusoy, T.G., A. Ghobadi, and A.K. Okyay, *Surface engineered angstrom thick ZnO-sheathed TiO 2 nanowires as photoanodes for performance enhanced dye-sensitized solar cells.* Journal of Materials Chemistry A, 2014. **2**(40): p. 16867-16876.
127. Zhu, L., et al., *Effects of synthesis methods on catalytic activities of CoOx–TiO2 for low-temperature NH3-SCR of NO.* Journal of Environmental Sciences, 2017. **54**: p. 277-287.
128. Olowoyo, J.O., et al., *Self-organized copper impregnation and doping in TiO2 with enhanced photocatalytic conversion of H2O and CO2 to fuel.* International Journal of Hydrogen Energy, 2018. **43**(42): p. 19468-19480.
129. Kim, M.-S., et al., *Catalytic reduction of nitrate in water over Pd–Cu/TiO2 catalyst: effect of the strong metal-support interaction (SMSI) on the catalytic activity.* Applied Catalysis B: Environmental, 2013. **142**: p. 354-361.
130. Wu, L., et al., *Plasmon-induced photoelectrocatalytic activity of Au nanoparticles enhanced TiO2 nanotube arrays electrodes for environmental remediation.* Applied catalysis B: environmental, 2015. **164**: p. 217-224.
131. Guzman, F., S.S. Chuang, and C. Yang, *Role of methanol sacrificing reagent in the photocatalytic evolution of hydrogen.* Industrial & Engineering Chemistry Research, 2012. **52**(1): p. 61-65.
132. Nishi, H. and T. Tatsuma, *Mechanistic analysis of plasmon-induced charge separation by the use of chemically synthesized gold nanorods.* The Journal of Physical Chemistry C, 2018. **122**(4): p. 2330-2335.
133. Thrall, E.S., et al., *The role of photon energy and semiconductor substrate in the plasmon-mediated photooxidation of citrate by silver nanoparticles.* The Journal of Physical Chemistry C, 2013. **117**(49): p. 26238-26247.
134. Jian, A., et al., *Quantitative investigation of plasmonic hot-electron injection by KPFM.* Applied Surface Science, 2019. **492**: p. 644-650.
135. Zeng, S., et al., *Optical Control of Selectivity of High Rate CO2 Photoreduction Via Interband-or Hot Electron Z-Scheme Reaction Pathways in Au-TiO2 Plasmonic Photonic Crystal Photocatalyst.* Applied Catalysis B: Environmental, 2020: p. 118644.
136. Khomenko, V., et al., *Electronic absorption by Ti 3+ ions and electron delocalization in synthetic blue rutile.* Physics and Chemistry of Minerals, 1998. **25**(5): p. 338-346.
137. Wu, X., et al., *Broadband plasmon photocurrent generation from Au nanoparticles/mesoporous TiO2 nanotube electrodes.* Solar Energy Materials and Solar Cells, 2015. **138**: p. 80-85.
138. Warren, S.C. and E. Thimsen, *Plasmonic solar water splitting.* Energy & Environmental Science, 2012. **5**(1): p. 5133-5146.
139. Cushing, S.K., et al., *Controlling plasmon-induced resonance energy transfer and hot electron injection processes in Metal@ TiO2 core–shell nanoparticles.* The Journal of Physical Chemistry C, 2015. **119**(28): p. 16239-16244.
140. Moon, C.W., et al., *Plasmonic octahedral gold nanoparticles of maximized near electromagnetic fields for enhancing catalytic hole transfer in solar water splitting.* Particle & Particle Systems Characterization, 2017. **34**(1): p. 1600340.
141. Robatjazi, H., et al., *Direct plasmon-driven photoelectrocatalysis.* Nano letters, 2015. **15**(9): p. 6155-6161.
142. Brennan, L.J., et al., *Hot plasmonic electrons for generation of enhanced photocurrent in gold-TiO 2 nanocomposites.* Nanoscale research letters, 2015. **10**(1): p. 1-12.

143. DuChene, J.S., et al., *Hot hole collection and photoelectrochemical CO2 reduction with plasmonic Au/p-GaN photocathodes.* Nano letters, 2018. **18**(4): p. 2545-2550.
144. Sankar, M., et al., *Role of the Support in Gold-Containing Nanoparticles as Heterogeneous Catalysts.* Chemical Reviews, 2020. **120**(8): p. 3890-3938.
145. Pan, Y., et al., *Active sites in heterogeneous catalytic reaction on metal and metal oxide: theory and practice.* Catalysts, 2018. **8**(10): p. 478.
146. Zielasek, V., et al., *Gold catalysts: nanoporous gold foams.* Angewandte Chemie International Edition, 2006. **45**(48): p. 8241-8244.
147. Rao, W., et al., *Nanoporous gold nanoparticles and Au/Al2O3 hybrid nanoparticles with large tunability of plasmonic properties.* ACS Applied Materials & Interfaces, 2017. **9**(7): p. 6273-6281.
148. Liebig, F., et al., *Spiked gold nanotriangles: formation, characterization and applications in surface-enhanced Raman spectroscopy and plasmon-enhanced catalysis.* RSC Advances, 2020. **10**(14): p. 8152-8160.
149. Pellarin, M., et al., *Fano transparency in rounded nanocube dimers induced by gap plasmon coupling.* ACS nano, 2016. **10**(12): p. 11266-11279.
150. Wittstock, A., et al., *Nanoporous gold catalysts for selective gas-phase oxidative coupling of methanol at low temperature.* Science, 2010. **327**(5963): p. 319-322.
151. Zeng, S., et al., *Optical control of selectivity of high rate CO2 photoreduction via interband- or hot electron Z-scheme reaction pathways in Au-TiO2 plasmonic photonic crystal photocatalyst.* Applied Catalysis B: Environmental, 2020. **267**: p. 118644.
152. Zhao, J., et al., *A comparison of photocatalytic activities of gold nanoparticles following plasmonic and interband excitation and a strategy for harnessing interband hot carriers for solution phase photocatalysis.* ACS central science, 2017. **3**(5): p. 482-488.
153. Tian, B., et al., *UV-driven overall water splitting using unsupported gold nanoparticles as photocatalysts.* Chemical Communications, 2018. **54**(15): p. 1845-1848.
154. Jiao, X., et al., *Broad-Spectral-Response Photocatalysts for CO2 Reduction.* ACS Central Science, 2020. **6**(5): p. 653-660.
155. Xu, H., et al., *General synthesis of sponge-like ultrafine nanoporous metals by dealloying in citric acid.* Nano Research, 2016. **9**(8): p. 2467-2477.
156. Liao, T.-Y., et al., *Large-area Raman enhancement substrates using spontaneous dewetting of gold films and silver nanoparticles deposition.* Sensors and Actuators B: Chemical, 2011. **156**(1): p. 245-250.
157. Godipurge, S., et al., *A facile and green strategy for the synthesis of Au, Ag and Au–Ag alloy nanoparticles using aerial parts of R. hypocrateriformis extract and their biological evaluation.* Enzyme and microbial technology, 2016. **95**: p. 174-184.
158. Roger, I., et al., *The direct hydrothermal deposition of cobalt-doped MoS 2 onto fluorine-doped SnO 2 substrates for catalysis of the electrochemical hydrogen evolution reaction.* Journal of Materials Chemistry A, 2017. **5**(4): p. 1472-1480.
159. Iyengar, P., C. Das, and K. Balasubramaniam, *Photoelectrochemical performance of NiO-coated ZnO–CdS core-shell photoanode.* Journal of Physics D: Applied Physics, 2017. **50**(10): p. 10LT01.
160. Rouya, E., et al., *Electrochemical characterization of the surface area of nanoporous gold films.* Journal of The Electrochemical Society, 2012. **159**(4): p. K97.
161. Tan, Y.H., et al., *Surface area and pore size characteristics of nanoporous gold subjected to thermal, mechanical, or surface modification studied using gas adsorption isotherms, cyclic*

voltammetry, thermogravimetric analysis, and scanning electron microscopy. Journal of materials chemistry, 2012. **22**(14): p. 6733-6745.

162. Sukeri, A., L.P.H. Saravia, and M. Bertotti, *A facile electrochemical approach to fabricate a nanoporous gold film electrode and its electrocatalytic activity towards dissolved oxygen reduction.* Physical Chemistry Chemical Physics, 2015. **17**(43): p. 28510-28514.
163. Wittstock, A., J. Biener, and M. Bäumer, *Nanoporous gold: a new material for catalytic and sensor applications.* Physical Chemistry Chemical Physics, 2010. **12**(40): p. 12919-12930.
164. Farias, M.J., et al., *Disentangling catalytic activity at terrace and step sites on selectively Ru-modified well-ordered Pt surfaces probed by CO electro-oxidation.* ACS Catalysis, 2016. **6**(5): p. 2997-3007.
165. Farias, M.J. and J.M. Feliu, *Determination of specific electrocatalytic sites in the oxidation of small molecules on crystalline metal surfaces.* Electrocatalysis, 2020: p. 79-103.
166. Ding, Y. and M. Chen, *Nanoporous metals for catalytic and optical applications.* MRS bulletin, 2009. **34**(8): p. 569-576.
167. Falsig, H., et al., *Trends in the catalytic CO oxidation activity of nanoparticles.* Angewandte Chemie, 2008. **120**(26): p. 4913-4917.
168. Qian, L., et al., *Surface enhanced Raman scattering of nanoporous gold: Smaller pore sizes stronger enhancements.* Applied physics letters, 2007. **90**(15): p. 153120.
169. Liu, K., et al., *Porous Au–Ag nanospheres with high-density and highly accessible hotspots for SERS analysis.* Nano letters, 2016. **16**(6): p. 3675-3681.
170. Li, X., D. Xiao, and Z. Zhang, *Landau damping of quantum plasmons in metal nanostructures.* New Journal of Physics, 2013. **15**(2): p. 023011.
171. Sundararaman, R., et al., *Theoretical predictions for hot-carrier generation from surface plasmon decay.* Nature Communications, 2014. **5**(1): p. 5788.
172. Vahidzadeh, E., et al., *Asymmetric Multipole Plasmon-Mediated Catalysis Shifts the Product Selectivity of CO2 Photoreduction toward C2+ Products.* ACS Applied Materials & Interfaces, 2021. **13**(6): p. 7248-7258.
173. Tatsuma, T. and H. Nishi, *Plasmonic hole ejection involved in plasmon-induced charge separation.* Nanoscale horizons, 2020. **5**(4): p. 597-606.